2022-12-01

Engineering 3D Bioprinted Cardiac Spheroidal Droplets With Cardiomyocytes and Cardiac Fibroblasts for Tissue Engineering and Drug Cytotoxicity Studies

Raven El Khoury
University of Texas at El Paso

ENGINEERING 3D BIOPRINTED CARDIAC SPHEROIDAL DROPLETS WITH

CARDIOMYOCYTES AND CARDIAC FIBROBLASTS FOR TISSUE

ENGINEERING AND DRUG CYTOTOXICITY STUDIES

RAVEN EL KHOURY

Doctoral Program in Biomedical Engineering

APPROVED:

_____
Binata Joddar, Ph.D., Chair

_____
Sylvia L. Natividad-Diaz, Ph.D.

_____
Md Nurunnabi, Ph.D

_____
Wilson Poon, Ph.D

_____
Stephen L. Crites, Ph.D.
Dean of the Graduate School

Dedication

This thesis is dedicated to the ones I love and to me.

R.E.K

ENGINEERING 3D BIOPRINTED CARDIAC SPHEROIDAL DROPLETS WITH

CARDIOMYOCYTES AND CARDIAC FIBROBLASTS FOR TISSUE

ENGINEERING AND DRUG CYTOTOXICITY STUDIES

by

RAVEN EL KHOURY

DISSERTATION

Presented to the Faculty of the Graduate School of

The University of Texas at El Paso

in Partial Fulfillment

of the Requirements

for the Degree of

DOCTOR OF PHILOSOPHY

Department of Metallurgical, Materials and

Biomedical Engineering

THE UNIVERSITY OF TEXAS AT EL PASO

DECEMBER 2022

Acknowledgments

Achieving the goals I set before me was not a simple mission. It would not have been possible without all the support I have received from the people around me. I want to acknowledge the guidance and support I have received from my advisor Dr. Binata Joddar who made this work possible. I would further like to acknowledge the faculty members in the Biomedical Engineering and the Border Biomedical Research Center (BBRC) at the University of Texas at El Paso for their unswerving assistance. I want to express gratitude to my committee members for their constructive feedback and insightful comments I have received throughout this journey. I would like to acknowledge the assistance received from the staff and faculty members in the Department of Metallurgical, Materials, and Biomedical Engineering and Texas Tech University Health Sciences Center El Paso (TTUHSC). I also would like to thank fellow members of my research group from the Inspired Materials and Stem Cell based Tissue Engineering Laboratory (IMSTEL) at UTEP. I am also grateful to the funding sources from the National Institute of Science (NSF), the National Institute of Health (NIH), and UTEP Graduate School, who supported my doctoral studies and scientific research.

Abstract

Engineering is the supreme human endeavor that involves harnessing the scientific understanding of the natural world to design and invent objects to improve the society around us. Biomedical engineering is the implementation of concepts acquired from engineering in biology and medicine that aims to improve human health through the integration of engineering with biomedical sciences. The mission of a biomedical engineer is to develop technologies that help advance the quality of people's health using various tools and materials with one passion and goal: making the patient's life longer and easier. Tissue engineering is developed from the field of biomaterials and refers to the application of incorporating scaffolds, cells, and biologically active molecules into functional tissues. Engineered tissue replicates must provide in-vivo-like physiological demands and have the ability to enable suitable dynamic and mechanical environments for the hosted cells.

Heart disease is the leading cause of death worldwide and in the United States. The most common type is coronary artery disease, which can cause heart-related diseases leading to heart failure. When a plaque first grows within the walls of the coronary arteries, the blood flow to the heart becomes limited. If not treated over time, the heart muscle or myocardium will start to die, causing a heart attack. Tissue engineering aims to fabricate functional constructs that have the potential to regenerate damaged tissues. Two-dimensional cultured-based systems lack cell-cell and cell-matrix interactions, and failure to mimic the in vivo microenvironment of the native heart ultimately increases the need for an in vitro fabrication of three-dimensional (3D) cardiac tissue models for more effective drug toxicity testing and pharmaceutical assays. To surpass the current limitations in tissue engineering approaches, in this study three-dimensional bioprinting

technology has been used to design a unique 3D cardiac spheroidal droplet hydrogel scaffold using medium viscosity alginate and gelatin using a CELLINK-BIO X printer. This technique was further scaled up to a high throughput 96-well array set-up with a six-axis robotic arm using a 3D bioprinter (BioAssemblyBot). This study produced morphologically consistent 3D spheroidal droplets with significant porosity and a degree of interconnectivity between the pores. The resultant scaffolds retained structural fidelity after 28 days confirming their use in long-term *in-vitro* cell culture studies, and rheological studies performed on these 3D spheroidal droplets were found to be suitable for in-vitro cardiac tissue engineering studies. Cell viability quantification showed a steady turnover of cells in the scaffolds for up to 14 days, and the percent heterocellular coupling (HC) between CMs and cardiac fibroblasts (CFs) was quantified.

Based on such an existing premise, we adopted the optimized 3D bioprinted cardiac spheroidal model for testing the effects of cardiotoxicity induced by DOX. This study yielded a mass production of 3D spheroidal droplet scaffolds tailored to study the induced cytotoxic effects of DOX in-vitro. We further anticipate using this 3D bioprinted model to facilitate early-phase drug development in preclinical studies with sufficient versatility to evaluate the responses of various drugs and small molecules more efficiently at a relatively low cost. As a more sophisticated and cardiac-relevant in-vitro model, we expect to see increased adoption of this model for a better understanding of human biology as well as disease diagnosis and therapeutics.

Table of Contents

List of Tables

List of Figures

List of Illustrations

Chapter 1: Introduction and Specific Aims

1.1.   Heart Disease: Worldwide Epidemic

Cardiovascular diseases (CVDs) are the primary cause of death globally [4], with coronary artery disease (CAD) being the leading cause attributable to CVD in the US [5]. While examples of heart disease include arrhythmias, congenital heart disease, and cardiomyopathy, coronary artery disease is characterized when the arteries that provide blood to the heart become narrowed or even blocked due to the buildup of plaque in the inner walls of the arteries [5, 6] as shown in **Illustration 1.1.**
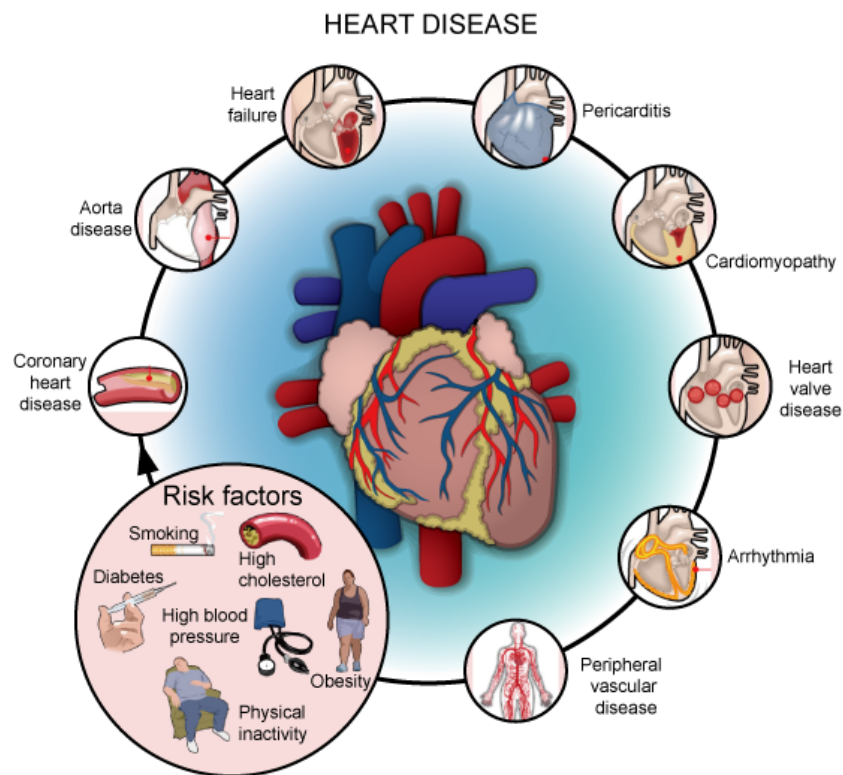
Illustration 1.1: Multiple forms of heart disease with various conditions that affect the heart and blood vessels. Symptoms of cardiovascular disease vary from shortness of breath and fatigue to chest pain and irregular heartbeat. This illustration is obtained from [1].

The constriction of coronary arteries is due to the accumulation of fatty plaque compromised of low-density lipoproteins (LDL) and degraded collagen [5]. Although coronary disease starts to appear at a late stage, it begins at an early age and progresses slowly. In the state of myocardial ischemia — when the myocardium is unable to get enough blood flow — chest pain (angina) and shortness of breath may result from [4, 7]. As less blood can flow through the arteries, a complete blockage of blood circulation may result in a heart attack [7], as shown in **Illustration 1.2**. The most common risk factors contributing to heart disease include an unhealthy diet, tobacco, excessive use of alcohol, and physical inactivity [8]. Other behavioral risk factors may include high blood glucose, obesity, and high blood pressure [5, 8].
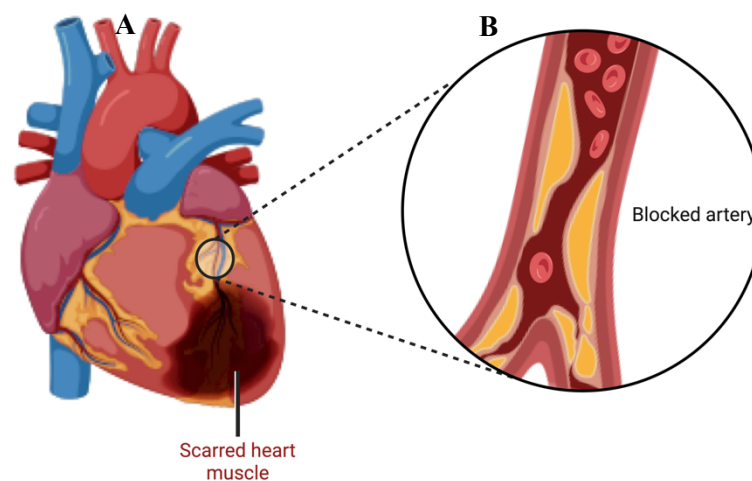
Illustration 1.2: (A) An overview of a heart and a coronary artery showing scarring of the heart muscle attributed to a heart attack. (B) A cross-section of the coronary artery with a plaque build-up and a blood clot. Illustration produced in BioRender.

Patients with coronary artery disease risk having blood clots causing a heart attack, also known as myocardial infarction (MI). MI may lead to heart failure causing cardiac dysfunction when the plaque within the artery burst and the body's blood clotting mechanism triggers an immune response. As a result, a blood clot forms and hinders the blood flow and oxygen to the myocardium causing permanent damage to the surrounding area. Coronary angioplasty is a

percutaneous intervention used to expand severely narrowed coronary arteries that nourish the heart in addition to arteries with an atherosclerotic plaque in other body parts. The non-surgical procedure uses a short mesh-like tube structure or balloon inserted into the blood vessel to dilate and enhance blood flow, as shown in **Illustration 1.3.** Angioplasty can alleviate chest pain and is often performed to mitigate the degree of damage caused by the blocked artery. The operation is carried out under local anesthesia and does not require more than two days of hospitalization.
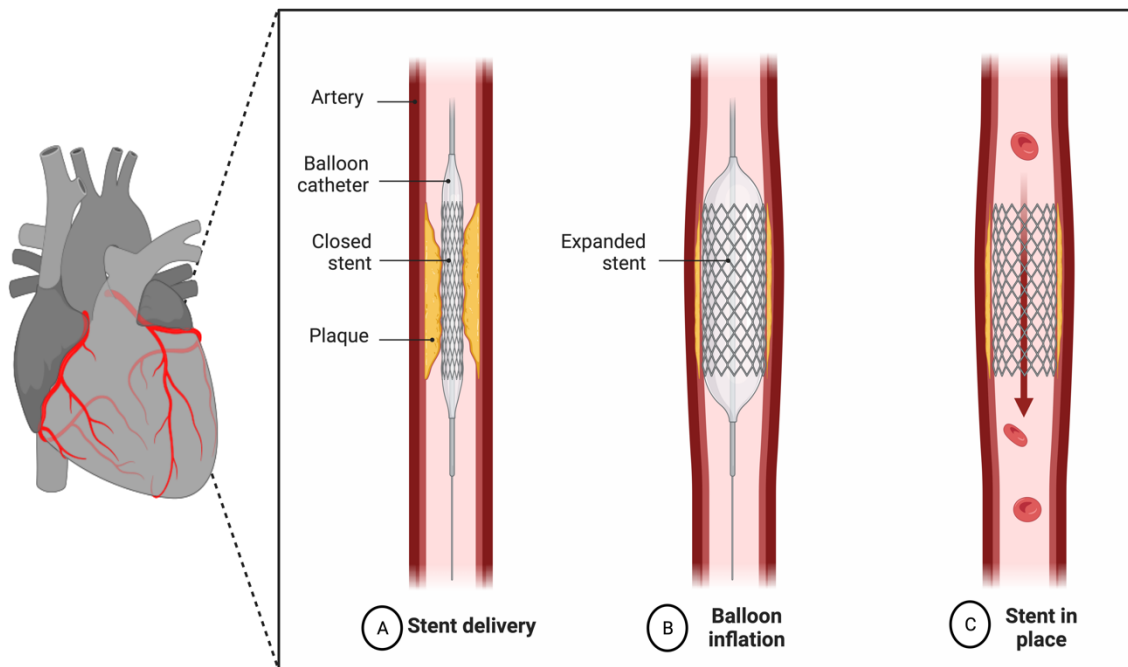
Illustration 1.3: Rendering of coronary balloon angioplasty and stent placement. When a significant blockage is found, (A) a stent delivery catheter is inserted and placed in the location of the plaque. (B) The balloon of this catheter opens the stent. (C) Finally, the balloon is deflated and removed along with the elastic tube leaving the stent to hold open the artery. Illustration produced in BioRender.

Various medications are available to help lessen the effects on patients with heart disease and serve as the first line of treatment. Statins include drugs that can lower harmful cholesterol levels and therefore reduce the build-up of plaques in the coronary arteries.

1.2. Engineering Cardiac Tissue: The Building Blocks

Organ transplantation is one of the significant breakthroughs of the century [9, 10]. Yet, its unavoidable side effects and shortage of donors put the patient at increased risk for organ rejection [10]. Although life-long immunosuppressive drugs have considerably increased graft success rates, recipients are at risk of life-threatening infections and even developing cancer and other severe age-related diseases [9]. Nothing illustrates this journey better than the cardiac field. The mammalian heart is among the least regenerative organs in the human body [11]. The lack of a regenerative capacity makes heart disease a growing problem that current therapies cannot unravel [6-8]. During disease, the myocardial architecture is disorganized leading to irregular heart contractions and stiffening of the organ due to extreme collagen buildup [12]. Stem cell therapy was hoped to provide a new mechanism to regenerate an injured myocardium [12, 13]. Initially, incredible breakthroughs enticed the swift progression toward clinical trials but the main goal, which was the improvement in cardiac function, failed in most cases, and no genuine regeneration of the myocardium was achieved with stem cells. One of the most evident understandings was that cells are not alone embedded in a tissue but surrounded by an extra-cellular matrix (ECM) not only affecting the architectural constituent but also a determinant of functionality [13]. One of the main objectives of cardiac tissue engineering is the fabrication of myocardium-like scaffolds with a surrounding matrix capable of reproducing conditions of native heart tissue with the addition of the most prominent cardiac cells [12]. Cardiac tissue engineering holds promise to reshape scientific research and immediate treatments with methods that focus on in-vitro studies in which cells are seeded onto a 3D polymeric scaffold propelling new therapeutic designs for clinical treatment [11, 12, 14]. As knowledge and understanding of how the extra-cellular matrix affects cardiac cell behavior, its main objective has greatly

expanded into domains such as disease modeling and drug testing. Most cells constituting the heart's structure are cardiomyocytes, fibroblasts, endothelial, neurons, and smooth muscle cells. Therefore, the interactions between these cells can significantly influence the aspects of cardiac biology [14, 15]. While CMs are the largest by number volume, endothelial cells and fibroblasts play a crucial role in tissue function and homeostasis [11]. Cardiac fibroblasts have been shown to be the chief cell type responsible for secreting and remodeling the collagen matrix through a degradation-deposition equilibrium [11].

Cell culture is extensively used as an in vitro tool in cell biology to enhance our understanding of the mechanisms of diseases, drug interactions, and the development of the nascent field of tissue engineering. Despite the simplicity of producing and conserving two-dimensional (2D) cell cultures, limitations such as failure to mimic the *in vivo* microenvironment remain a concern [13, 16]. Optimizing the microenvironment conditions may allow for a better understanding and facilitate the study of biomarkers and targeting therapies. Although 2D cell cultures are broadly used in in-vitro research, they are ineffective in fully simulating the native human tissue architecture, preventing the discovery of potential therapeutic targets [16]. 3D bioprinting is an additive manufacturing process with non-toxic biomaterials, living cells, and active biomolecules that aim to fabricate structures that mimic natural tissue characteristics and an extracellular matrix (ECM) environment capable of sustaining cell adhesion, proliferation, and differentiation [17-19]. Three-dimensional (3D) spheroidal structures are believed to be the most accepted models for 3D in vitro culture; therefore, engineering 3D spheroidal myocardial tissue scaffolds offers several advantages to study human heart biology, physiology, and pharmacology [12, 20-24].

In the preceding section, the hypothesis and specific aims have been conceptualized to realize the objectives of this dissertation.

1.3   Hypothesis and Specific Aims

The central hypothesis of this dissertation is utilizing 3D bioprinting to fabricate a 3D spheroidal hydrogel scaffold that provides enhanced habitat for tissue formation allowing a homogeneous distribution of oxygen, media, growth factors, therefore serving as a superior cardiac model in terms of mechanical properties, cell viability, proliferation, heterocellular coupling of cardiac fibroblasts and cardiomyocytes in-vitro.

In a follow-up proof-of-concept study, we employed this newly developed spheroid model to elucidate the mechanism of doxorubicin, an anti-tumor agent, that causes cumulative and dose-dependent cardiotoxicity, ranging from perplexing changes in myocardial structure and function to severe cardiomyopathy and congestive heart failure that may result in cardiac death.

I.   <u>**Specific Aim I:**</u>

  A. Development and optimization of a droplet printing protocol using medium viscosity alginate and gelatin to 3D bioprint spheroidal scaffolds.
  B. Structural characterization, mechanical testing of the 3D printed droplets, and proof of long-term stability.

II. <u>**Specific Aim II:**</u> Evaluation of cell viability, proliferation, and heterocellular coupling of cardiomyocytes and cardiac fibroblasts in the 3D bioprinted spheroidal droplets.

III. <u>**Specific Aim III:**</u> Adoption and application of the 3D bioprinted spheroidal droplets as a high throughput screening model for drug cytotoxicity testing.

A. Evaluate the cytotoxic effects of DOX on CMs.

B. Evaluate the cardioprotective effects of NAC and Tiron in the presence of DOX.

C. Evaluate the induced cardiotoxic effects of DOX using caspase-3 activity assay on CMs.

D. Evaluate the induced cardiotoxic effects of DOX using dihydroethidium (DHE) staining.

E. Evaluate the induced cardiotoxic effects of DOX on CMs using a flow cytometer.

Chapter 2: Research Strategy, Materials and Methods

To meet the above specific aims and to fulfill the requirements of this dissertation, the preceding scientific methods and techniques were addressed punctiliously in the optimization, fabrication, and analysis of the engineered cardiac scaffolds.

2.1   2D and 3D Cell Culture Systems

Two-dimensional (2D) cell culture techniques have been the method used by researchers to culture cells since the early 1900s [25]. In 2D cell culture systems, cells are grown as a monolayer on flat dishes with plastic-coated surfaces where they attach and expand. The early success attributed to the 2D cell culture-based system can be ascribed to its gaining ubiquitous acceptance since the early 1940s, its relatively simple and low-cost maintenance, the presence of numerous comparative pieces of literature, and its ease of analysis compared to other cell culture systems [25, 26]. Other methods such as 3D cell culture have gained traction in studies targeting cell morphology, proliferation, adaptation to stimuli, and drug cytotoxicity assays due to the 3D culture's potential to simulate in-vivo-like conditions while in vitro. 3D cultures can be more physiologically relevant than 2D cultures since such designs offer a superior degree of complexity better representing how various cell types interact [26]. Despite the fact that 3D cell culturing techniques are still in their infancy stages, the latter is beginning to surpass old 2D culture methods [27]. In fact, 3D culture systems resemble the cellular microenvironment of native in vivo tissues providing a more realistic approach for assessing accurate data about cell interactions, and proliferation when compared to results obtained in 2D cells [19, 25]. Scaffold-based techniques such as hydrogels and scaffold-free techniques such as hanging drop microplates each provide their set of applications and advantages [27, 28]. Moreover, 3D cell culture offers the potential to learn about organ behavior, narrowing the gap between 2D cell culture and animal models [16, 26, 29].

2.2   Different Types of Bioprinting Techniques

In tissue engineering, bioprinting technology has shown potential in fabricating hydrogel scaffolds and in vitro organ and tissue mimics [18, 30, 31]. The concept of bioprinting utilizes biomaterials compromised of cells and growth factors known as the "bioink" to manufacture potential tissue constructs [30]. In addition, properties such as biomimicry, scalability, resolution, and mechanical/structural stability should be assessed [18]. Even though the significance of each attribute depends on the selected bioprinting method, shared characteristics such as being commercially available, rapid gelation, and low viscosity are highly desirable. Shear thinning is one of the most critical properties of a bioink [32, 33]. Because it is inevitable to limit the shear stress exerted by the walls of the selected nozzle during the extrusion process [34], a hydrogel with suitable shear-thinning increases cell viability by providing protection during the extrusion process [34, 35]. The most commonly used bioprinting techniques are divided into extrusion-based bioprinting **(Illustration 2.1)**, inkjet-based bioprinting, and laser-assisted bioprinting [36]. Inkjet bioprinters are considered one of the first methods used in bioprinting and can be self-assembled with modest effort [37]. It is a form of non-contact printing technique where the desired volume of a bioink is expelled onto a pre-defined spot of a substrate in the form of droplets propelled by thermal or piezoelectric techniques in small amounts [37]. When a thermal element is used, a rise in temperature generates a vapor bubble at the tip of the nozzle, thereby splitting the droplet from the reservoir and expelling it out. With the piezoelectric method, as the voltage changes throughout the printhead, it will increase in volume releasing the droplet [37, 38]. On the other hand, Laser-assisted bioprinting has been mainly used for creating 2D cell patterns with high resolution and cell density [39]. The setup comprises a laser source, a receiving substrate, and a ribbon covered with a liquid biological substance [40].

In recent years, research performed using extrusion-based bioprinters has evolved swiftly while laser-assisted 3D bioprinting has been slowly decreasing in popularity, and inkjet-based 3D printers haven't witnessed notable changes in adoption.

In extrusion-based bioprinting, the bioink is released or extruded from the nozzle by air pressure. The bioink is extruded in the form of a continuous filament printed in a layer-by-layer fashion on the surface of a substrate placed on the printer's bed. The flow speed of a bioink is managed by the pressure and inner diameter of the nozzle. Relatively high-viscous bioinks can be hard to extrude and can cling to the nozzle, thus blocking it without it reaching the desired surface. On the other hand, low-viscosity bioinks percolate easier, even without added pressure. A summary of all three techniques is summarized in **Table 2.1**.
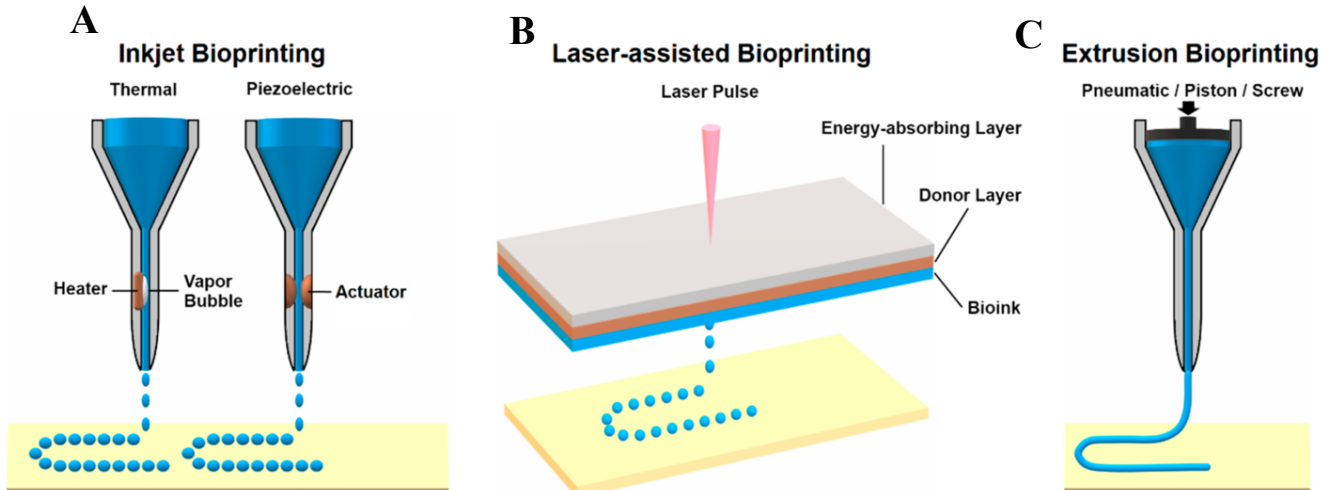
Illustration 2.1: Schematic of inkjet, laser-assisted, and extrusion bioprinters. (A) The printheads in thermal inkjet printers are electrically heated to create air pressure that forces droplets from the nozzle, while acoustic printers produce pulses formed by piezoelectric or ultrasound pressure. (B) Laser-assisted printers use lasers focused-beam on an absorbing

substrate to produce pressures that drive cell-containing materials onto a collector substrate. (C) Extrusion printers use pneumatic dispensing systems to extrude a continuous flow of cell-containing material. This illustration is obtained from [2].

Table 2.1: Characteristics of the different 3D bioprinting methods used in tissue engineering applications. The information in this table was obtained from [41].

3D bioprinting method	Inkjet	Extrusion	Laser-assisted
Actuator	Temperature/voltage	Pressure	Laser
Bioink viscosity	Low (1-15mPa/s)	High (30-60x10^{7}mPa/s)	Wide range (1-300mPa/s)
Mechanical/Structural stability	Low	High	Low
Print speed	Fast	Slow	Medium
Resolution	High (0.5-50 um)	Moderate (~200um)	High (~1um)
Cell viability	70-90%	45-98%	>95%
Cost	Low	Medium	High

2.3: Hydrogel Scaffolds

Hydrogels are the most common and widely considered type of biomaterial used in cardiac tissue engineering [42-44]. Biomaterials in the form of hydrogel scaffolds play a substantial role in hosting cells and helping them become functional tissues. Although each design structure has a distinct design arrangement, they all have a common framework to enable biocompatibility, differentiation, proliferation and the transport of gas and nutrients. Moreover, these hydrogels must permit the formation of highly porous matrices essential for cell-cell

adhesion, ECM secretion, and vital paracrine processes where cardiac cells cultured in 3D scaffolds are in tight communication with one another through cellular junctions [29]. Recent developments have led to various types of biomaterials (synthetic, natural, or composites) capable of being crosslinked via chemical, light-activated, or pH mechanisms. Origins can be from human tissues, animals, or natural sources [42]. The constitution and design of tissue-engineered hydrogel-based constructs must be defined by parameters such as mechanical properties, degradation, and cell attachment moieties [45, 46]. Hydrogels are cross-linkable polymers capable of absorbing a considerable amount of water, allowing efficient circulation of solutes from within the interconnected network [33, 47]. One of them is gelatin which is obtained through the irreversible denaturation of collagen proteins which has been regarded as a promising candidate for various tissue engineering applications [48, 49]. It is mainly derived from natural sources such as skin, ligaments, and bones. In addition to being readily soluble and possessing properties such as low toxicity and biodegradability, gelatin contains the RGD sequence (Arginine-Glycine-Aspartate) that enables cell attachment, migration, and proliferation befitting with various biomedical applications [49].

Alginate is a biomaterial obtained naturally from algae and is often used in the fabrication of tissue-engineered scaffolds due to its biocompatibility and biodegradability [33, 50, 51]. Alginate-based biomaterials have been extensively used in wound dressings because of their ability to maintain a physiologically stable microenvironment by minimizing bacterial growth, thus facilitating wound healing [44]. Alginates are composed of building blocks of (1,4)-linked β-D-mannuronate (M) and α-L-guluronate (G) chains. Alginate-based scaffolds can be prepared by various cross-linking methods, such as using calcium chloride ($CaCl_2$), one of the most abundant and often used agents to ionically cross-link alginate [52]. Because the composition of

alginate-gelatin scaffolds can be tunable, these scaffolds have been used in 3D bioprinting to achieve geometric precision and acceptable mechanical properties to maintain structural resemblance to the ECM found in native tissues [52-54]. Other essential components of the cardiac matrix include fibronectin, glycoproteins, and laminin, which play an effective role in cell differentiation, migration, and proliferation [55]. In an attempt to engineer tissue, it is vital not only to shape the ECM and its architecture but also the tissue's biophysical and biochemical properties [14, 15, 56, 57].

2.4   Scanning Electron Microscopy

To acquire details and knowledge about the hydrogel scaffold's topography, and morphology, a scanning electron microscope (SEM) was used [58]. A beam of high-energy focused electrons is produced by an electron gun which is then accelerated by a positively charged anode [59]. The beam then travels and is focused via an electromagnetic field to finally reach the sample, where electrons are emitted, producing an image on the screen. Since the Broglie wavelength of electrons is substantially smaller than that of light, the resolution is finer and superior to that of a light microscope [59]. The procedure is performed in a sealed chamber under vacuum to avoid vibrations, noise, and the scattering of electrons with air molecules [58, 59].
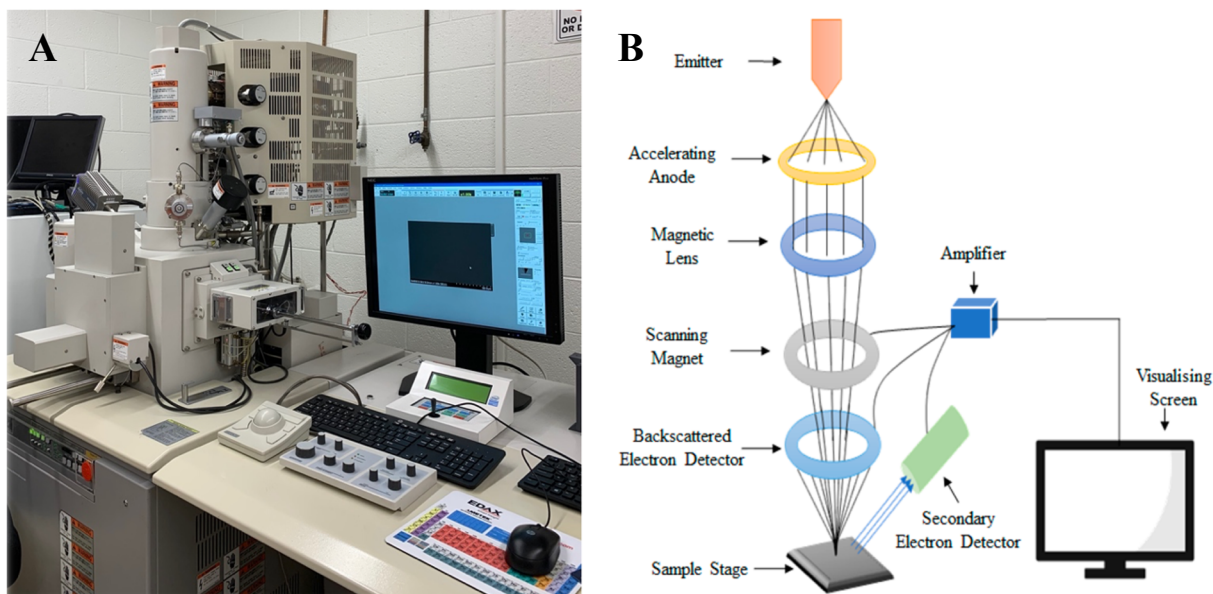
Illustration 2.2: Scanning electron microscopy setup and its schematic diagram. (A) A Hitachi S-4800 – property of UTEP was used to capture high-resolution images. (B) Schematic diagram displaying the core components of an SEM microscope and its operating principle obtained from [3].

2.5   Rheology

Hydrogels are 3D porous materials that have the ability to entrap considerable amounts of water, making them an attractive tool that can be used in biological applications such as microfluidics, tissue engineering, and drug delivery [60]. Rheology is known as the measure of flow and distortion behavior of liquids and solids – an ideal technique to study various compositions of hydrogels and their relative degree of crosslinking [61]. Because a hydrogel's properties can change when it absorbs water, scientists must be able to study its behavior under different conditions. Essentially, hydrogels are viscoelastic – displaying viscous and elastic properties [60]. Oscillatory rheology characterizes these biomaterials using key quantitative measurements. Loss modulus (G'') measures the energy lost as a hydrogel scaffold when it deforms and restores its native configuration [62]. Storage modulus (G') represents how much

energy needs to be exerted to deform the sample, and Tan δ is the ratio of loss to storage moduli which evaluate the damping capacity of a hydrogel scaffold [63]. When G'>G'', the material is regarded to possess more elastic solid properties. Inversely, when G''>G', the material is regarded to possess more liquid-like properties [62]. In our study, an Anton Paar MCR92 rheometer with a 25mm parallel plate was used to characterize our 3D bioprinted scaffolds.
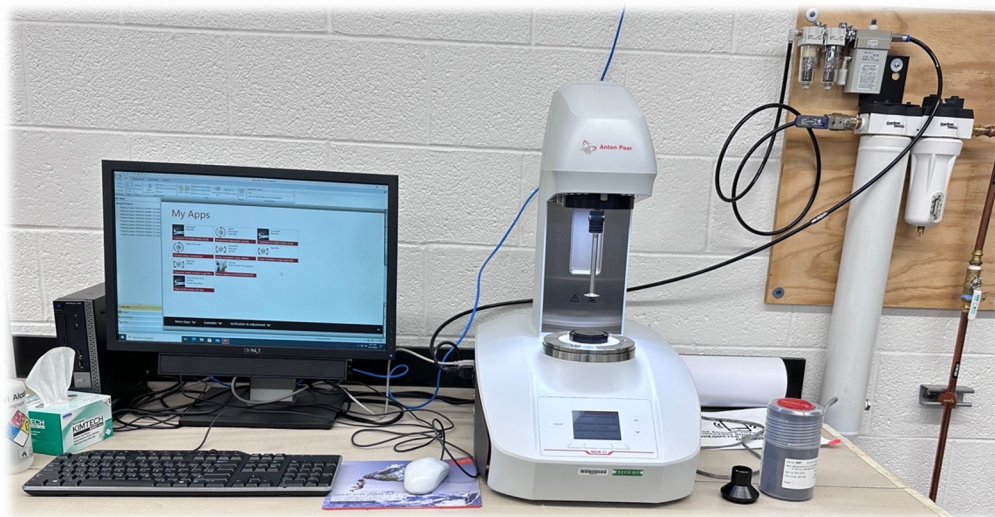
Illustration 2.3: An Anton Paar MCR 92 used in the rheometric characterization of 3D bioprinted hydrogel scaffolds – property of IMSTEL (UTEP).

2.6   Swelling and Degradation

Swelling and degradation behaviors of 3D matrix hydrogels as known to control and balance various aspects of cellular behavior [64]. A swelling assay is a technique used to examine the hydration capacities of hydrogels as a function of time. One way to adjust the rate of swelling and degradation is to increase the cross-linking density of the polymeric chains constituting the bioink by increasing the polymers compositions [64, 65]. Although this might decrease the rate of degradation, this also results in a smaller mesh and interconnected network,

which leads to a decrease in the transport and traffic of overall nutrients, growth factors, media, and oxygen [66]. In addition, this could also lead to a change in the biomaterial properties affecting the biology of the encapsulated cells [67]. Developing new strategies to regulate the hydrogel's network structure is ideal in tissue engineering applications for long-term in vitro studies.

2.7   Fluorescent Microscopy

Fluorescence microscopy has become an indispensable tool used in biology and biomedical sciences due to its unique characteristics that are not readily available in other traditional optical microscopy techniques. It is an imaging technique that permits the excitation of fluorophores and the detection of a fluorescence signal [68]. It is one of the most popular methods abundantly used by scientists to observe specific targets such as molecules within the cells, proteins, and observe dynamic processes occurring in live cells with high precision amidst non-stained elements. Because most cells are colorless and undistinguishable under a bright field microscope, the fundamental principle of fluorescence is to stain the constituents with colorful dyes [69]. Also known as fluorophores, the molecules absorb the excitation beam of electrons at a particular wavelength and emit light at a longer wavelength which is a different color from the original excited light [68, 69]. In addition, other objects can be stained with various dyes providing a clear advantage over optical imaging techniques for in vitro and in vivo imaging.
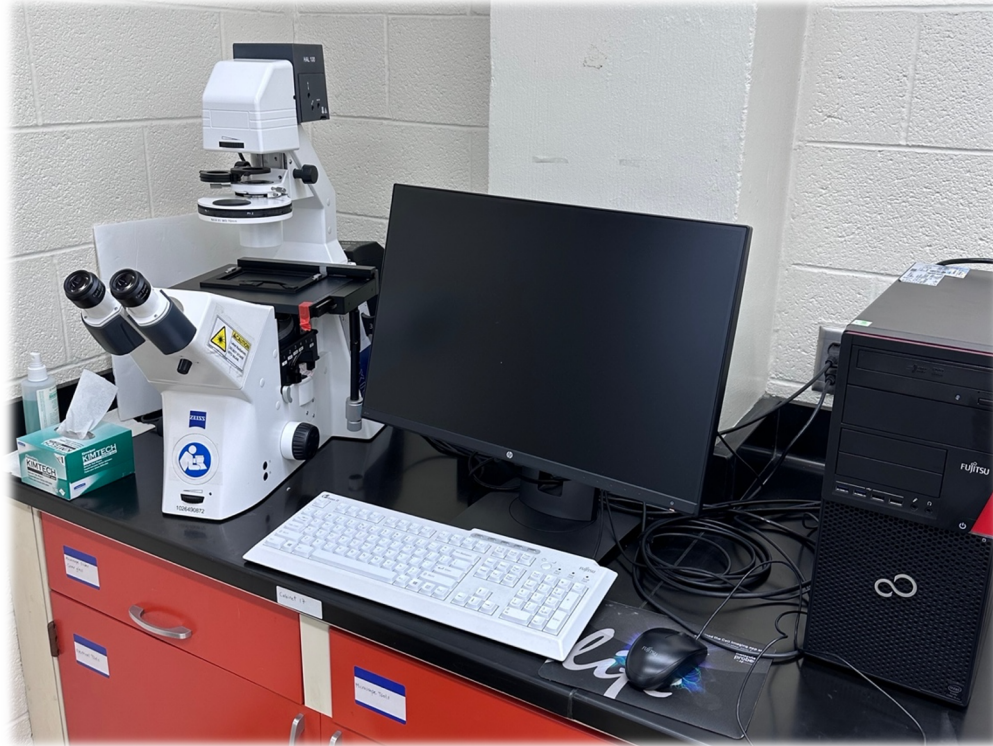
Illustration 2.4: Zeiss Axio Observer fluorescent microscope was used to capture fluorescent images included in this work – property of IMSTEL (UTEP).

2.8   Confocal Microscopy

Fluorescence microscopy has become an indispensable tool used in biology and biomedical sciences due to its characteristics that are not readily available in other traditional ooptical microscopy techniques. A confocal microscope provides numerous advantages over conventional optical microscopy, including the potential to reduce background noise from a focal plane by rejecting out-of-focus light or glare, increased visual contrast by using a spatial pinhole, and the ability to control depth of field which allows the stacking of multiple sections from a thick sample generating a 3D set of extremely high-quality images [70]. As the light emitted from the excitation source of the laser system travels through a pinhole, the laser is reflected off of the dichroic mirror and scanned over the specimen then, fluorescence is emitted from the specimen and travels back through the dichroic mirror, reaching the photomultiplier where the image is processed and forms [71]. Although they are relatively expensive to make and purchase, using a confocal microscope enables the acquisition of sharp images of a detailed structure of specific objects in high-resolution [70, 71].
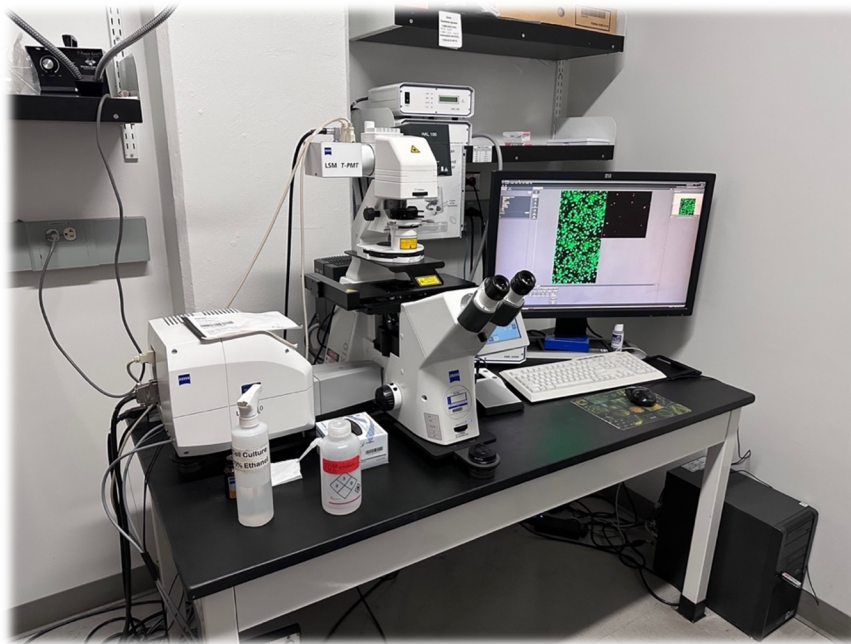
Chapter 3: The 3D Bioprinted Spheroidal Droplet

The work presented in the following chapter has been peer-reviewed and published in [45]. This chapter fulfills the requirements for *Specific Aim I* and *Specific Aim II.*

3.1   Abstract

While 2D cell culture systems are convenient and widely used in cardiac tissue engineering, the drawbacks of such a system are still of concern. Failure to emulate the in-vivo conditions and microenvironments results in variations in terms of proliferation, differentiation as well as cell-cell and cell-matrix interactions. Such limitations influenced the advent of 3D cell culture-based systems with physiological relevance to overcome discrepancies between cell assay and clinical trials. This study aimed to design and develop a high-throughput 3D bioprinted cardiac spheroidal droplet-organoid model with cardiomyocytes and cardiac fibroblasts that can be used for tissue engineering and drug cytotoxicity assays. To accomplish the desired objectives, the bioprinting parameters of a hydrogel scaffold composed of medium-viscosity alginate and gelatin were optimized and cross-linked with a calcium chloride solution. While alginate is a naturally occurring polysaccharide commonly used to model cardiac tissue, its cell adherence properties are limited and therefore has been supplemented with gelatin-containing cell adhesion moieties. Microstructural and mechanical properties of the three-dimensional bioprinted droplets after crosslinking were evaluated and found suitable for a cardiac scaffold.

Moreover, the characterization of these scaffolds revealed a highly porous and interconnected network enabling nutrients, oxygen diffusion, and waste removal. Biocompatibility and proliferation assays such as live-dead and flow cytometry exhibited biocompatibility in the 3D

spheroidal droplets supporting growth and proliferation for long-term in vitro studies. Finally, heterocellular coupling, a phenomenon that regulates the excitation-contraction machinery in the native human cardiac tissue, was studied in the 3D bioprinted scaffolds.
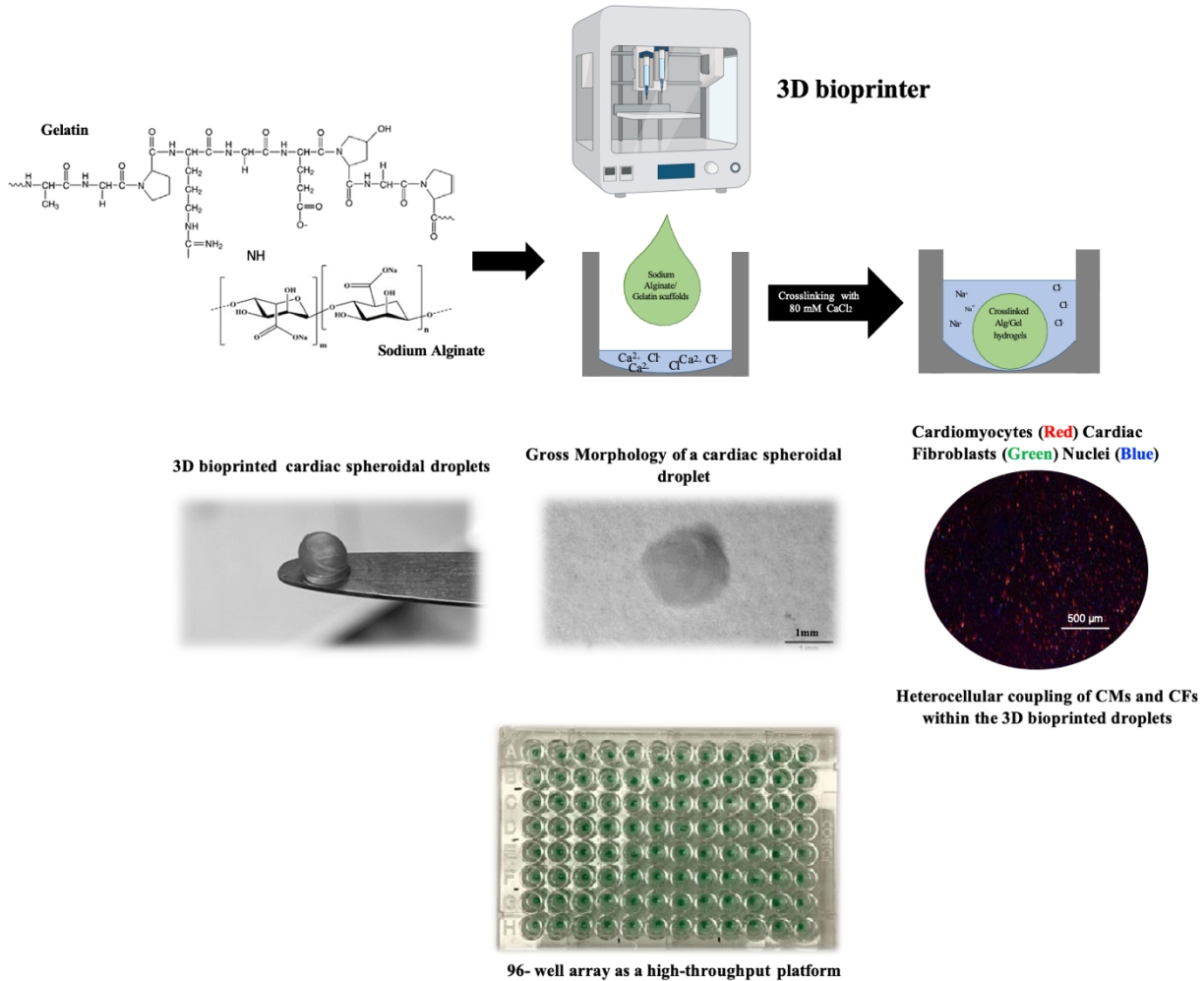
Illustration 3.1: Graphical abstract of the 3D bioprinted cardiac spheroidal droplet presented in Chapter 3 of this dissertation.

3.2   Introduction:

Mortality attributed to cardiovascular diseases has been a worldwide concern due mainly to the inadequacy of donor organ supply [72]. To successfully treat CVD, heart transplantation is generally required since the heart organ tissue is incapable of regenerating cardiomyocytes and cannot repair itself after injury [73]. Varying factors that cause such impairments include ischemic heart disease, inflammation, and congenital heart disease, may cause various pathological disorders, including loss of structure and function, leading to irreversible chronic heart failure [73]. Although several patients with advanced CVD are fortunate to gain a donor's heart, many more die in anticipation [72, 74]. In addition, several factors such as surgical complications, immune rejection, and the administration of immunosuppressive drugs cause numerous heart transplantations to fail [75].

The field of regenerative medicine comprehends numerous strategies including the use of materials and de-novo generated cells, to effectively replace damaged tissue or to contribute to tissue healing [76]. Applying cutting-edge technology to artificially construct a tissue-on-a-chip heart mimicking the function and structure of native myocardial tissue has matured to become one of the main aspirations for cardiac tissue engineering (CTE) [10, 12]. CTE aims to fabricate functional engineered tissue used as in-vitro models for research on disease mechanisms, drug discovery, and cytotoxicity applications. The most commonly used research model is the 2D cell culture-based system [25, 28]. Due to its limitations, 2D cultures are increasingly perceived as an inept model for approaching new treatment strategies and biomarkers. A rising approach to grapple with the continuously significant demand for in vitro cardiac tissue constructs is 3D bioprinting. Being a valuable tool to fabricate pseudo-human tissue mimics, many researchers have fabricated 3D cardiac constructs in-vitro in which biomaterials such as alginate, gelatin,

collagen, fibrinogen, and hyaluronic acid are generally used [45, 67, 77-80]. The physical

characteristics of biomaterials can influence and dictate printing parameters. Recent advances in

tissue engineering owe their success predominately to the development of novel biomaterials-

based strategies that better simulate native tissue and organ structures [81, 82]. These

biomaterials have the potential to harness the natural abilities of cells to sense their local

environment through cell-cell and cell-extracellular matrix (ECM) interactions and congregate

into complex networks to elucidate emergent behaviors [8, 15]. While cells grow more in a low-

viscosity environment, other characteristics, such as the average pore size and interconnectivity,

can also impact the embedded cells.

3D spheroids are considered the most commonly recognized model for 3D in vitro

culture and have recently attracted growing interest for drug screening applications and the study

of various pathological diseases [21, 83-85]. In this study, we developed a printing protocol with

optimized parameters to 3D bioprint spheroidal droplets hydrogel scaffolds in a high-throughput

fashion. A scaffold with a spheroidal design is expected to offer an improved and enriched

habitat for cellular growth, proliferation, and a homogenous distribution of media, growth

factors, and oxygen. Due to the numerous and diverse benefits of alginate and gelatin, a hydrogel

scaffold was formulated using a combination of both materials, and a droplet-based extrusion

printing technique was implemented to 3D bioprint spheroidal droplets using a BIO X 3D

bioprinter. After optimizing the printing parameters, a high-throughput fashion of the droplets

was carried out using the Advanced BioAssemblyBot (BAB), an industrial-grade bioprinter

equipped using a six-axis robotic arm. The printed constructs were characterized for their

swelling properties, microstructural porous, interconnected network, mechanical integrity, and

structural stability. The resultant 3D bioprinted spheroidal droplets with cardiomyocytes and

cardiac fibroblasts were analyzed for cell viability, proliferation, and the extent of heterocellular coupling was assessed for up to 21 days in vitro. The ability of the 3D spheroidal droplets to show cardiac tissue attributes can enable its use for various purposes in cardiac tissue engineering in addition to its adoption as a high-throughput drug screening and cytotoxicity purposes, as will be described in the upcoming chapter.

3.3   Materials and Methods

3.3.1   Chemicals and Cell Culture Reagents

Medium viscosity alginic acid (MP Biomedicals LLC, Illkirch, France) and gelatin type A (MP Biomedicals LLC, OH, USA) were mixed to form the hydrogel mixture. Sodium citrate and ethylenediaminetetraacetic acid (EDTA) were procured from Fisher Scientific. Calcium chloride solution was created from calcium chloride dihydrate (Fisher Scientific, MA, USA) mixed with phosphate-buffered saline 10x solution (Fisher Scientific, MA, USA) as an ionic cross-linker for the hydrogel scaffolds. For structural analysis, Castor oil USP (Walgreens CO, IL, USA) was used to suspend the printed spheroidal droplets. Cardiac fibroblast complete growth medium (Cell Applications, CA, USA) was used as such to culture CFs, and the CMs were cultured and expanded in Dulbecco's modified Eagle medium (Sigma, MI, USA) containing 2 mM L-glutamine (Sigma, MI, USA), FBS (Sigma, MI, USA) and 1x penicillin-streptomycin solution (Sigma, MI, USA). CellTrace Violet proliferation kit (Invitrogen, Carlsbad, CA) and DAPI (Thermo Fisher Scientific, MA, USA) were used for cell labeling. In addition, 96 round-bottom well plates and 24 and 6 flat-bottom well plates (Thermo Fisher Scientific, MA, USA) were used for bioprinting and cell culture, respectively, and Trypsin-EDTA 0.25% phenol red (Thermo Fisher Scientific, MA, USA) for cell detachment; 3-(4,5-dimethylthiazol-2-yl)-5-(3-carboxymethoxyphenyl)-2- (4-sulfophenyl)-2H-tetrazolium (MTS;

G3580, Cell Titer 96 Aqueous One Solution Cell Proliferation Assay) (Promega, WI, USA) was used for cell viability assays. The LIVE/DEAD® Viability/Cytotoxicity Kit (Thermo Fisher Scientific, MA, USA) was used to image the extent of the viability of cells. Multitissue dissociation kit 1 (Miltenyi Biotec GmbH, Bergisch Gladbach, Germany) was used to enzymatically digest the hydrogels for cell extraction, and 4% PFA (Janssen Pharmaceuticals, Belgium) was applied for cell fixation. Click-iTTM Plus TUNEL Assay was used to detect in situ apoptosis (Thermo Fisher Scientific, MA, USA). Hoechst 33342 (Sigma, MI, USA) was used for counter-staining cell nuclei, and PKH26 Red/PKH67 Green, Fluorescent Cell Linker Kit (Sigma, MI, USA) for general cell membrane labeling.

3.3.2   Preparation of Alginate-Gelatin Hydrogels

A bioink solution of 2% w/v gelatin was dissolved in Milli-Q water (37°C) in a 5mL sterile eppendorf tube to which 3% w/v alginate was added under aseptic conditions [86]. To dissolve the hydrogel mixture, the gel mixture was vortexed and centrifuged to remove the remaining air bubbles. Hydrogel scaffolds were UV sterilized for 15 min prior to bioprinting, after which they were scooped into a sterilized syringe (CELLINK, Blacksburg, VA, USA).

3.3.3   Fabrication of 3D Bioprinted Spheroidal Hydrogels Constructs

A sphere with a radius of 1mm (R=1mm) was designed using SolidWorks® software. The scaffold design was then converted to a binary .stl file using Meshmixer®, a prototype designer tool. Using CELLINK BIO X (Blacksburg, VA, USA), the temperature-controlled printer head was used to deposit scaffolds inside a 96-round-bottom well plate. Prior to 3D printing, 5 μL of 80 mM $CaCl_2$ sterile solution was added to the bottoms of each of the designated wells. As shown in **Table 3.1**, air pressure was set between 13 and 15kPa, the speed

selected to be 0.7 mm/s, and a nozzle size of 16G (ID = 1:2 mm/OD = 1:6). After printing, the

alginate-gelatin composite scaffolds were cross-linked with an additional 75 μL of 80 mM $CaCl_2$

solution for 45 min under dynamic conditions while being placed on a Belly Dancer Shaker for

15 min (IBI SCIENTIFIC, Iowa, USA). When sodium alginate is reacted with calcium chloride,

a double replacement reaction occurs where the calcium ions replace the sodium ions on the

alginate, producing calcium alginate whereas the bi-product, sodium chloride, remains in the

solution. Moreover, each calcium ion bind to two carboxylate chains from the sodium alginate,

which cross-link the polymer chains resulting in the formation of an insoluble gel-like substance

[87].

Table 3.1: Parameters used for 3D bioprinting of spheroidal droplets

Printer Setting	Requirement
Printing Pressure	13-15 kPa
Printing Speed	0.7 mm/s
Nozzle size	16G (~1.19 mm)
Temperature	Room temperature (25-28°C)

For high-throughput droplet printing of the hydrogel, the BioAssembly-Bot (BAB) was used.

Using the TSIM (Tissue Structure Information Modeling) software, a series of identical

spheroidal droplets were designed, and high-throughput bioprinting was achieved using the same

optimized parameters as in **Table 1.1.** Using the same optimized parameters, a flattened disk

serving as a control structure was 3D printed [80]. Scaffolds were cross-linked and washed with

1x PBS (pH 7.4) for 10 minutes to remove excess $CaCl_2$ under dynamic conditions.

To test the conformity and consistency of the design structure of the 3D spheroidal

droplets, three distinct batches (each n=36) were printed. Samples were picked arbitrarily from

each of these batches and immersed in castor oil. The aspect ratio of each spheroidal droplet

sample was calculated using ImageJ by finding the relationship between the height and width

[88] as shown in equation (1):

$$Aspect\ ratio = \frac{Height}{Width} \qquad (1)$$

3.3.4   Scanning Electron Microscopy

Front and cross-sectional images of the lyophilized hydrogels were analyzed using a Hitachi, S-

4800) scanning electron microscope **(Illustration 2.4).** Lyophilized samples were sputter coated with

gold for 45 seconds and imaged between 5 and 10 kV [44, 80]. Using the energy-dispersive X-ray

spectroscopy (EDS) instrument in combination with the SEM, elemental analysis of the cross-section of

3D bioprinted hydrogel spheroidal droplets with/without cardiac cells was performed. Elemental

composition revealed the presence of carbon (C), oxygen (O), nitrogen (N), and sodium (Na) elements.

To show the difference in elemental composition between cellular and acellular scaffolds and the absence

of a necrotic core, the electron beam was focused on cells adhered to the scaffold in the core as described

by other published works [89]. Using ImageJ, an in-depth microstructural analysis was performed to

determine the average pore diameter using equation (2) below.

$$AVG\ Pore\ Diameter = \frac{\sum Pore\ Diameters}{Total\ No.of\ Pores} \qquad (2)$$

3.3.5   Swelling and Degradation

The experimental (3D spheroidal droplets) and control structure (flattened ring) were maintained

at -80°C for 24 hours and lyophilized [80]. After freeze-drying, samples were weighed (W_0) and

immersed in 1x PBS. At various time points, the samples were weighed at room temperature [35, 80]. The

swelling ratio was calculated using the formula below for samples equilibrated in PBS for up to 28 days.

$$Ds = \frac{Wi - W0}{W0} \qquad (3)$$

3.3.6 Rheological Analysis

Using an Anton-Paar MCR 92 rheometer (Anton-Paar, Austria), the rheological

properties of the experimental and control constructs was performed with a PP25/S measuring

system at 1% strain with a frequency range between 0.5 and 50Hz [90]. Prior to the oscillatory

shear stress rheometric study, hydrogels were pre-swollen in 1X PBS for 24 h, and analysis was

conducted at 1% strain with a frequency range between 0.5 and 50Hz [63] while the frequency

sweep analysis was conducted within the viscoelastic range of the gels. Storage/loss moduli,

complex viscosity, and elastic modulus were measured as previously done and reported [44, 67,

80, 90].

3.3.7 Biocompatibility in the 3D Spheroidal Droplets

A bioink solution of the alginate-gelatin mixture was prepared to which human cardiac

fibroblasts (CF, adult; Cell Applications, San Diego, CA) and AC16 human cardiomyocyte or

cardiac myocyte cell line (CM, ATCC, Manassas, VA) were mixed in a ratio of 1:1 to constitute

a final cell seeding density of 1×10^6 /ml. A complete growth media for the bioprinted scaffolds

was prepared by mixing CF and CM growth media in a ratio of 1:1. Cultures were maintained at

37°C and 5% CO_2. A Live/Dead Assay Kit was used to assess the biocompatibility of the 3D

spheroidal droplets according to the manufacturer's protocol. Calcein AM (green) represented

live cells, while ethidium homodimer (red) represented dead cells. Cell viability was quantified

using the equation below:

$$No.\ of\ live/dead\ cells\ (\%) = \frac{\#\ of\ green\ or\ red\ cells}{Total\ No.\ of\ green\ and\ red\ cells}\ x\ 100. \quad (4)$$

To confirm their heterocellular coupling, CMs were pre-stained using PKH67 (green dye), and the CFs were stained using the PKH26 (red dye) [90, 91]. The samples for HC analysis were fixed with PFA for 15min at room temperature (25-28°C) before imaging. The samples were washed with 1X PBS and mounted using Fluor mount-G with DAPI. Using an LSM 700 confocal microscope system **(Illustration 2.5)**, Z-stack projection high-magnification images were acquired for each representative sample in each group. The average coupling percentage was obtained using equation (5) below.

$$\%\ Coupling = \frac{2\ x\ (\#\ of\ coupled\ CMs\ (green)\ \&\ CFs\ (red)}{Total\ No.\ of\ CFs+CMs}\ x\ 100 \quad (5)$$

3.3.8 TUNEL Assay and Imaging

DNA fragmentation was evaluated using Click-iT™ Plus TUNEL Assay for In Situ Apoptosis Detection Kit which was used to check for the presence of a necrotic core within the 3D bioprinted cardiac spheroidal droplets. On day 7, the scaffolds were fixed in 4% PFA for 15 min and then cut in half using a blade. A staining procedure with Picolyl azide Alexa Fluor™488 was performed to detect DNA fragmentation according to the manufacturer's protocol [92]. The stained scaffolds were visualized with the appropriate filters using an LSM 700 confocal microscope system. The nuclei were counterstained with Hoechst 33342 and high-magnification Z-stack images were acquired for each representative sample in each group.

3.3.9   Flow Cytometry Analysis (FACS)

Cardiomyocytes were pre-stained using CellTrace™ Violet (CTV) proliferation kit according to the manufacturer's protocol prior to 3D bioprinting with the cardiac fibroblasts. At each time point, the 3D spheroidal droplets with cells were extracted using Miltenyi gentleMACS Dissociator (Miltenyi Biotec, Cambridge, MA) using a Multi Tissue Dissociation Kit-1 by running the Multi_B program according to the manufacturer's protocol. After 7 and 14 days, cells were fixed for 15 min using 4% PFA at room temperature and added to their designated FACS analysis falcon tubes, and analyzed with a Beckman Coulter Gallios Flow Cytometer (Brea, CA, USA) based on the excitation and emission wavelengths of 405 and 450 nm respectively.

3.4   Results and Discussion

3.4.1   Morphological Consistency of 3D Spheroidal Droplets.

Figure 3.1A illustrates the 3D printer used for high throughput printing of the spheroidal droplets (Figure 3.1B), and Figure 3.1C shows the theoretical design used for bioprinting. Figure 3.1D represents the 3D printed spheroidal droplets acquired from a gelatin and sodium alginate-based bioink using the optimized printing parameters **(Table 1.1)**. The objective of the parameter optimization was to reduce the shear stress acting on the bioink to achieve optimal geometric accuracy using the CELLINK and the BAB platforms [35, 67] while maintaining a low and constant extrusion pressure due to its inverse effect on cell viability [93]. Prior to yielding the 3D spheroidal droplets (Gen IV), three previous generations of scaffolds (Gen I-III) were realized (Appendix A.1.1) [93].
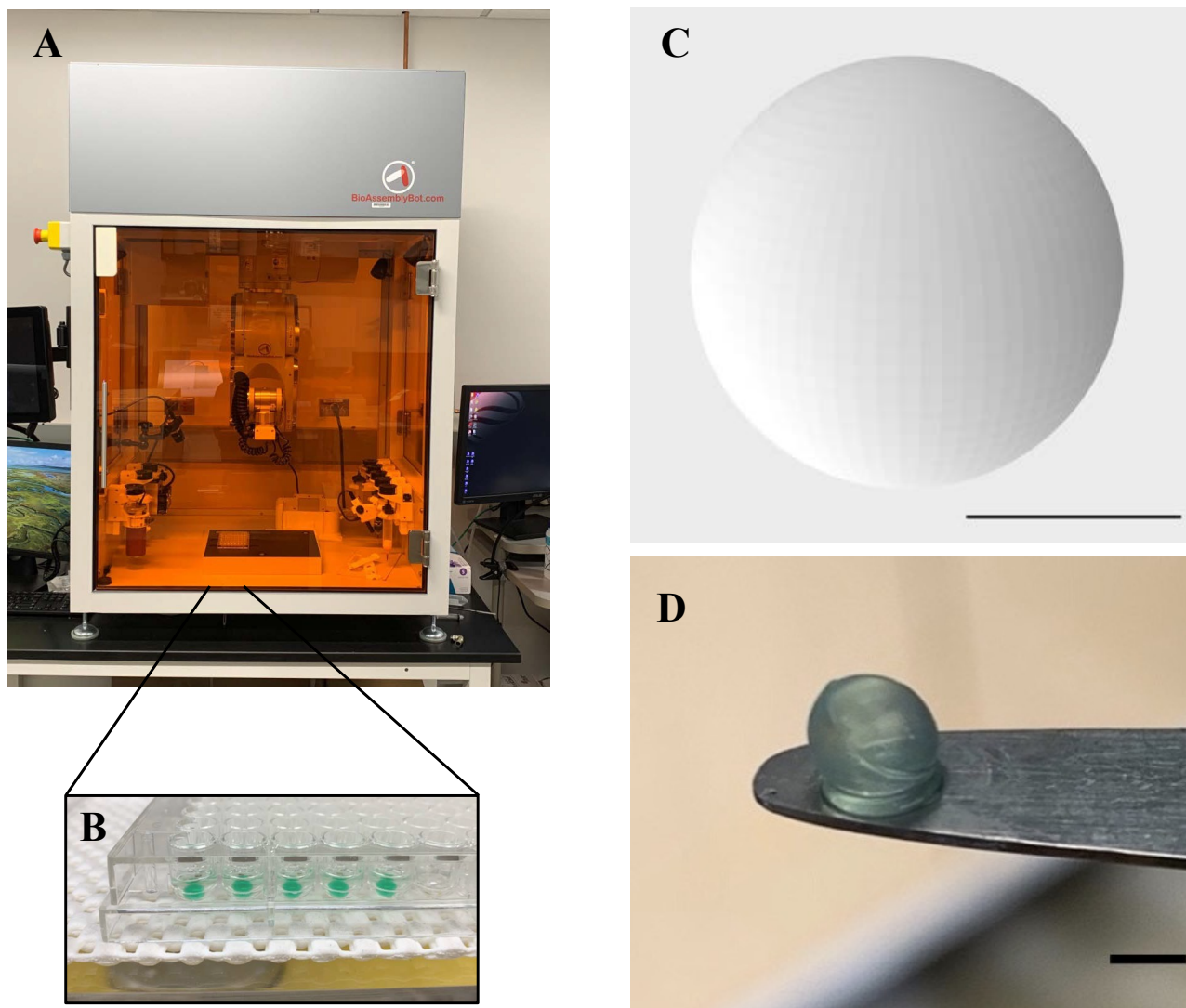
Figure 3.1: Design, morphology, and consistency of 3D spheroidal droplets. (A) The BioAssemblyBot (BAB) 3D printer is used in bioprinting spheroidal hydrogels in a 96-well plate as shown in (B). (C) .stl file image of a spheroidal droplet and shown in (D) is a gross morphology image of the 3D bioprinted spheroidal droplet. Scale bar was set at 1 mm for (C) and (D).

The immersion of the 3D bioprinted spheroidal droplets in castor oil confirmed its morphological and structural stability, as depicted in Figure 3.2A. As shown in Figure 3.2B, the aspect ratio of the 3D bioprinted hydrogel spheroidal droplets (Gen IV) was conserved between varying batches from a total of 108 samples signifying uniformity and reproducibility of the spheroidal prints using the in-house developed printing technique.
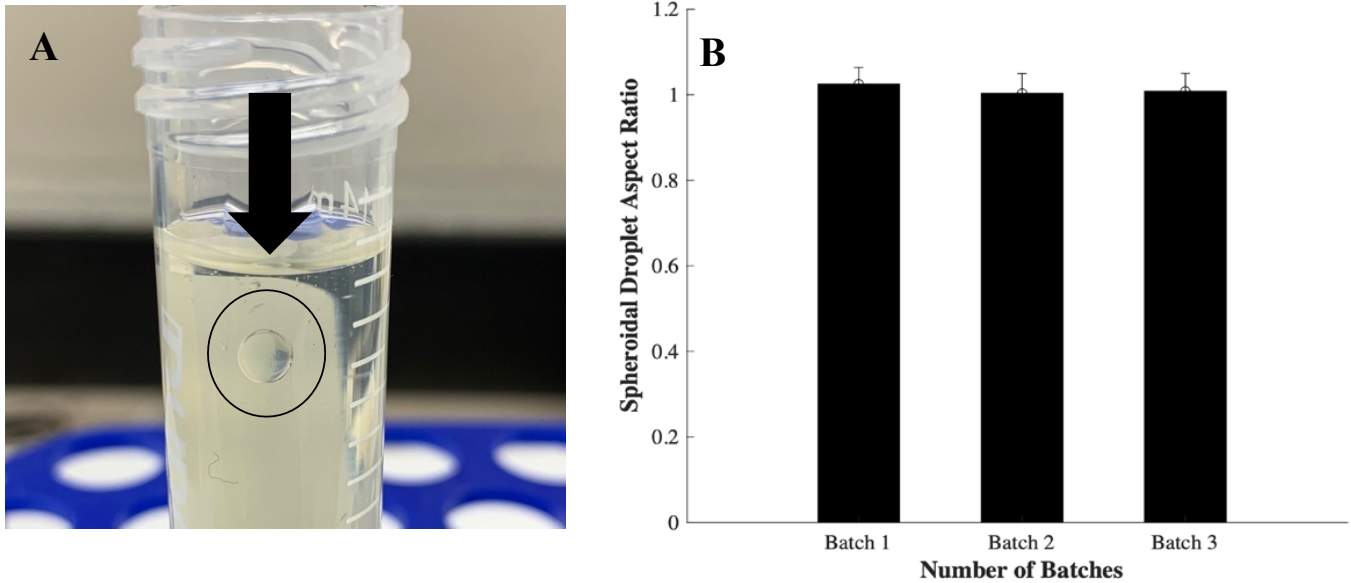
Figure 3.2: Uniformity and Consistency of 3D Spheroidal droplets. (A) Representative image showing a 3D bioprinted spheroidal droplet freely suspended in oil. (B) The aspect ratio is maintained for three consecutive 3D bioprinted batches.

3.4.2 Microstructural Analysis

Significant porosity in hydrogel scaffolds plays a critical role in cell proliferation, nutrient diffusion, migration, vascularization, and differentiation [94]. Figure 3.3A-D depicts a microstructural image of a cross-sectional surface area of a 3D spheroidal droplet (A, B) and flattened disk (C, D) conducted using a scanning electron microscopy **(Illustration 2.3)**. While the spheroidal droplets and flat discs expressed an interwoven mesh network, a significant difference in the average pore diameter was observed in the 3D bioprinted spheroidal droplets (228.67±92.07 µm) and flattened disk (63.02±29.3 µm) as depicted in Figure 3.3E (p<0.001). Tissue-engineered scaffolds require pore sizes greater than 200µm for enhanced vascularization and cell viability [95]. Moreover, a higher pore diameter contributes to a significantly higher porosity, thereby increasing the interconnectivity between the pores which enables and facilitates

31

higher cell migration and diffusion of nutrients, supplements, and oxygen more efficiently in the

3D spheroidal droplets compared to the control structures [80, 96].
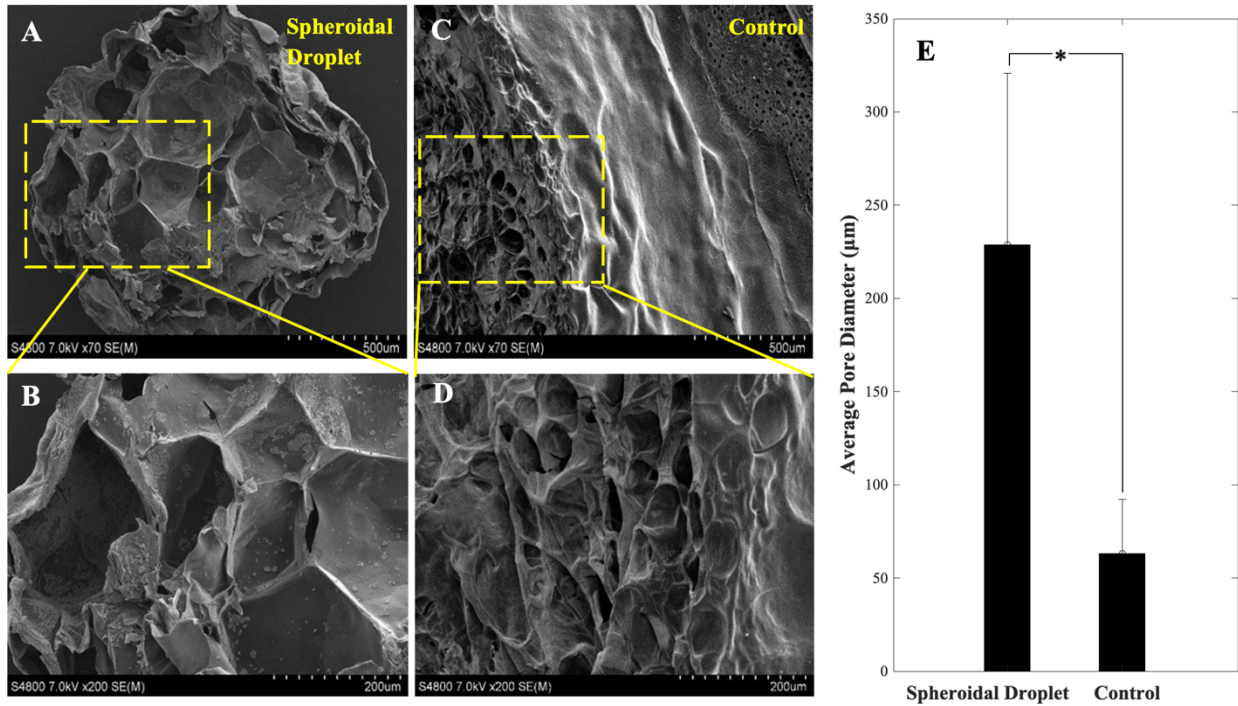
Figure 3.3: Microstructural analysis. (A, B) Representative SEM images for the cross-section of the spheroidal droplets. (C, D) Representative SEM images for the cross-sectional structures of the flattened disk structure (control). The bar graph in (E) depicts the average pore diameter of the spheroidal droplet in comparison to the control structure (n=5). The average pore diameter was found to be statistically different (*p < 0.001) between the spheroidal droplet and control samples.

3.4.3   Swelling, Structural and Mechanical Properties of Bioprinted Constructs

The degree of swelling (D_s) of the 3D spheroidal droplets and control sample is depicted

in Figure 3.4A. Due to a higher surface area-to-volume ratio and average pore diameter, the 3D

spheroidal droplets contributed to an increased swelling compared to the control structure.

(p<0.01) [97]. The spheroidal droplets were stable for up to 28 days in 1X PBS and did not

physically fragment, while the control samples started to physically decompose after 14 days. This confirms the utilization of the 3D spheroidal droplets as a long-term *in-vitro* model for cell culture studies.

The rheological characteristics of the 3D bioprinted spheroidal droplets and the control structure are represented in Figure 3.4B-D. Although both structures showed viscoelastic properties, a significant difference in the storage and loss modulus was observed between the 3D spheroidal droplets and control structure ($p<0.001$), as shown in Figure 3.4B. The storage modulus corresponds to the energy stored in the elastic structure of the sample, while the loss modulus constitutes the amount of energy lost in the sample [98, 99]. The average storage and loss moduli for the 3D spheroidal droplets was $3.84\pm0.38/0.597\pm0.054$ kPa, while control structures exhibited $1.78\pm0.05/0.188\pm0.002$ kPa. When the storage modulus is higher than the loss modulus, then the material can be considered mainly elastic. Complex viscosity, which accounts for the total resistance to flow movement as a function of the angular frequency [100], was found to be higher in the 3D spheroidal droplet model (309.78 ± 30.86 Pa·s) when compared to the control sample (143.11 ± 8.58 Pa·s) as shown in Figure 3.4C. The elastic modulus, which is a measure of the scaffold's resistance to being deformed elastically, was also studied. Similar to the storage and loss modulus, the elastic modulus of 3D bioprinted hydrogel spheroidal droplets (Figure 3.4D) was significantly higher than the control samples ($p<0.001$). While the elastic modulus of the spheroidal scaffolds was deemed to be within the range of the elastic modulus of native heart tissue (>10-15 kPa), this makes it an attractive platform to be used as a 3D cardiac

organoid model for *in-vitro* studies.
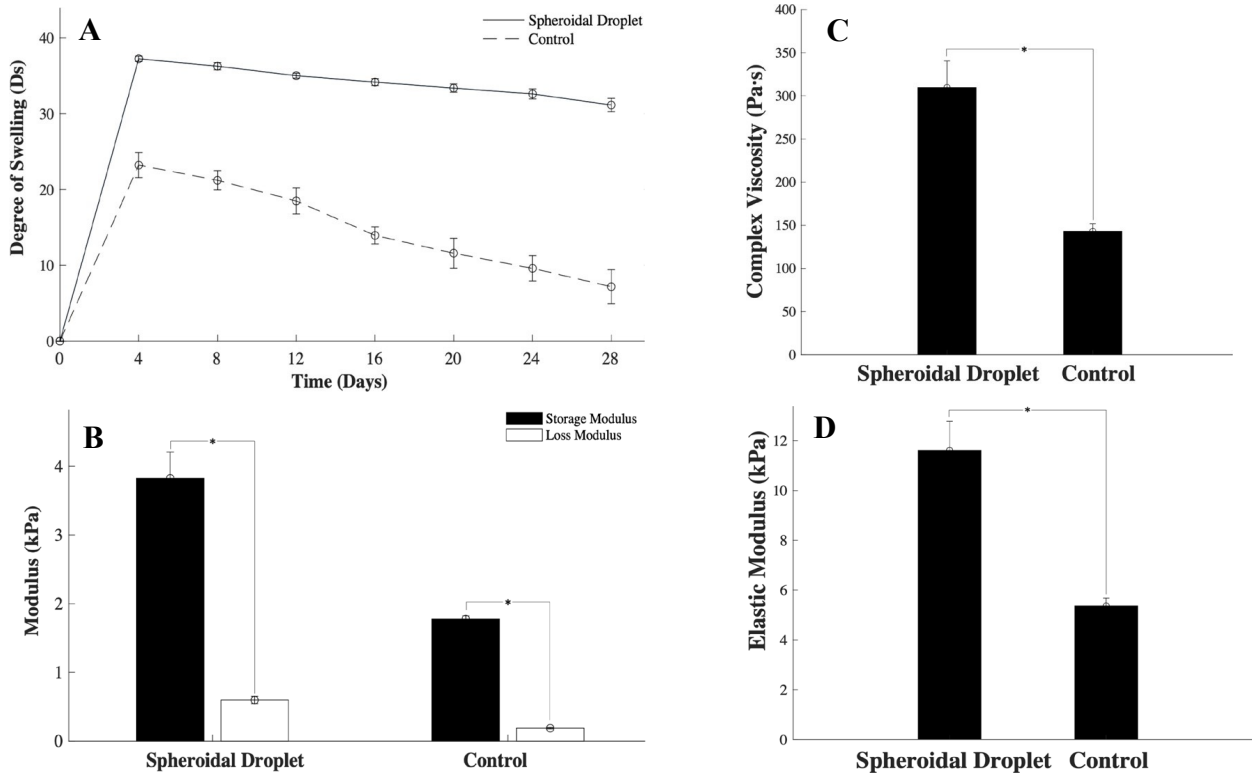
Figure 3.4: Mechanical characterization. (A) Graph depicting the average degree of swelling (mean ± SD) for spheroidal droplets (—) and control (----) structures for a period of 28 days. (B) Bar graph showing the storage/loss modulus, (C) complex viscosity, and (D) elastic modulus of the spheroidal droplet compared to the control structure. *p values were found to be all statistically different.

3.4.4   Cell Viability within the Spheroidal droplets.

After 7 and 14 days of culture, live-dead confocal microscopy images of cells within the

3D bioprinted spheroidal droplets are shown in Figures 3.5A and 3.5B, respectively. Figure 3.5C

shows no significant difference in the % of live cell viability between the two time points,

representing the steady turnover in the number of growing cells. Live-dead images from positive

34

and negative controls are depicted in Appendix A.1.3.
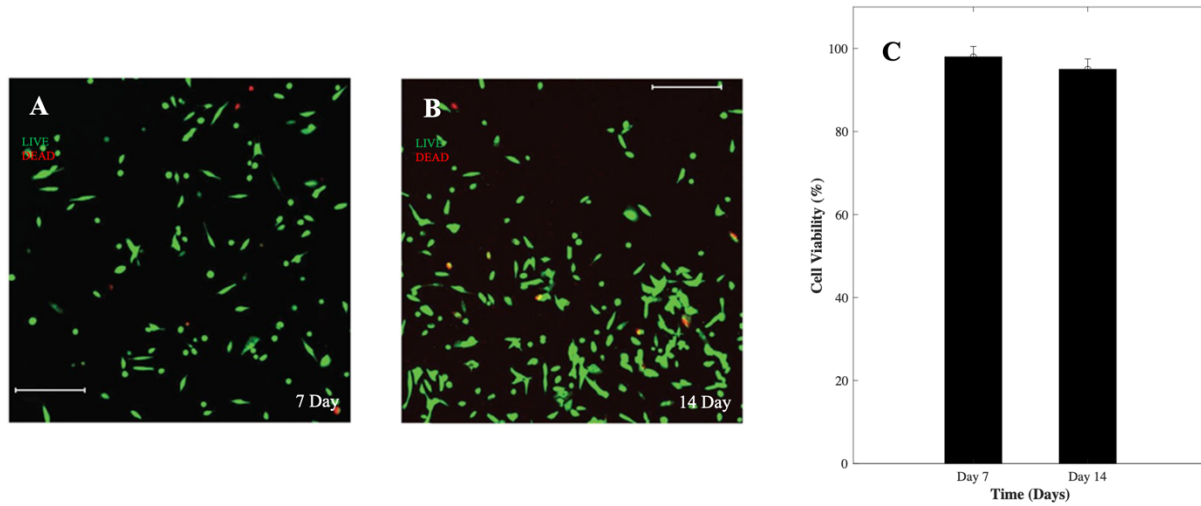
Figure 3.5: Cell viability. (A, B) The live stained cells in green by calcein AM and dead cells were stained in red by ethidium homodimer after 7 days and 14 days in culture (scale bar 200 µm). (C) Graph illustrating the % live/dead cells in both 3D spheroidal droplets and controls at 7 and 14 days, respectively. p values were found not to be statistically significant when data were compared between different time points ($p>0.05$).

To further determine whether a necrotic core was formed in the 3D spheroidal droplets containing cells, TUNEL assay were performed on the cross-section area of samples cut through the center on day 7 and assessed using a Click-iT™ TUNEL assay kit. Results showed no proof of apoptotic DNA fragments (Figure 3.6C) when all cells were counterstained using Hoechst (Figure 3.6A) confirming the absence of a necrotic core in the 3D cardiac spheroidal droplets. However, a parallel set of control samples treated with ethanol and then processed using the TUNEL assay displayed positive staining for the Alexa Fluor™ 488 tagged to TdT (Figure 3.6B).
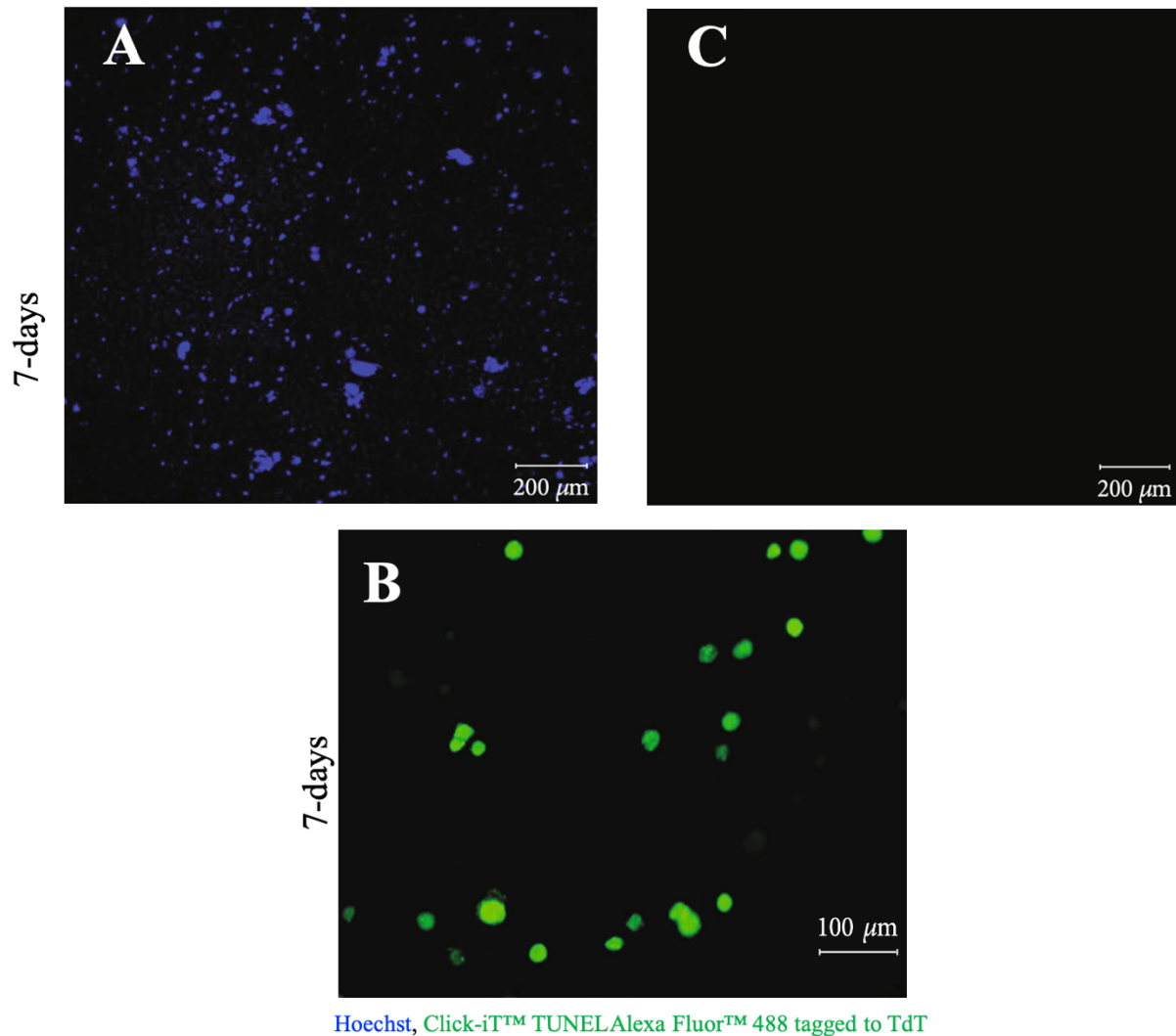
Figure 3.6: TUNEL staining of 3D spheroidal droplets. (A) All the cells were counterstained using Hoechst and (B) the presence of dead cells in the 3D spheroidal droplets. (C) The absence of evidence of apoptotic DNA fragments after 7 days in culture.

3.4.5   Heterocellular Coupling of CFs with CMs

In an attempt to mimic *in-vivo* cardiac tissue, the 3D spheroidal droplets must promote the heterocellular coupling (HC) between CMs and CFs [101]. Representative high-magnification images of CMs prestained with PKH67 (green dye) and CF prestained with PKH26 (red dye) after

14 days are represented in Figure 3.7A-D. The percent of the HC between the 3D spheroidal droplets and the control structure is illustrated in Figure 3.7E. A statistically significant difference in HC was observed between the 3D bioprinted droplets (80.33±8.38%) and control structure (53.63±5.9%) and the overlapping of both cell types validated their HC after 7 and 14 days of culture and confirmed the potential of utilizing these 3D bioprinted spheroidal scaffolds as a cardiac organoid model (p<0.05). The heterocellular coupling is consistent and maintained even after 21 days of culture, as shown in Appendix A.1.4. Furthermore, immunohistochemistry performed on the cells confirmed their respective identities as cardiomyocytes and cardiac fibroblasts with heterocellular and cell junction coupling, as shown in Figure 3.7F. Troponin-I (Trp-I; red) was used as a biomarker for staining CMs, fibroblast-specific protein-I (FSP-I; green) was used as a biomarker for CFs and DAPI (blue) as an overall stain.

CM (PKH-67), CF (PKH26), DAPI
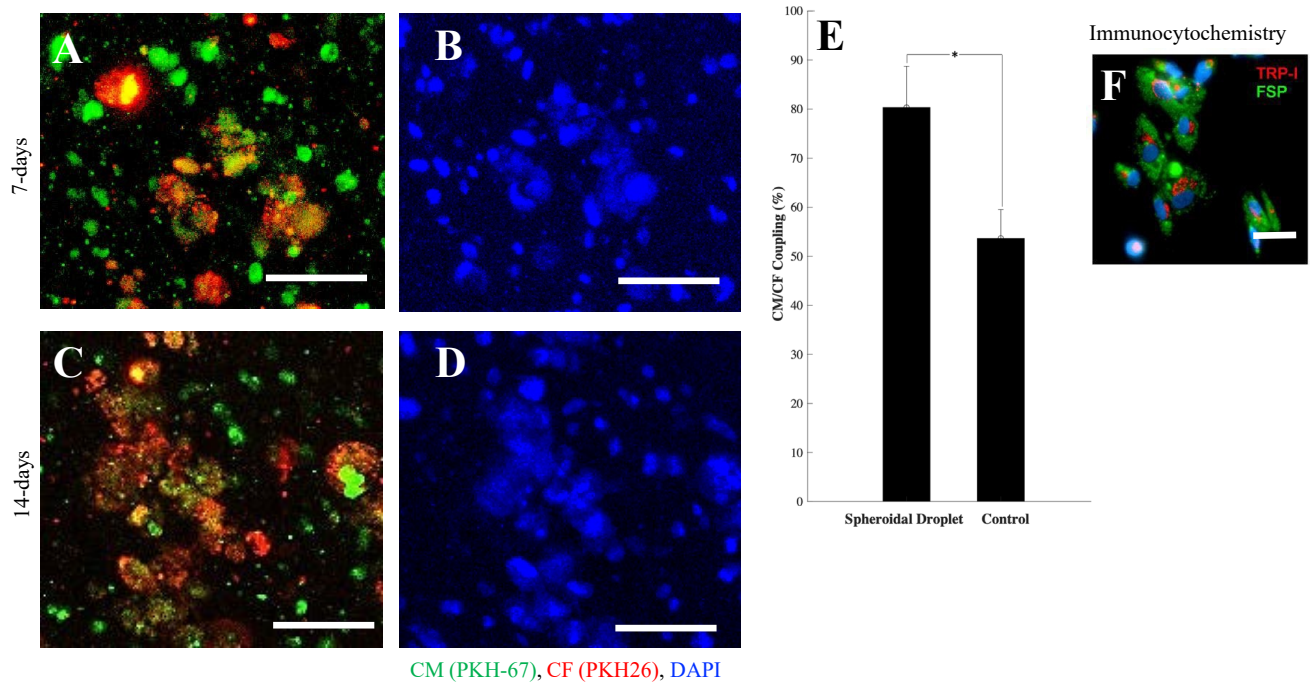
Figure 3.7: Confirmation of heterocellular coupling for cardiomyocyte (CM) and cardiac fibroblasts (CF) in the spheroidal droplets after 7 and 14 days of culture (A–D). Percent of heterocellular coupling between CM (green) and CF (red) is depicted using a bar graph in (E). The extent of coupling was found to be significantly greater in the 3D spheroidal droplets (p<0.03) compared to the controls after 7 days of culture. Immunocytochemical data for CM-CF coculture at 7 days demonstrated the presence of CM and CF as analyzed by cell marker troponin I for CM and FSP for CF and imaged as shown in (F). The scale bar used in all images is 100 μm.

3.4.6   Cell Proliferation

To evaluate the proliferation trends of CMs in the 3D bioprinted spheroidal droplets, CMs were prestained using CellTrace™ Violet (CTV) dye, whereas CFs were not stained and mixed in a 1:1 ratio. The CTV dye is used to track cell proliferation based on the concept of dye dilution of CMs when coupled with CF allowing several generations of proliferating cells to be examined. An increase in cell proliferation causes a reduction in the dye intensity over successive generations produced [102, 103]. Figures 3.8A-D represent the flow cytometry analysis of cells seeded in the 3D spheroidal droplets. Positive controls included CMs pre-stained with CTV and mixed with CF for 24 hours, after which they were extracted and analyzed. Negative controls included samples cultured using exact conditions as positive controls but without adding the CTV dye.

Figure 3.8A represents a characteristic distribution of peaks for a negative control where cells were not stained, and therefore peaks are shown in low-intensity regions to the left on the logarithmic scale. Figure 3.8B represents characteristic peaks from positive controls wherein peaks for unstained CF are partially observed in the low-intensity region on the left, and the peaks for stained CM are partially observed in the high-intensity region to the right. The characteristic peaks represented by both sets of controls can be further explained by the higher intensity in the positive control (78.83%) compared to the negative control (7.23%) on day 1.

Figure 3.8C and Figure 3.8D represent the % CTV+ collected from samples extracted after 7 and

14 days of culture, respectively. The % intensity decreased from 60.11% on day 7 to 39.62% on

day 14. Moreover, Figure 3.8E indicates a statistical difference ($p<0.05$) in the average %CTV+

between 7 days (62.23±1.83%) and 14 days (40.64±1.04%). This reduction in the dye intensity

marked the dilution of CTV dye with time, suggesting the proliferation of CMs in the 3D

spheroidal droplets. Fluorescent microscopy images for CTV dye-stained cell samples are

presented in Appendix A.1.5.
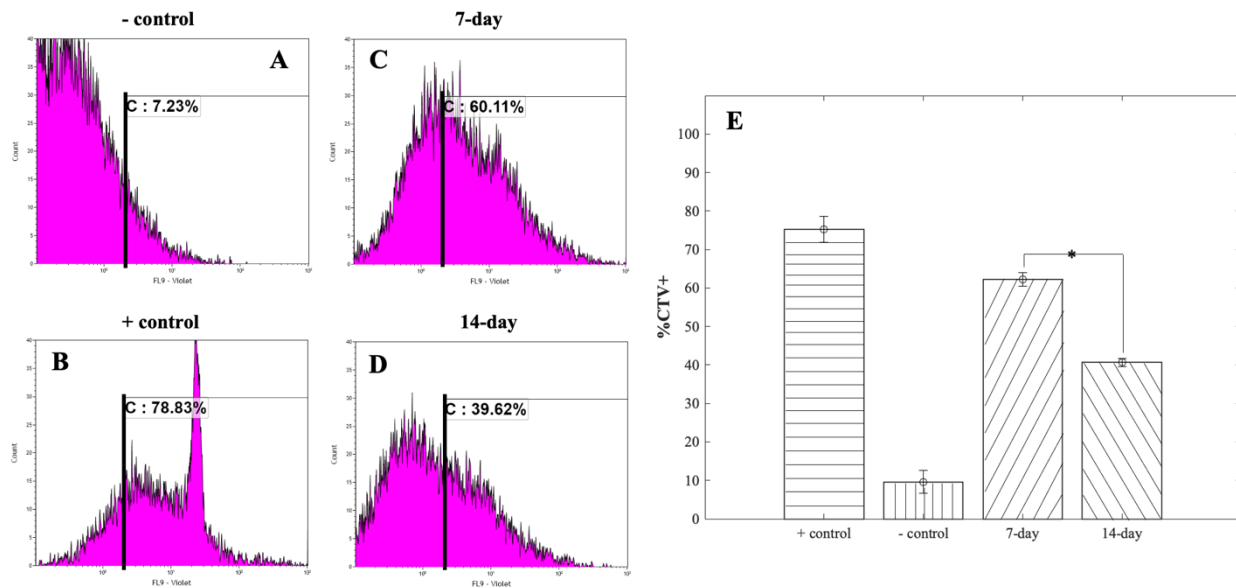
Figure 3.8: Pre-stained CMs with CellTrace Violet dye (CTV) were added to CFs and mixed
with the bioink mixture prior to 3D bioprinting. Cells were extracted and analyzed using a flow
cytometer. (A-D) Graphs depicting the %CTV+ for each experimental condition and time-point.
(E) Bar graphs representing the average %CTV+ from cells extracted from the 3D bioprinted
spheroidal droplet for each condition. *p values were found to be statistically different.

3.4.7 Conclusion

In this study, we have developed a protocol for 3D bioprinting cross-linkable alginate-

gelatin spheroidal droplets whereby the mechanical stability of the 3D spheroidal droplets and

microstructural analysis were studied and found to be appropriate for a cardiac scaffold. We then

assessed cell viability using various biocompatibility studies and found that the 3D spheroidal

droplets supported the growth, proliferation, and heterocellular coupling of human

cardiomyocytes and cardiac fibroblasts for long-term in-vitro cultures. The bioprinting protocol

can be adjusted to include a comprehensive range of various in-vivo tissues in addition to its

utilization in tumor models.

Chapter 4: Adoption and Application of the 3D Bioprinted Spheroidal Droplet as a Drug Cytotoxicity Model

The work presented in the following chapter will be submitted for review. This chapter fulfills the requirements for Specific Aim III.

4.1   Abstract

Doxorubicin is an anthracycline chemotherapeutic drug used to treat various malignancies; however, its application is limited because patients can experience severe adverse side effects including irreversible cardiotoxicity [104-106]. Despite substantial scientific research, the mechanism by which doxorubicin causes cardiotoxicity remains incompletely understood. This study examined the effects of DOX-induced cardiotoxicity on human cardiomyocytes using a three-dimensional (3D) bioprinted cardiac spheroidal droplet-based system compared with the traditional two-dimensional cell (2D) culture model to which its cardiotoxic effects were mitigated with the addition of N-acetylcysteine (NAC) and Tiron. Quantification of caspase-3 activity was performed, and the production of reactive oxygen species (ROS) was measured using dihydroethidium (DHE) staining. Different concentrations of DOX ($0.4\mu M$-$1\mu M$) were tested, and results showed that the response of CMs was dose-specific with $1\mu M$ being the concentration in which $0.22\pm0.11\%$ of cells are found to be alive in 3D samples and $1.02\pm 0.28\%$ in 2D cultures after 5 days of culture. Moreover, a flow cytometric analysis was conducted to evaluate CMs proliferation in the presence of DOX and antioxidants. Data from this study supported using the 3D bioprinted cardiac spheroidal droplet as a high throughput model for drug cytotoxicity assays and screening applications.
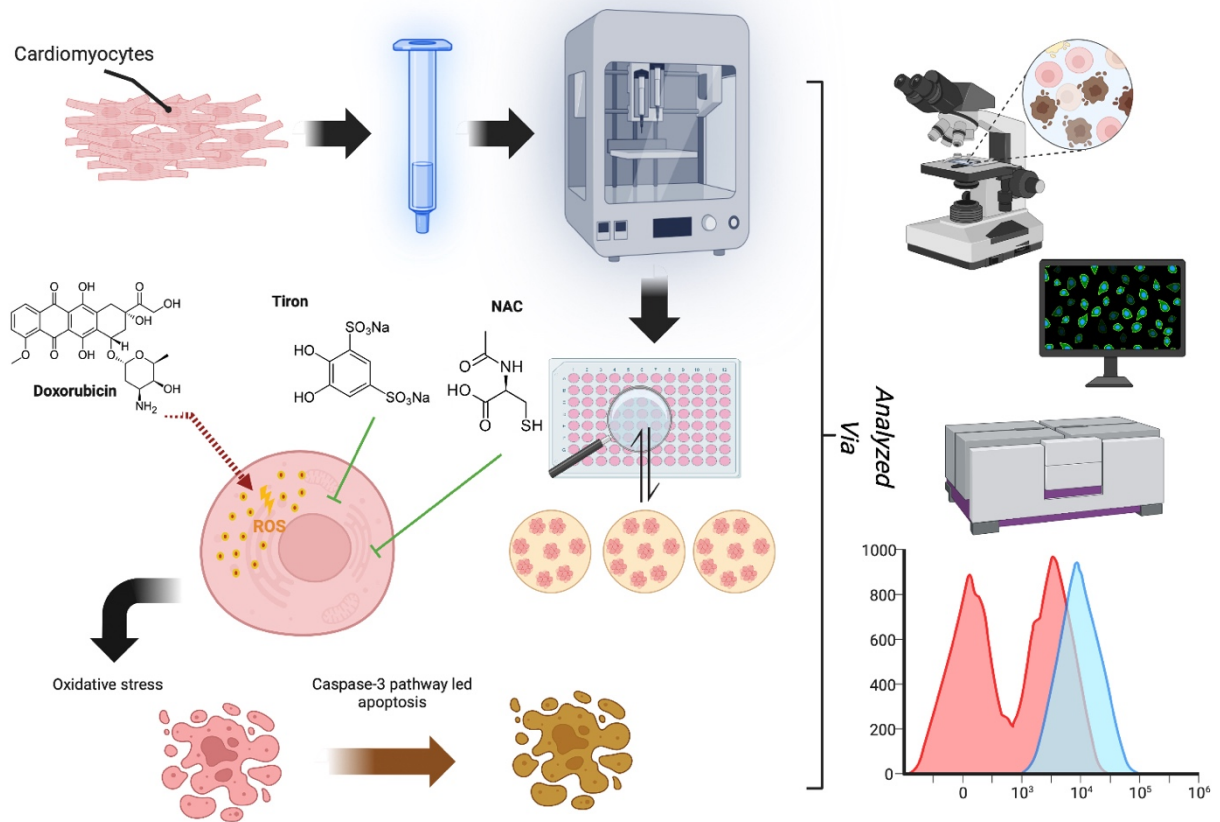
Illustration 4.1: Graphical abstract of the 3D bioprinted cardiac spheroidal droplet model used to test the cytotoxic effects of DOX presented in Chapter 4 of this dissertation.

4.2   Introduction

A significant breakthrough in the recent past was the development of 3D-human-derived models to address challenges specific to understanding human biology and disease [107, 108]. With the emergence of human organoids, which are stem cell-derived 3D cell-culture systems, it is now feasible to simulate the architecture and physiology of human organs. Human organoids provide unique opportunities to study human disease and complement animal models [109]. The use of two-dimensional cell cultures in biomedical research has been successful in many areas, such as increasing our understanding of cellular signaling pathways, determining potential drug targets, and guiding the design of candidate drugs for various pathologies and infectious diseases [108]. In this study, we utilized a 3D cardiac spheroidal droplet model to test the toxic effects of doxorubicin on CMs [45, 109]. One of the most technological developments of the last decades is 3D bioprinting which incorporates diverse fields and principles in material science, cell biology, and tissue engineering. To mimic in-vivo conditions, 3D bioprinting must be capable of recapitulating the complex structure of the extracellular matrix (ECM) by properly integrating biological material, cells, and biomolecules such as growth factors. Researchers have studied tissue engineering to fabricate 3D cardiac constructs in-vitro, in which biomaterials such as alginate, gelatin, collagen, fibrinogen, and hyaluronic acid are generally used. CMs seeded in such a hydrogel scaffold retain heart-specific functions because the scaffold-based systems can provide a 3D culture environment for cells [46, 48, 67, 77-80, 101, 107]. In a recently published work, a droplet-based extrusion printing approach was used to fabricate 3D bioprinted cardiac spheroids using a CELLINK-BIO X printer [45]. This initial study led to the fabrication of a high-throughput cardiac tissue model that can potentially be utilized for studying drug interactions on cardiac cells [45]. For this study, we hypothesized that by using such a 3D

bioprinted cardiac spheroidal model, we would be able to build an alternative 3D model for drug toxicity testing. Cardiomyocytes were 3D bioprinted in a high throughput fashion inside of wells in a 96-round bottom well plate. Confirmation of cardiac toxicity with DOX was quantitatively assessed via a tetrazolium salt assay (MTS) and qualitatively by conducting a Live/Dead assay. We then aimed to mitigate these cytotoxic effects using two antioxidants, N-acetylcysteine (NAC) and Tiron. As cardiomyocytes are the targeted cell type during DOX-induced myocardial toxicity, we quantitatively assessed the proliferation trends of CMs using a flow cytometer, analyzed the activation of the caspase-3 pathway, and the release of ROS.

4.3 Mechanism of DOX-induced Cardiotoxicity

Doxorubicin is a chemotherapeutic drug used to treat numerous diseases. However, patients experience its cardiotoxic effects limiting its use as an effective drug. Despite extensive research, the mechanisms by which doxorubicin kills cardiomyocytes have been elusive, and the exact mechanisms remain unknown [110, 111].

Doxorubicin-induced regulated cardiomyocyte death pathways include autophagy [104], ferroptosis [112], necroptosis [104, 113], pyroptosis [114], and apoptosis [104, 115]. Autophagy is a homeostatic dynamic process by which cellular components, including organelles, are sequestered into membrane vesicles called autophagosomes which fuse with lysosomes for degradation under normal and stress conditions [104]. Such conditions are caused by doxorubicin, and autophagy may be activated during doxorubicin treatment. While doxorubicin can stimulate autophagy, the deregulation of autophagy leads to uncontrolled cardiomyocyte death [115]. Studies have shown that doxorubicin originally induces autophagy but then blocks it, resulting in the buildup of undegraded autophagosomes. Therefore, the suppression of lysosomal proteolysis results in an accumulation of undegraded vesicles, which leads to

increased ROS production and CMs death [104, 115, 116]. Another pathway that causes DOX-induced cardiotoxic effects is known as Ferroptosis [112]. It is characterized by the buildup of iron lipid peroxides, a significant source of ROS. In addition, DOX treatment increases the iron pool, especially in the mitochondria, which can be detrimental to cells. Doxorubicin also triggers another form of cell death known as necroptosis [104, 113]. While apoptosis and autophagy are considered "programmed cell death," necrosis is regarded as "unprogrammed" due to deregulated activity involving the secretion of death-signaling cytokines. Pyroptosis is an inflammatory cell death and is widely recognized in the pathogenesis of cardiovascular diseases [114]. It is accompanied by activating inflammasomes and caspase pathways, mainly caspase 3. The apoptotic pathway is the most studied programmed cell death pathway in DOX-induced cardiotoxicity. DOX treatment causes excess oxidative stress and mitochondrial damage triggering cell death pathways through the activation of caspase 9, which cleaves and activates caspase 3. DOX also activates apoptosis by other mechanisms, including upregulation of p53 resulting in extrinsic and intrinsic apoptosis [104, 115].

Doxorubicin has been well-characterized in lowering cell viability, possibly the most significant aspect of cardiotoxicity. The dose-dependent cardiotoxic effects of doxorubicin are well documented and revealed even at low cumulative doses [110, 111]. Patients prescribed DOX are at potential risk of its asymptomatic cardiotoxic side effects, such as elevated stress in the left ventricular wall leading to arrhythmias, heart failure to heart transplantation [115, 116]. The principal proposed mechanism of doxorubicin-induced cardiotoxicity is increased oxidative stress. The generation of ROS is the general route by which doxorubicin harms the myocardium. Furthermore, oxidative stress is associated with cardiomyocyte death, contributing to the doxorubicin-induced cardiotoxicity [117, 118]. Doxorubicin appears to cause damage to the

mitochondria generating ROS and increasing superoxide formation by increasing endothelial

nitric oxide synthase promoting intracellular hydroxide formation [119, 120]. Many studies have

found various reasons behind DOX's cardiotoxicity, with a common factor whereby induces

oxidative stress resulting in excessive ROS generation [121]. Moreover, ROS production or

oxidative stress promotes apoptosis and necrosis in cardiomyocytes developing severe

cardiomyopathy [122, 123]. Oxidative stress from exposure to hydrogen peroxide (H_2O_2) and

reactive oxygen species causes apoptosis in several cells and organ tissues, including

cardiomyocytes [124]. Cardiomyocytes exposed to DOX undergo apoptosis, and this effect is

primarily attributed to the formation of oxygen free radicals and its intercalation into DNA and

disruption of topoisomerase-II-mediated DNA repair. Therefore, a treatment with various

antioxidants has been proposed to mitigate cardiotoxicity caused by doxorubicin. NAC and Tiron

have been identified as possible antioxidants effective at impeding apoptosis triggered by

reactive oxygen species [125]. While the ROS-scavenging role of NAC is evident, the process

for their regulation of apoptosis is still ambiguous [126]. The inhibition of apoptosis by

antioxidants such as N-acetylcysteine or Vitamin E can further mitigate the outcomes of

oxidative stress in the DOX-induced apoptosis [127, 128]. While cardiomyocytes are the target

cell type of DOX-induced cardiotoxicity, we were particularly interested in assessing the

activation of initiator caspases such as caspase-3 activity and the release of free radicals, which

can cause oxidative damage to myocytes and lead to apoptosis and cell death [118, 122]. With

maximum activity shown in the group with added doxorubicin, a lower activity was

demonstrated in groups with NAC. In the present study, treatment of AC16 cardiomyocytes with

antioxidants such as NAC and Tiron alleviated the DOX-induced oxidative stress in the 3D

bioprinted spheroidal droplets and 2D samples by inhibiting the apoptotic pathway and

decreasing the number of apoptotic cells.

4.4: Materials and Methods

4.4.1: Reagents and Chemicals

Gelatin type A (MP Biomedicals LLC, USA, Cat. No. 901771) and Medium Viscosity Alginic acid (MP Biomedicals LLC, USA, Cat. No. 154724) were used to fabricate the hydrogel scaffolds used in this study. Calcium chloride crosslinking solution was produced from calcium chloride dihydrate (Fisher Chemical, Germany, Cas. No. 10035-04-8) and Phosphate-Buffered Saline (PBS) 10x solution (Thermo Fisher Scientific, USA, Cat. No. 70011069). AC16 human cardio-myocytes or (ATCC, Manassas, VA) were cultured and expanded in Dulbecco's modified Eagle medium (Sigma, Germany, Cat. No. D6434) containing 2 mM L-glutamine (EMD Millipore, Germany, Cat. No. TMS- 002-C), 12.5% FBS (EMD Millipore, Germany, Cat. No. ES-009-B) and 1X penicillin-streptomycin solution (EMD Millipore, Germany, Cat. No. TMS-AB2-C), 0.25% Trypsin-EDTA (Thermo Fisher Scientific, USA Cat. No. 25200056). 96 round-bottom well plates (Thermo Fisher Scientific, USA, Cat. No. 12-565-212) were used for bioprinting and cell culture. Doxorubicin hydrochloride powder (Sigma, Germany, CAS-No: 25316-40-9) was used as a cardiotoxic agent. N-Acetyl-cysteine (Sigma, Germany, CAS-No: 616-91) was obtained from Sigma-Aldrich and Tiron (Thermo Fisher Scientific, USA, Cat. No.)174140250 as a ROS scavenging agents. CellTiter 96® AQueous One Solution Cell Proliferation Assay (Promega, USA, Cat. No. G3582) was used to determine cell viability quantification. Hanks' Balanced Salt Solution (HBSS) (Thermo Fisher Scientific, USA, Cat. No. 88284) was used to wash cells. The LIVE/DEAD® Viability/Cytotoxicity Kit (Thermo Fisher, USA, Cat. No. L3224) was used to image viable and dead cells. The caspase-3 Colorimetric

Assay Kit (NucView® 488 Caspase-3 Assay Kit for Live Cells, USA, Cat. No. 30029-T) was purchased from Biotium (USA) to detect cellular apoptosis. CellTrace Violet, proliferation kit (Invitrogen, USA, Cat. No. C34557) as a cell proliferation dye tracker, and Dihydroethidium (DHE) was used as a superoxide indicator (Thermo Fisher Scientific, USA, Cat. No. D11347).

4.4.2 DOX and Tiron/NAC Solution Preparation

10g of DOX was dissolved in 1.72mL of DMSO to reconstitute a stock solution of 10mM according to the manufacturer's protocol [129, 130]. To induce cardiotoxicity in the 3D spheroidal droplets with cardiomyocytes, four different stock concentrations of DOX (40μM, 60μM, 80μM, and 100μM) were prepared and 2μL of each stock solution was added to 200μL of culture media. It has been shown that DOX induces the production of reactive oxygen species and antioxidants, such as NAC and Tiron can mitigate the cytotoxic effects [131, 132]. From a 200mM Tiron/NAC stock solution, 1μL and 3μL were added to 200μL culture media to prepare a solution of 1mM and 3mM respectively. Similarly, from a 500mM Tiron/NAC stock solution, 2μL and 3.2μL were added to 200μL culture media to form a solution of 5mM and 8mM respectively and from a 613mM stock solution, 3.3μL and 4.9μL were added to form a solution of 10mM and 15mM respectively. MTS measurements were recorded using a microplate reader (BioTek Synergy H1, CA, USA) on days 1, 3, and 5. To ensure their homogeneous diffusion into the 3D bioprinted scaffolds and 2D samples, the antioxidants were added 24h prior to the addition of DOX [133-135]. MTS measurements were recorded on a microplate reader (BioTek Synergy H1, CA, USA) on days 1, 3, and 5. The blank samples included the hydrogel scaffolds with DOX subtracted from the MTS reading. For comparison, both positive (in the presence of DOX) and negative (in the absence of DOX) 2D control samples were included.

4.4.3 Cell Culture

AC16 human cardiomyocytes (passages 3-4) were cultured in Dulbecco's modified Eagle's complete growth medium supplemented with 10% fetal bovine serum (FBS) and 1% penicillin-streptomycin. Before 3D bioprinting, cells were harvested by trypsinization and mixed with the alginate-gelatin hydrogel to constitute a final cell seeding density of 1×10^6 cells per 1 mL of bioink (approximately 50 spheroidal droplets/1mL bioink; 20,000 cells per spheroidal droplet). Cultures were incubated with a complete growth medium and maintained in a humidified atmosphere of 95% air and 5% CO_2 at 37°C. The initial cell seeding density used in this study was 20,000 cells per 2D cultured well and 20,000 per spheroidal droplet [45].

4.4.4 Bioink Preparation

An optimized protocol for bioink preparation was based on an alginate/gelatin scaffold that was developed and reported in a previous study [45]. Briefly, under aseptic conditions, 2% w/v gelatin and 3% w/v alginate were dissolved in Milli-Q water respectively under constant stirring [45, 46, 86]. The mixture was next allowed to rest and dissolve for 16-24 h at room temperature and centrifuged at 1200 rpm for 5 min to remove the remaining air bubbles. Before cell printing, gels were additionally UV sterilized for 15 min, after which they were loaded into a 3 mL syringe (CELLINK, Blacksburg, VA, USA).

4.4.5 Biofabrication of 3D Constructs and Culture

A 3D spheroid with a diameter of 2 mm was designed using SolidWorks® software. Using CELLINK BIO X (Blacksburg, VA, USA), the temperature-controlled printer head was used to place the droplets inside a 96-round-bottom well plate. Printing parameters are shown in **Table 3.1**. 5 µL of 80 mM $CaCl_2$ sterile solution was added to the bottoms of each of the wells.

The resultant spheroidal droplets were further crosslinked with an additional 75 µL of $CaCl_2$ post-printing while being placed on a Belly Dancer Shaker (IBI SCIENTIFIC, Iowa, USA) for 15 mins at a speed of 4.5 (au).

4.4.6 MTS Standard Curve for Cardiomyocytes

Cardiomyocyte viability was determined using CellTiter 96 Aqueous One Solution Cell Proliferation Assay kit from Promega (Madison, WI). The culture medium was removed, and a tetrazolium salt (MTS) was prepared and added in the ratio of 1:10 (MTS solution: media) where the samples were left in the incubator (5% CO_2 and 37°C) for 4 hours according to the manufacturer's protocol [46, 136, 137]. Absorbance was recorded on a microplate reader (BioTek Synergy H1, CA, USA) at 490nm. Using the calibration curve, the number of live cells was determined, and the percentage of surviving cells was compared with that of the control sample from the equations shown below:

The linear best-fit equation for 3D spheroidal droplets used was:

$$y = 3.1 \times 10^{-5}x + 0.035 \quad (1)$$

The linear best-fit equation for 2D samples used was:

$$y = 3.6 \times 10^{-5}x + 0.074 \quad (2)$$

$$Percent\ Cell\ Viability\ (\%) = \frac{\#\ of\ LIVE\ cells}{Total\ \#\ of\ cells\ in\ control\ group} \ X\ 100 \quad (3)$$

To plot a standard curve, varying concentrations of CMs were used to determine the MTS value for each concentration and construct a best fit calibration curve for both 3D bioprinted

spheroidal cell droplets and 2D cell culture samples. This calibration curve enabled us to quantify the number of live cells through its corresponding linear equation derived by MATLAB by entering the variable "y" as the OD value and calculating "x" as the number of viable cells for both 3D and 2D samples using the above two formulas (equations 1 and 2) [137, 138] and percent cell viability (% CV) was inferred using equation 3.

4.4.7   Live/Dead assay

Live/Dead cytotoxicity assay assessed cell survival following the manufacturer's protocol. NAC and Tiron were added to the 3D and 2D samples 24h prior to the addition of DOX. Based on the intracellular esterase activity and plasma membrane integrity, calcein AM was used to stain live cells in green exclusively. In contrast, ethidium homodimer dye was used to stain only compromised plasma membranes of dead cells by binding to nucleic acids exhibiting a red fluorescence dye. Images were acquired with an inverted Zeiss microscope (Zeiss, AXIO, Germany) using 43 DsRed (ex533-558nm/em570-640nm) to perceive dead cells and 38 Green Fluorescent Prot (ex450-490nm/em500-550nm) to perceive live cells. Percent viability was quantified using the formula below:

$$No. of\ live\ or\ dead\ cells\ (\%) = \frac{\#\ of\ green\ or\ red\ cells}{Total\ \#\ of\ green\ and\ red\ cells}\ X\ 100 \quad (4)$$

4.4.8   In vitro Caspase-3 Activity Assay

Activation of the caspase-3 (Cas-3) pathway is considered a pivotal event during apoptosis; therefore, Cas-3 activity was determined using NucView® 488 Cas-3 substrate; a permeable fluorogenic caspase substrate for identifying Cas-3 activity within live cells [139, 140]. The substrate comprises a fluorogenic DNA dye coupled with a DEVD (Asp-Glu-Val-Asp)

substrate element specific for caspase-3 and prepared according to the manufacturer's protocol. The DEVD/Cas-3 recognition subunit is non-fluorescent until cleaved. During apoptosis, the substrate enters the cytoplasm by crossing the cell membrane, where it is cleaved by Cas-3. The dye, NucView®488, enters the cell nucleus where it binds DNA and fluoresces green at 488 nm, expressing apoptosis. 15mM of Tiron/NAC was added to the 3D and 2D samples 24h prior to the addition of DOX, and cas-3 activity was quantified using a microplate reader (BioTek Synergy H1, CA, USA) on days 1 and 3 and high magnification images were acquired using a LSM 700 confocal microscope (ZEISS LSM, Germany).

4.4.9 Dihydroethidium (DHE) Staining

To determine the level of ROS production in doxorubicin-induced AC16 CMs, intracellular oxidant production levels in CMs were measured using DHE fluorescence following the manufacturer's protocol. NAC and Tiron were added to the 3D and 2D samples 24h prior to the addition of DOX, and at each time point samples were washed with HBSS (Hanks' Balanced Salt Solution) and incubated with DHE for 30min at 37°C. The cells were washed 3 times, and mean fluorescent intensity readings were taken using a microplate reader (BioTek Synergy H1, CA, USA) on days 1 and 3. Images were taken using an inverted Zeiss microscope (Zeiss, AXIO, Germany) using 43 DsRed (em533-558nm/ex570-640nm) to perceive ROS and 49 DAPI (ex335-383nm/em420-470nm) as an overall nuclear stain.

4.4.10 Assessment of Cell Viability with DOX and NAC using Flow Cytometry

Flow cytometric analysis was performed using Beckman Coulter Gallios Flow Cytometer (Beckman Coulter, CA, USA). CMs were prestained using CellTraceTMViolet (CTV) proliferation kit (Invitrogen, CA, USA) according to the manufacturer's protocol and were

treated with their respective doses of NAC and DOX. On day 1 and day 3, the 3D spheroidal droplets with cells were cut using a blade, and cells were extracted using Miltenyi gentleMACS Dissociator (Miltenyi Biotec, MA, USA) using a Multitissue Dissociation Kit-1 by running the Multi_B program according to the manufacturer's protocol. For 2D samples, cells were detached using trypsin-EDTA. Cells were fixed with 4% paraformaldehyde (PFA) for 15 min at room temperature, then added to their assigned FACS analysis falcon tubes, and analyzed using excitation and emission wavelengths of 405 and 450nm, respectively. Negative controls included freshly isolated non-stained cells and positive controls were prestained with CTV [45, 46, 141].

4.4.11 Quantitative Reverse Transcriptase Chain Reaction (qPCR) Analysis

To compare the gene expression and integrity between the CMs present in the 3D bioprinted spheroidal hydrogels to CMs cultured on 2D surfaces, qPCR was performed. After 5 days of culture, scaffolds were washed using 1X PBS, and cells were extracted following the previously published method [54]. The dissolved mixture was then centrifuged at 400g for 10 min yielding the cell pellet.

Total RNA extraction was carried out using RNeasy® Plus Mini Kit (QIGEN, Germany) according to the manufacturer's instructions. Extracted RNAs were quantified by NanoDrop OneC spectrophotometer (ThermoFisher Scientific, MA, USA), and the absorbance ratios at 260/280 nm and 260/230 nm were measured to control RNA purity as shown in Supporting Table S2. Total RNA (50 ng) was reverse transcribed to cDNA using the First Strand cDNA Synthesis Kit (OriGene Technologies Inc, MD, USA) in a volume of 20 µL, according to the manufacturer's instructions. Extracted cDNA was quantified by NanoDrop OneC spectrophotometer (ThermoFisher Scientific, MA, USA), and the absorbance ratios at 260/280

nm and 260/230 nm were measured.

The RT–qPCR reactions were performed in Quantstudio 3 (ThermoFisher Scientific, MA, USA). The cardiomyocytes isolated from 2D and 3D samples (n=3 each) were placed in qPCR Tubes, with optical strip caps 3 (ThermoFisher Scientific, MA, USA) in a reaction volume of 20 μL. To avoid sample contamination and primer-dimer formation that could produce false positive results, no template control was used. The genes analyzed were selected from the vendor. The gene expression GJA1 (Connexin 43) was studied as the target gene and GAPDH was used as the reference gene (control). The reaction started with a 10 min initial denaturation step at 95°C, 40 cycles of 95°C for 15s and 60°C for 15s according to the protocol provided by Origene. The quantification cycle (CT) values were automatically calculated by the qPCR instrument software Quantstudio 3 (ThermoFisher Scientific, MA, USA). A statistical algorithm was used to evaluate gene expression of the comparative CT method (2-ΔΔCT) [142]. Average CTs of GAPDH was used as endogenous control and the stability of the target genes was expressed as Ct values of each candidate gene normalized with GAPDH.

4.5   Results and Discussion

4.5.1   DOX Affects the Viability and Proliferation of CMs in a Dose-responsive Manner

Four different concentrations of DOX (0.4μM, 0.6μM, 0.8μM, and 1μM) were used to study the cardiotoxic effects on CMs using the 3D bioprinted spheroidal model, and the results were compared with 2D models. In Figure 4.1 (for 3D results) and Figure 4.2 (for 2D results), MTS assay data revealed that the trends of OD values progressively reduced with respect to the control group (no DOX). For the 3D bioprinted spheroidal droplets, the OD value decreased from 0.90 ± 0.02 on day 1 to 0.52 ± 0.04 on day 5 ($p<0.05$) when 0.4μM of DOX was added, from 0.85 ± 0.05 on day 1 to 0.43 ± 0.03 on day 5 when 0.6μM of DOX was added ($p<0.05$) and from

0.77±0.06 at day 1 to 0.12±0.02 on day 5 when 0.8μM of DOX was added (p<0.05). With 1μM

of DOX, the OD value decreased from 0.71±0.03 on day 1 to 0.002±0.001 on day 5 (p<0.05) but

in the samples where DOX was not added, no statistical significance was observed between day

1 (0.93±0.03) and day 5 (0.90±0.04) with p>0.05. Since the value of OD value is a measure of

metabolic activity, it indicates the amount of live cells per sample. Thus a lower OD value

reflects a lower number of viable cells present in a sample and vice-versa. Results showed as the

concentration of DOX was increased, the OD value was decreased correlating with a lesser

number of viable cells confirming the cardiotoxic effects caused by DOX on CMs.
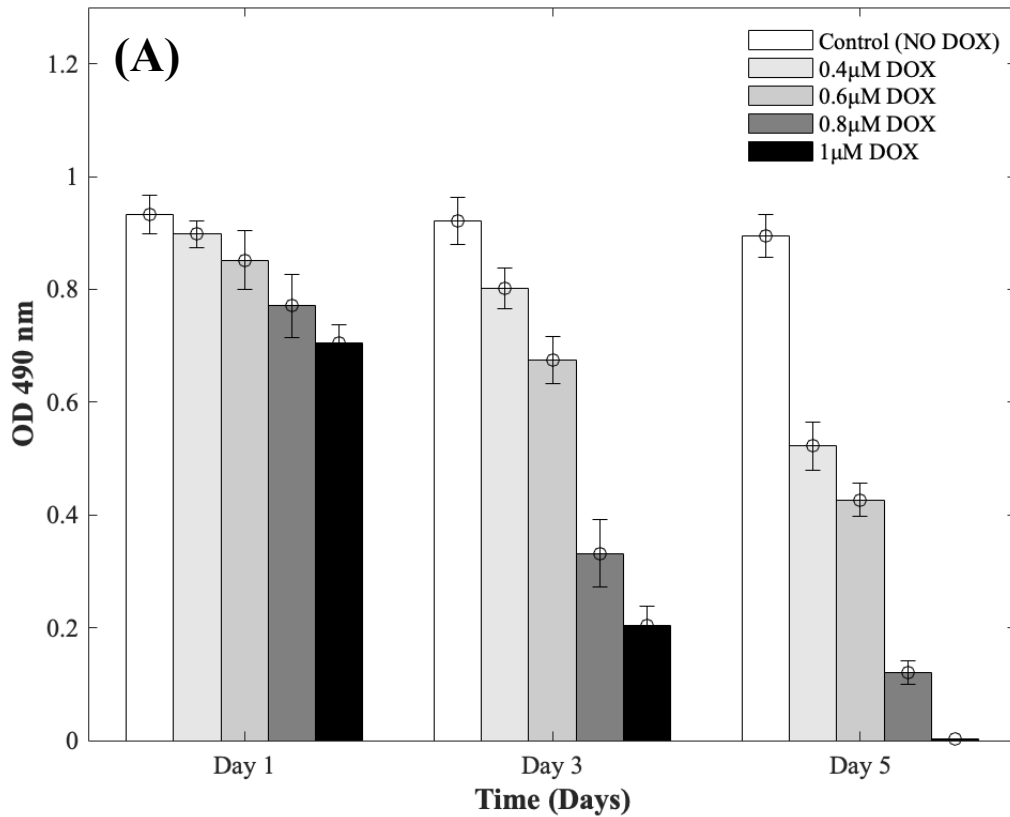
(B)	Day 1		Day 3		Day 5	
	OD Value	% Cell Viability (% CV)	OD Value	% Cell Viability (% CV)	OD Value	% Cell Viability (% CV)
0.4µM DOX	0.90 ± 0.02	$97 \pm 2\%$	0.80 ± 0.04	$86 \pm 4\%$	0.52 ± 0.04	$56 \pm 4\%$
0.6µM DOX	0.85 ± 0.05	$91 \pm 5\%$	0.67 ± 0.04	$72 \pm 4\%$	0.43 ± 0.03	$46 \pm 3\%$
0.8µM DOX	0.77 ± 0.06	$82 \pm 6\%$	0.33 ± 0.06	$33 \pm 6\%$	0.12 ± 0.02	$10 \pm 2\%$
1µM DOX	0.71 ± 0.03	$75 \pm 3\%$	0.20 ± 0.03	$19 \pm 3\%$	0.002 ± 0.001	$0.22 \pm 0.11\%$
Control (NO DOX)	0.93 ± 0.03	100%	0.92 ± 0.04	100%	0.90 ± 0.04	100%

Figure 4.1: Dose responsive effects of DOX on CMs using 3D bioprinted spheroidal droplets. **(**A) Optical density measurements for MTS assay of CMs treated with increasing concentrations of DOX during 5 days of culture. (B) Table showing the percent cell viability of CMs treated with increasing concentrations of doxorubicin extrapolated from the linear best fit curve of MTS data (Appendix A.2.1) over 5 days. The actual cell numbers used to generate % CV are shown in Appendix A.2.1.

For the 2D CMs models, the OD value decreased from 1.02 ± 0.04 on day 1 to 0.72 ± 0.04 on day 5 ($p < 0.05$) when 0.4µM of DOX was added, from 1 ± 0.05 on day 1 to 0.56 ± 0.04 on day 5 when 0.6µM of DOX was added ($p < 0.05$) and from 0.90 ± 0.06 at day 1 to 0.22 ± 0.02 on day 5 when 0.8µM of DOX was added ($p < 0.05$). With 1µM of DOX, the OD value decreased from 0.81 ± 0.05 on day 1 to 0.011 ± 0.003 on day 5 ($p < 0.05$) but in the samples where DOX was not added, no statistical significance was observed between day 1 (1.08 ± 0.05) and day 5 (1.08 ± 0.05) with $p > 0.05$. These trends compared well with results from 3D samples.

To calculate the % cell viability (% CV) (equation 1) of CMs in each sample, the linear best-fit equations (equations 2 and 3) from the MTS standardization assay were used. For the 3D bioprinted spheroidal droplets (Figure 4.1 B), the % CV) decreased from $97 \pm 2\%$ on day 1 to $56 \pm 4\%$ on day 5 ($p < 0.05$) when 0.4µM DOX was added, from $91 \pm 5\%$ on day 1 to $46 \pm 3\%$ at day 5 ($p < 0.05$) when 0.6µM DOX was added, from $82 \pm 6\%$ at day 1 to $10 \pm 2\%$ at day 5 ($p < 0.05$) when 0.8µM DOX was added and from $75 \pm 3\%$ at day 1 to $0.22 \pm 0.11\%$ at day 5 ($p < 0.05$) when

1μM of DOX was added. These values confirmed the existing trends in OD values from MTS assay reported earlier.

For the 2D models (Figure 4.2 B), % CV of CMs decreased from 94±4% on day 1 to 64±4% on day 5 ($p<0.05$) when 0.4μM DOX was added, from 92±5% on day 1 to 48±3% on day 5 ($p<0.05$) when 0.6μM DOX added, from 82±6% at day 1 to 15±1% at day 5 ($p<0.05$) when 0.8μM of DOX was added and from 73±5% at day 1 to 1.02±0.28% at day 5 ($p<0.05$) when 1μM DOX was added. The actual number of live CMs is derived from the best fit curve using their corresponding OD values found in Appendix A.2.1 (corresponding to 3D samples) and Appendix A.2.2 (corresponding to 2D samples). Images showing the diffusion of DOX into the hydrogel scaffolds can be found in Appendix A.2.13.
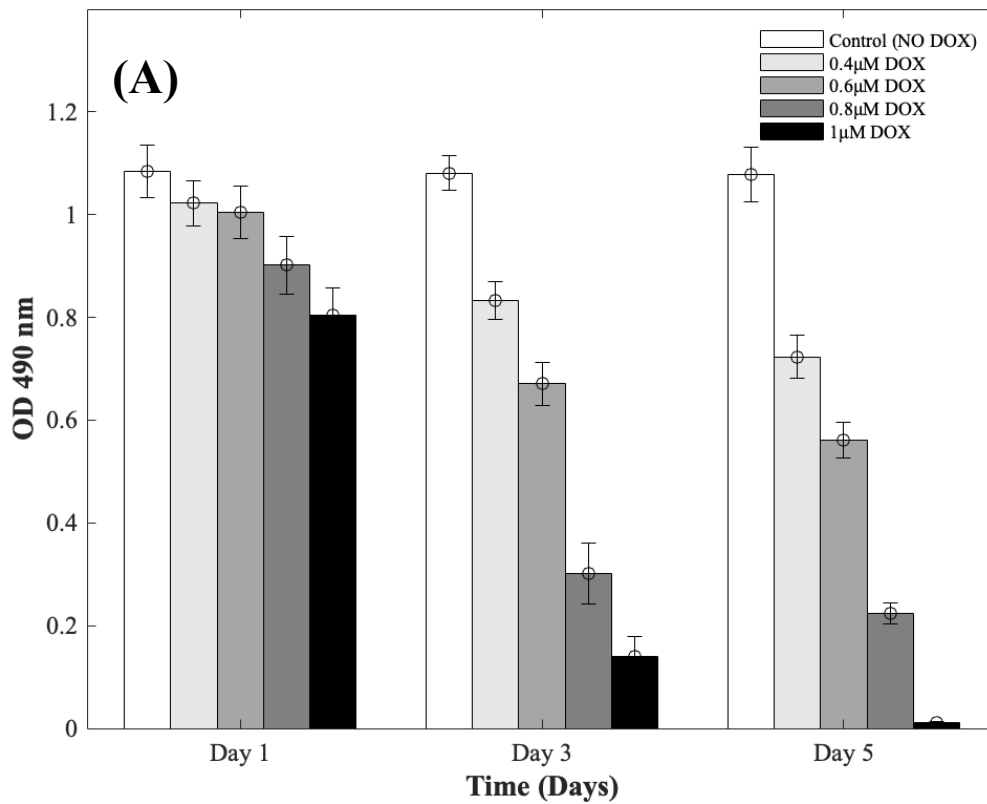
(B)	Day 1		Day 3		Day 5	
	OD Value	% Cell Viability (% CV)	OD Value	% Cell Viability (% CV)	OD Value	% Cell Viability (% CV)
0.4µM DOX	1.02 ± 0.04	94 ± 4%	0.83 ± 0.04	75 ± 4%	0.72 ± 0.04	64 ± 4%
0.6µM DOX	1.00 ± 0.05	92 ± 5%	0.67 ± 0.04	59 ± 4%	0.56 ± 0.04	48 ± 3%
0.8µM DOX	0.90 ± 0.06	82 ± 6%	0.30 ± 0.06	22 ± 4%	0.22 ± 0.02	15 ± 1%
1µM DOX	0.81 ± 0.05	73 ± 5%	0.14 ± 0.04	7 ± 2%	0.011 ± 0.003	1.02 ± 0.28%
Control (NO DOX)	1.08 ± 0.05	100%	1.08 ± 0.03	100%	1.08 ± 0.05	100%

Figure 4.2: Dose responsive effects of DOX of CMs on 2D samples. **(**A) Optical density measurements for MTS assay of CMs treated with increasing concentrations of DOX during 5 days of culture. (B) Table showing the percent cell viability of CMs treated with increasing concentrations of doxorubicin extrapolated from the linear best fit curve of MTS data (Appendix A.2.2) over 5 days. The actual cell numbers used to generate % CV are shown in Appendix A.2.2.

The effect of DOX on CMs was seemingly more pronounced in 3D scaffolds as confirmed by our results. This can be attributed to the intensified distribution of DOX inside the hydrogel's mesh network and its anchorage to the polymer's backbone that constitutes the bioink [53, 143] in contrast to 2D cell cultures models whose molecules diffuse throughout the cell culture media [144].

4.5.2 Reversal of DOX-induced Cardiotoxicity on CMs with the Addition of NAC and Tiron

DOX induces myocardial damage to the heart via the elevation of ROS [117, 118, 145]. In an attempt to mitigate the cytotoxic effects caused by doxorubicin on CMs in the 3D spheroidal droplet model, six different concentrations of NAC and Tiron were initially tested. Preliminary MTS assay data for 3mM, 5mM, and 10mM of antioxidants can be found in Appendix A.2.5, A.2.6, A.2.8, A.2.9. Quantitative analysis using a colorimetric assay with increasing concentrations of Tiron and NAC (Figure 4.3) in the presence of 1µM DOX is

depicted during 5 days of culture. For the 3D bioprinted spheroidal droplets, OD values decreased from 0.77 ± 0.06 to 0.24 ± 0.03 ($p<0.05$) and from 0.78 ± 0.06 to 0.47 ± 0.02 ($p<0.05$) after 5 days of culture when 1mM and 8mM of Tiron were added respectively. But with the addition of 15mM of Tiron, no statistically significant difference was observed between day 1 (0.91 ± 0.05) and day 5 (0.83 ± 0.05) (Figure 3A) with $p>0.05$. With NAC, the OD value also dropped from 0.74 ± 0.03 to 0.25 ± 0.04 ($p<0.05$) and from 0.77 ± 0.04 to 0.50 ± 0.03 ($p<0.05$) after 5 days of culture when 1mM and 8mM of the antioxidant were added to the 3D spheroidal droplet (Figure 4.3). But with the addition of 15mM of NAC, no statistically significant difference was observed between day 1 (0.90 ± 0.02) and day 5 (0.86 ± 0.02) with $p>0.05$.

To further calculate the number of viable to non-viable CMs present, the linear best-fit equations were used. % CV decreased from $82\pm6\%$ to $24\pm3\%$ ($p<0.05$) and from $83\pm6\%$ to $50\pm2\%$ ($p<0.05$) after 5 days of culture when 1mM and 8mM of Tiron (Figure 4.3A) were added respectively to the 3D spheroidal droplets. But with the addition of 15mM of Tiron, no statistically significant difference was observed in % CV between day 1 ($98\pm5\%$) and day 5 ($92\pm6\%$) (Figure 3B) with $p>0.05$.

With 1mM and 8mM of NAC (Figure 4.3D), the % CV dropped from $78\pm3\%$ to $25\pm4\%$ ($p<0.05$) and from $82\pm4\%$ to $54\pm3\%$ ($p<0.05$) respectively after 5 days of culture. But with the addition of 15mM of NAC (Figure 4.3D), % CV remained relatively stable between day 1 ($97\pm2\%$) and day 5 ($95\pm2\%$) with $p>0.05$.

Tiron
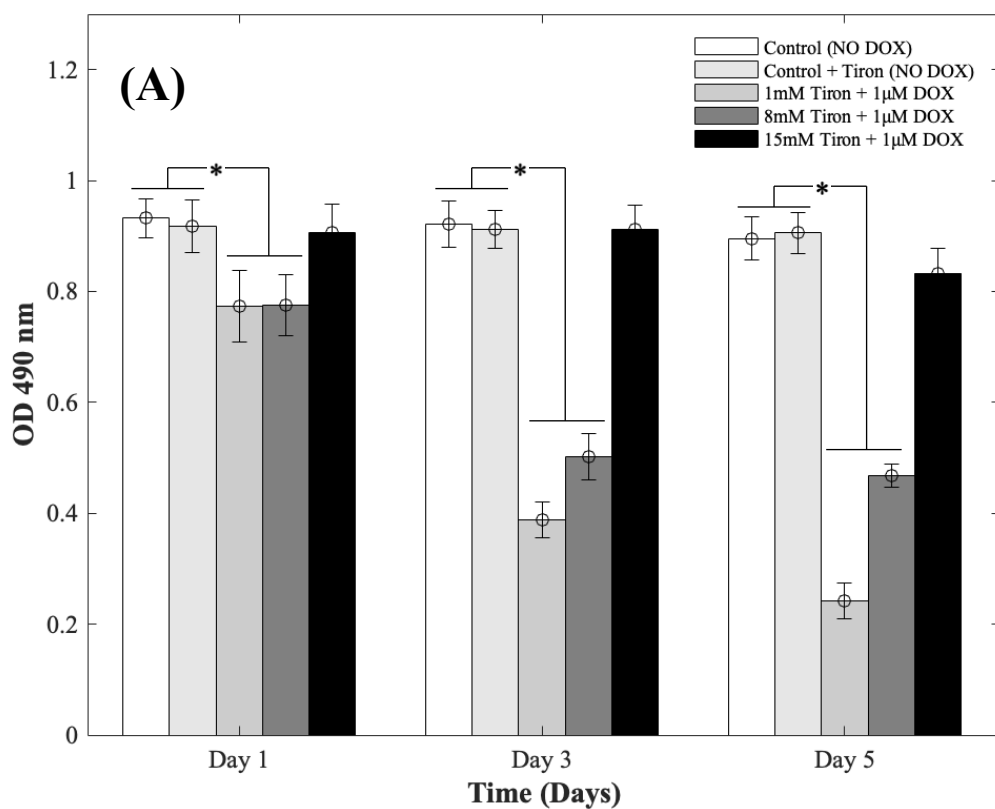
(B)		Day 1		Day 3		Day 5	
		OD Value	% Cell Viability (% CV)	OD Value	% Cell Viability (% CV)	OD Value	% Cell Viability (% CV)
Tiron	1mM	0.77 ± 0.06	82 ± 6%	0.39 ± 0.03	40 ± 3%	0.24 ± 0.03	24 ± 3%
	8mM	0.78 ± 0.06	83 ± 6%	0.50 ± 0.04	53 ± 4%	0.47 ± 0.02	50 ± 2%
	15mM	0.91 ± 0.05	98 ± 5%	0.91 ± 0.04	99 ± 4%	0.83 ± 0.05	92 ± 6%
	Control (NO DOX)	0.93 ± 0.04	100%	0.92 ± 0.04	100%	0.90 ± 0.04	100%
	Control + Tiron (NO DOX)	0.92 ± 0.05	100%	0.91 ± 0.03	100%	0.91 ± 0.04	100%

(C)
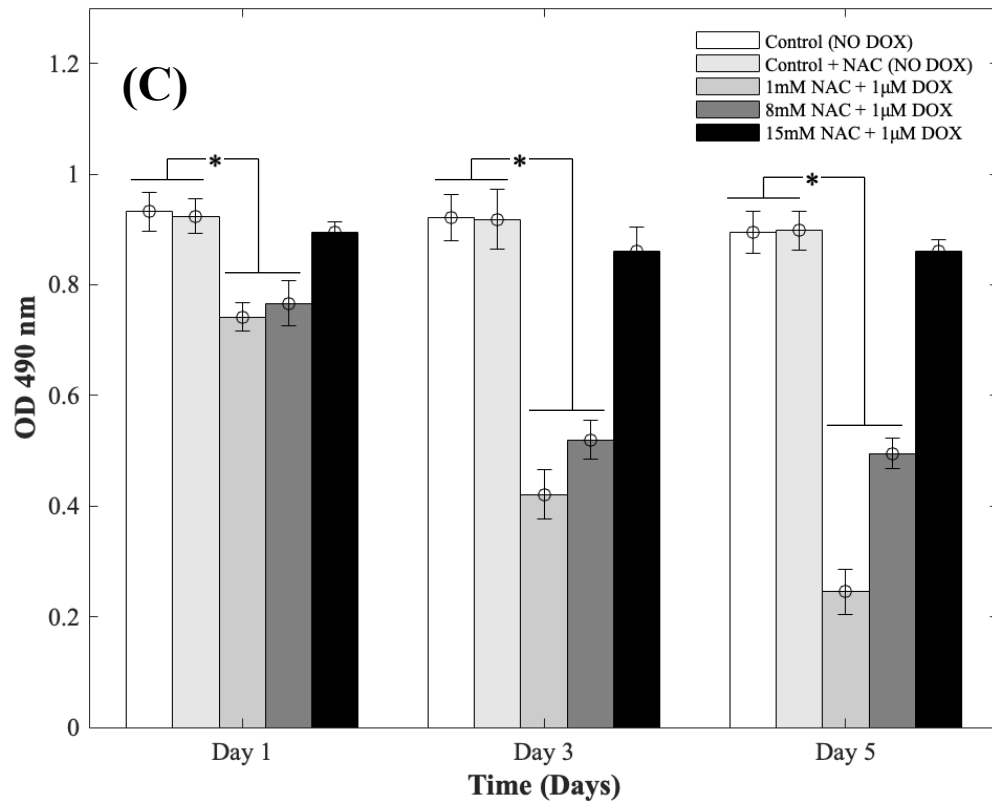
(D)

		Day 1		Day 3		Day 5	
		OD Value	% Cell Viability (% CV)	OD Value	% Cell Viability (% CV)	OD Value	% Cell Viability (% CV)
NAC	1mM	0.74 ± 0.03	$78 \pm 3\%$	0.42 ± 0.04	$44 \pm 4\%$	0.25 ± 0.04	$25 \pm 4\%$
	8mM	0.77 ± 0.04	$82 \pm 4\%$	0.52 ± 0.04	$55 \pm 4\%$	0.50 ± 0.03	$54 \pm 3\%$
	15mM	0.90 ± 0.02	$97 \pm 2\%$	0.86 ± 0.05	$93 \pm 5\%$	0.86 ± 0.02	$95 \pm 2\%$
	Control (NO DOX)	0.93 ± 0.04	100%	0.92 ± 0.04	100%	0.90 ± 0.04	100%
	Control + NAC (NO DOX)	0.92 ± 0.03	100%	0.92 ± 0.05	100%	0.90 ± 0.04	100%

Figure 4.3: Quantitative analysis depicting the effects of supplementing Tiron/NAC on CMs using 3D spheroidal droplets. Optical density measurements for MTS assay of CMs treated with increasing concentrations (1mM, 8mM, and 15mM) of (A) Tiron and (C) NAC with 1μM DOX. (B, D) Tables representing the percent cell viability of CMs extrapolated from the linear best fit curve of MTS data during 5 days of culture. *p values were found to be all statistically different. The actual cell numbers used to generate % CV are shown in Appendix A.3.

A similar trend was observed in CMs cultured in 2D plates with 1mM, 8mM, and 15mM of Tiron (Figure 4.4).

Tiron
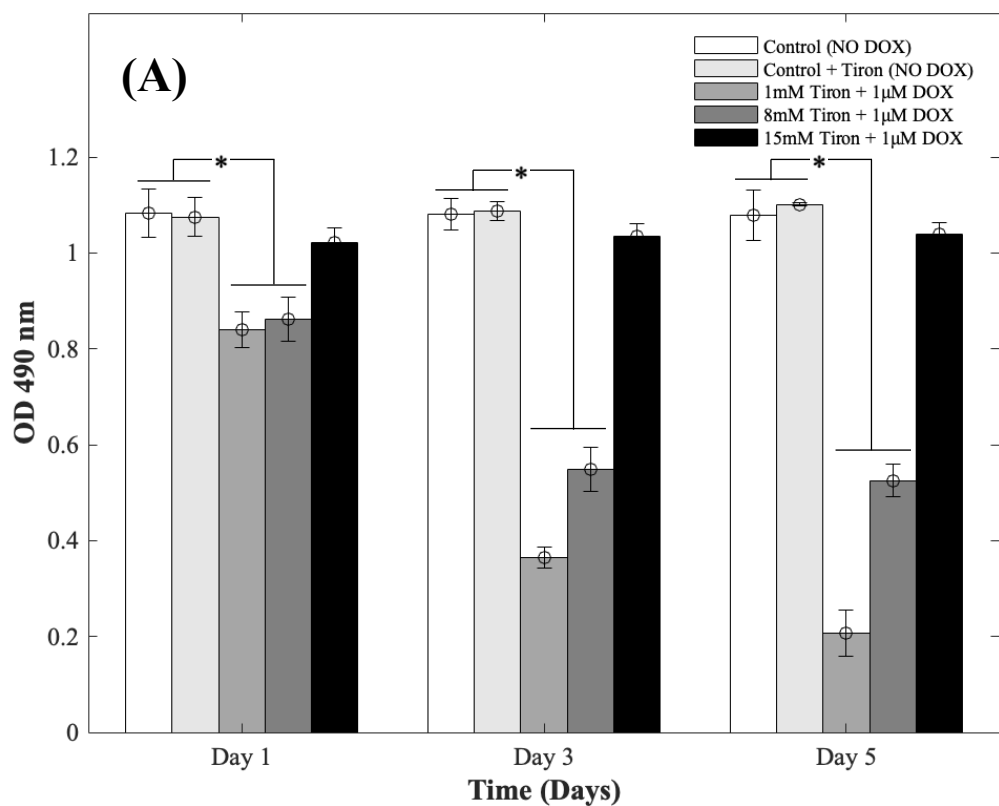
(B)		Day 1		Day 3		Day 5	
		OD Value	**% Cell Viability (% CV)**	**OD Value**	**% Cell Viability (% CV)**	**OD Value**	**% Cell Viability (% CV)**
Tiron	**1mM**	0.84 ± 0.04	76 ± 4%	0.36 ± 0.02	28 ± 2%	0.21 ± 0.05	14 ± 3%
	8mM	0.86 ± 0.05	78 ± 5%	0.55 ± 0.05	47 ± 4%	0.53 ± 0.03	45 ± 3%
	15mM	1.02 ± 0.03	94 ± 3%	1.04 ± 0.03	96 ± 3%	1.04 ± 0.03	96 ± 3%
	Control (NO DOX)	1.08 ± 0.05	100%	1.08 ± 0.03	100%	1.08 ± 0.05	100%
	Control + Tiron (NO DOX)	1.08 ± 0.04	100%	1.09 ± 0.02	100%	1.10 ± 0.003	100%

NAC
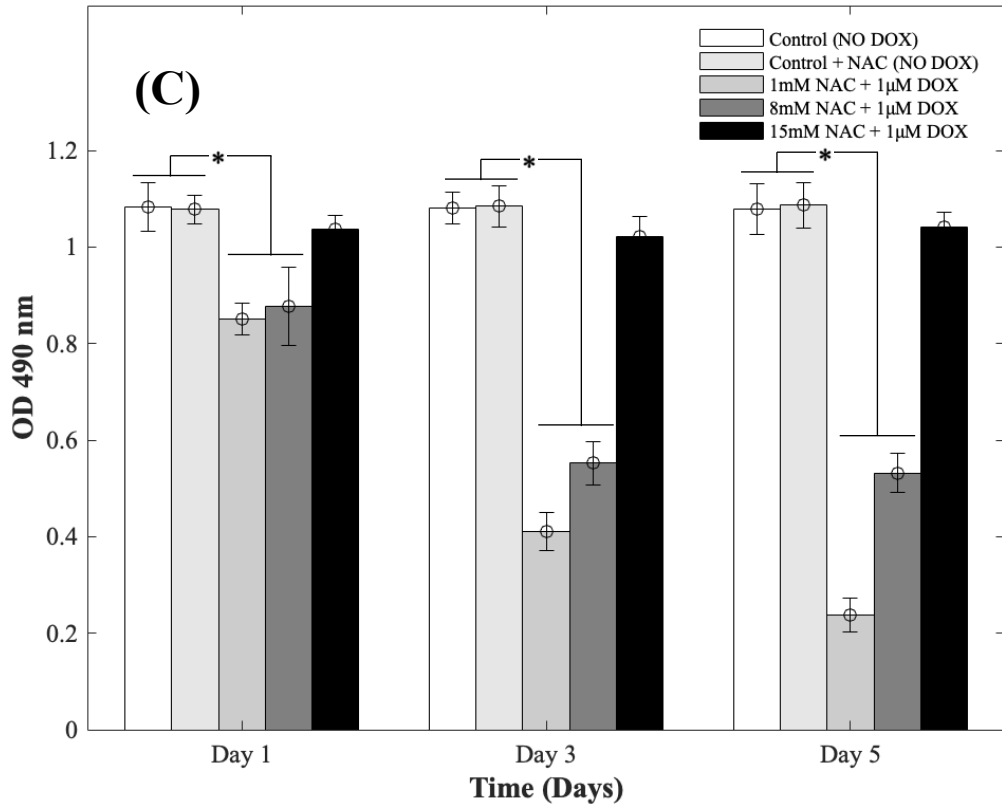
(C)

Legend:
- Control (NO DOX)
- Control + NAC (NO DOX)
- 1mM NAC + 1µM DOX
- 8mM NAC + 1µM DOX
- 15mM NAC + 1µM DOX

Y-axis: OD 490 nm
X-axis: Time (Days) — Day 1, Day 3, Day 5

(D)

NAC		Day 1		Day 3		Day 5	
		OD Value	% Cell Viability (% CV)	OD Value	% Cell Viability (% CV)	OD Value	% Cell Viability (% CV)
	1mM	0.85 ± 0.03	77 ± 3%	0.41 ± 0.04	33 ± 3%	0.24 ± 0.04	17 ± 3%
	8mM	0.88 ± 0.08	80 ± 7%	0.55 ± 0.05	47 ± 4%	0.53 ± 0.04	45 ± 3%
	15mM	1.04 ± 0.03	96 ± 3%	1.02 ± 0.04	94 ± 4%	1.04 ± 0.03	96 ± 3%
	Control (NO DOX)	1.08 ± 0.05	100%	1.08 ± 0.03	100%	1.08 ± 0.05	100%
	Control + NAC (NO DOX)	1.08 ± 0.03	100%	1.08 ± 0.04	100%	1.09 ± 0.05	100%

Figure 4.4: Quantitative analysis depicting the effects of supplementing Tiron/NAC on 2D samples with CMs and 1µM DOX. Optical density measurements for MTS assay with increasing concentrations (1mM, 8mM, and 15mM) of (A) Tiron and (C) NAC respectively with 1µM DOX during 5 days of culture. *p values were found to be all statistically different. (B, D) Tables showing the percent cell viability of CMs extrapolated from the linear best fit curve of MTS data. The actual cell numbers used to generate % CV are shown in Appendix A.2.4.

While OD trends and %CV were comparable between the 3D bioprinted spheroidal droplet scaffolds and CMs cultured in 2D cell cultures, 3D scaffolds potentially serve as a desirable microenvironment for CMs providing mechanical support and necessary biochemical cues for optimal cell, proliferation, and function [146, 147]. The actual number of live CMs derived from the best fit curve can be found in Appendix 2.3 (for 3D models) and Appendix 2.4 (for 2D models) respectively.

4.5.3 Confirmation of the cardioprotective effects of Tiron and NAC in the presence of DOX

To further illustrate the cardioprotective effects of NAC and Tiron in the presence of DOX, Live/Dead images were acquired (Figures 4.5A and 4.5C and Figures 4.6A and 4.6C). To visualize such effects on cardiac cells, quantitative analysis was performed on the acquired images and results indicated that the % CV of CMs in the 3D bioprinted spheroidal droplets decreased from $85\pm13\%$ on day 1 to $42\pm13\%$ on day 5 ($p<0.05$) when 1mM Tiron (Figure 4.5B) was added, and from $89\pm13\%$ on day 1 to $52\pm6\%$ on day 5 ($p<0.05$) when 8mM of Tiron (Figure 4.5B) was added. But with the addition of 15mM of Tiron (Figure 4.5B), no statistically significant difference was observed in % CV between day 1 ($95\pm11\%$) and day 5 ($93\pm9\%$) (Figure 4.5B) with $p>0.05$. With 1mM of NAC (Figure 4.5D), % CV decreased from $84\pm12\%$ on day 1 to $52\pm4\%$ ($p<0.05$) on day 5 and from $94\pm11\%$ on day 1 to $54\pm3\%$ ($p<0.05$) on day 5 when 8mM NAC (Figure 4.5D) was added. But with the addition of 15mM of NAC (Figure 4.5D), no statistically significant difference was observed in % CV between day 1 ($93\pm14\%$) and day 5 ($96\pm4\%$) with $p>0.05$.

(A) 1 Day

Tiron — NAC

1mM, 8mM, 15mM, Control

(B)
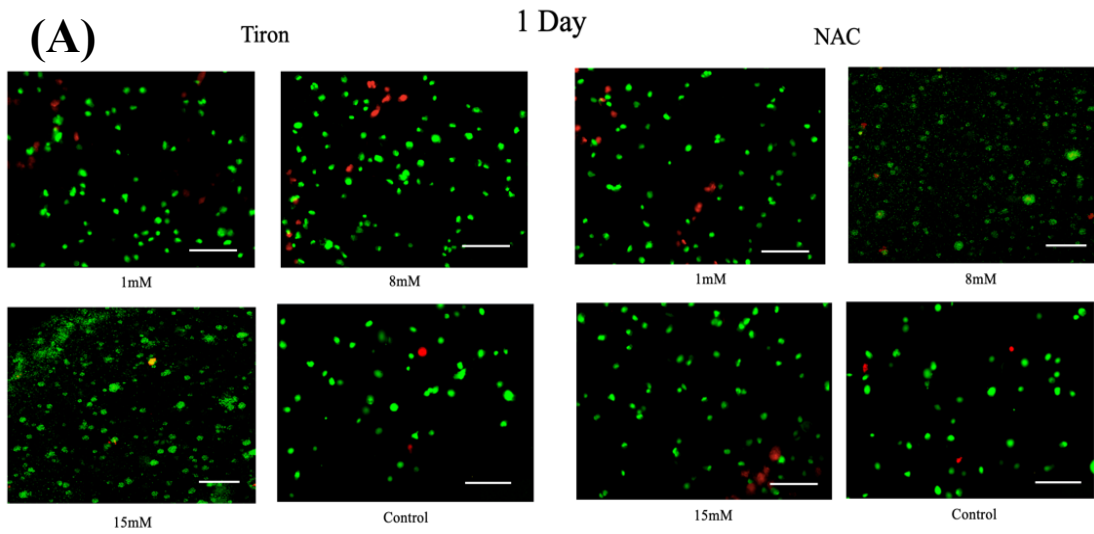
		Day 1 % Cell Viability (% CV)	Day 5 % Cell Viability (% CV)
Tiron	**1mM**	85 ± 13%	42 ± 13%
	8mM	89 ± 13%	52 ± 6%
	15mM	95 ± 11%	93 ± 9%
	Control (NO DOX)	94 ± 9%	94 ± 6%

(C) 5 Day

Tiron — NAC

1mM, 8mM, 15mM, Control
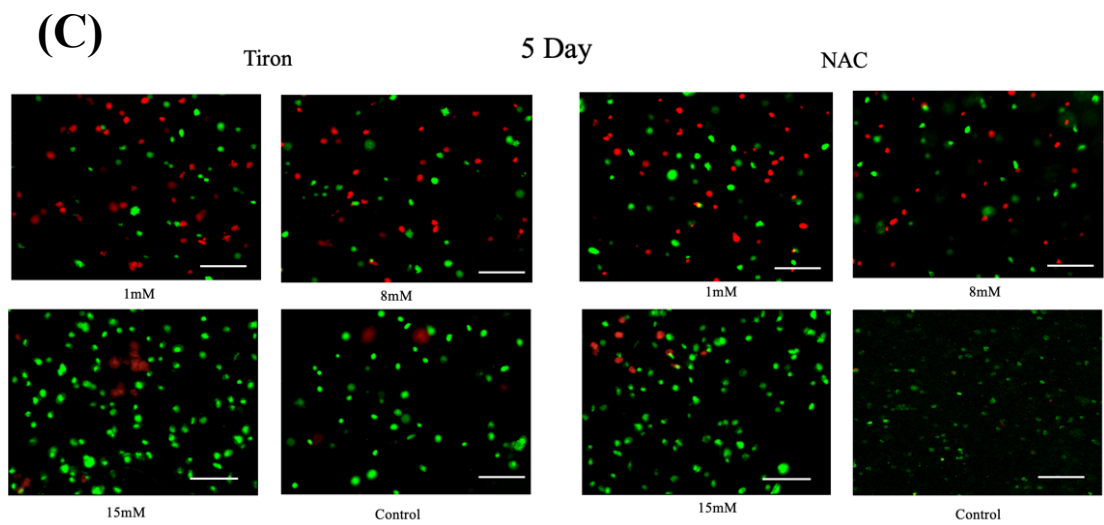
(D)		Day 1 % Cell Viability (% CV)	Day 5 % Cell Viability (% CV)
NAC	1mM	84 ± 12%	52 ± 4%
	8mM	94 ± 11%	54 ± 3%
	15mM	93 ± 14%	96 ± 4%
	Control (NO DOX)	95 ± 3%	94 ±12%

Figure 4.5: Live/Dead assay analysis representing the effects of supplementing Tiron/NAC on CMs using 3D spheroidal droplets. Representative fluorescence images of live/dead staining of CMs treated with increasing concentrations (1mM, 8mM, and 15mM) of Tiron and NAC respectively and 1μM DOX. Live cells are stained in green by calcein AM and dead cells stained in red by ethidium homodimer after (A) 1 day and (C) 5 days of culture. (B, D) Tables representing the percent live/dead cells of CMs. The scale bar corresponds to 100μm.

For 2D control samples, the % CV of cardiomyocytes decreased from 94±7% on day 1 to 57±9% on day 5 ($p<0.05$) when 1mM of Tiron (Figure 4.6B) was added and from 89±13% on day 1 to 43±9% on day 5 ($p<0.05$) when 8mM of Tiron (Figure 4.6B) was added. But with the addition of 15mM of Tiron (Figure 4.6B), no statistically significant difference was observed in % CV between day 1 (89±22%) and day 5 (95±6%) (Figure 4.6B) with $p>0.05$. With 1mM of NAC (Figure 4.6D), %CV decreased from 90±7% on day 1 to 56±8% ($p<0.05$) on day 5 and from 90±12% on day 1 to 49±12% ($p<0.05$) on day 5 when 8mM NAC (Figure 4.6D) was added. But with the addition of 15mM of NAC (Figure 4.6D), no statistically significant difference was observed in % CV between day 1 (96±5%) and day 5 (95±6%) with $p>0.05$. Quantitative analysis of representative Live-Dead images acquired when 3mM, 5mM, and 10mM of NAC and Tiron were added can be found in Appendix A.2.7 and Appendix A.2.10 for 3D and 2D samples respectively. Images of negative control hydrogel scaffolds with DOX acquired using 43 DsRed filter can be found in Appendix A.2.14. % CV data collected from the Live-Dead assay further corroborates the cardioprotective role of Tiron and NAC against the induced cardiotoxic effects of doxorubicin as shown by other published research articles [112, 148].

(A) Tiron   1 Day   NAC

1mM   8mM

15mM   Control

1mM   8mM

15mM   Control

(B)
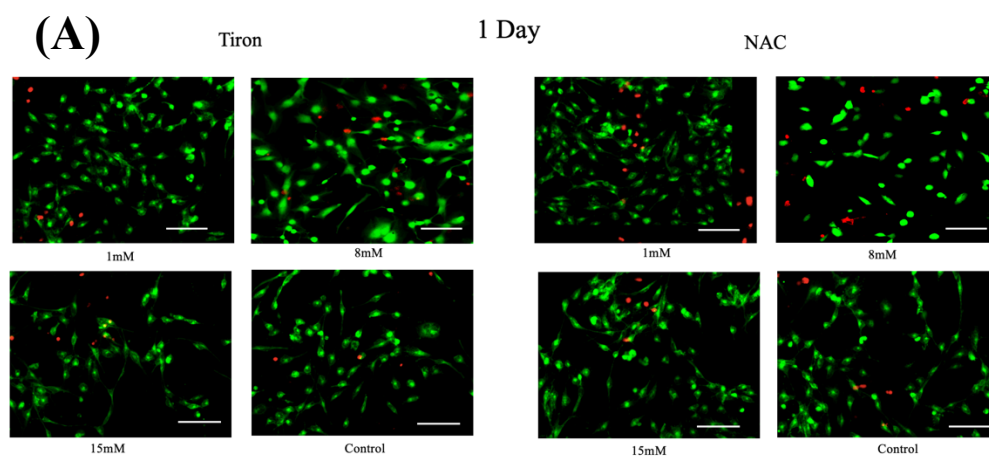
		Day 1 % Cell Viability (% CV)	Day 5 % Cell Viability (% CV)
Tiron	**1mM**	94 ± 7%	57 ± 9%
	8mM	89 ± 13%	43 ± 9%
	15mM	89 ± 22%	95 ± 6%
	Control (NO DOX)	95 ± 4%	94 ± 6%

(C) Tiron   5 Day   NAC

1mM   8mM

15mM   Control

1mM   8mM
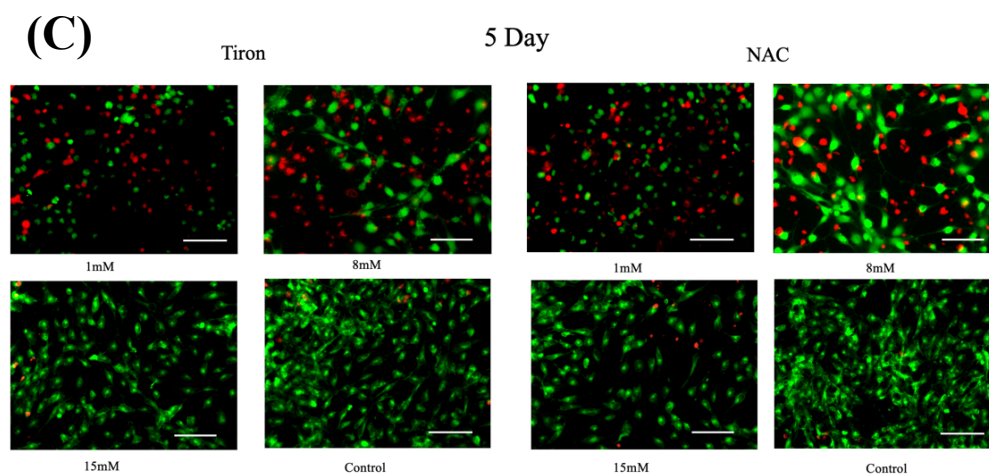
15mM   Control

(D)		Day 1 % Cell Viability (% CV)	Day 5 % Cell Viability (% CV)
NAC	1mM	90 ± 7%	56 ± 8%
	8mM	90 ± 12%	49 ± 12%
	15mM	96 ± 5%	95 ± 6%
	Control (NO DOX)	93 ± 8%	94 ± 7%

Figure 4.6: Live/Dead assay analysis representing the effects of supplementing Tiron/NAC on 2D samples with CM. Representative fluorescence images of live/dead staining of CMs gown on 2D models treated with increasing concentrations of AO (1mM, 8mM, and 15mM) and 1μM DOX. Live cells are stained in green by calcein AM and dead cells stained in red by ethidium homodimer treated with Tiron and NAC after (A) 1 day and (C) 5 days of culture. (B, D) Tables representing the percent live/dead cells of CMs. The scale bar corresponds to 100μm.

The OD trends and %CV were comparable between the 3D bioprinted spheroidal droplet scaffolds and CMs cultured in 2D cell cultures showing that this is a valid model. Because the 3D bioprinted spheroidal scaffolds serve as a desirable microenvironment for cells, in the future, other cell types can be seeded in the 3D bioprinted spheroidal scaffolds which can be utilized for other drug screening and drug cytotoxicity assays.

4.5.4   Mechanistic Insights on DOX-induced Cardiotoxicity

To gain insight into the cardiotoxic effects induced by DOX on CMs and how those were mitigated by the addition of 15mM of Tiron and NAC, we examined caspase-3 activity in the 3D bioprinted spheroids (Figure 4.7) and 2D samples (Figure 4.8). Experimental groups included CMs samples with DOX, AOs (Tiron & NAC), and NucView488 Cas-3 substrate (SUB), while control samples included CMs with caspase-3 inhibitor (Ac-DEVD-CHO), AOs (Tiron & NAC), and NucView488 Cas-3 substrate. Using a microplate reader, a significant difference ($p < 0.05$) was observed in the measured mean fluorescence units (MFU) expressing Cas-3 activity for the 3D bioprinted spheroidal droplets (Figure 4.7) between the group that contained DOX+SUB

(6216±823) and the groups that had Tiron+SUB (2829±386); NAC+SUB (3172±520); CM + SUB (3254±335); Inhibitor+SUB (3448±404), DOX+NAC+SUB (3553±430) and DOX+Tiron + SUB (3637±362) at day 1 with p<0.05. A similar trend in MFU was observed on day 3 but was not significant compared to day 1 (p>0.05).

(A)
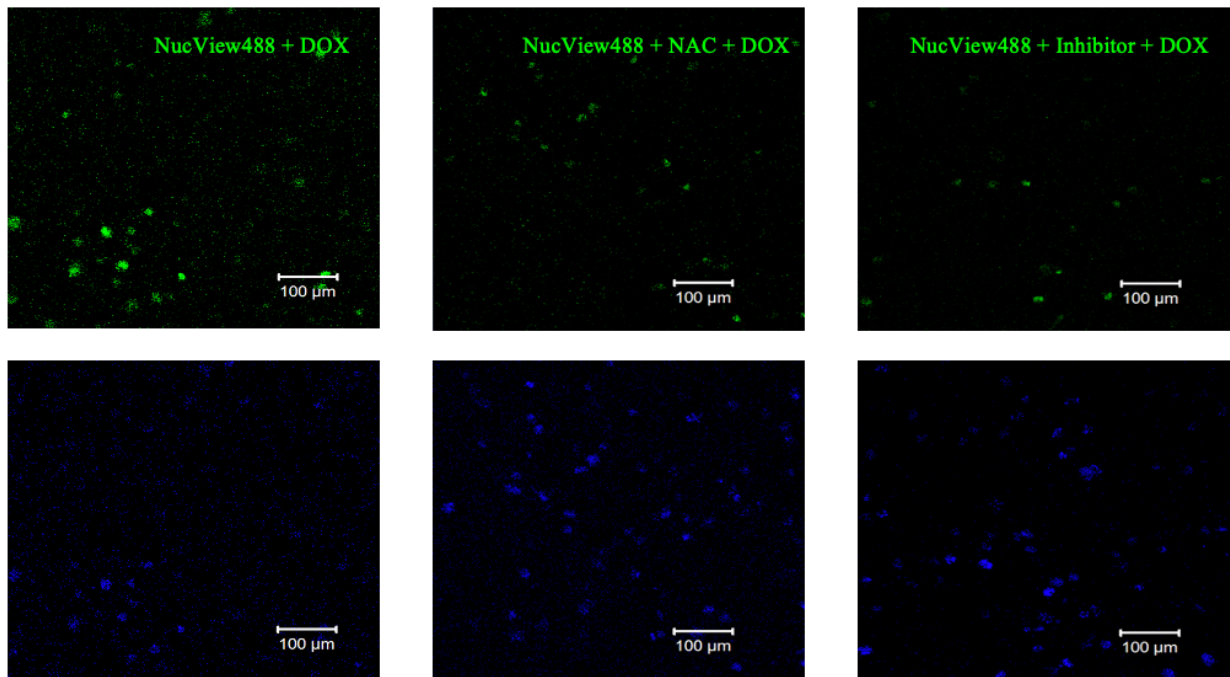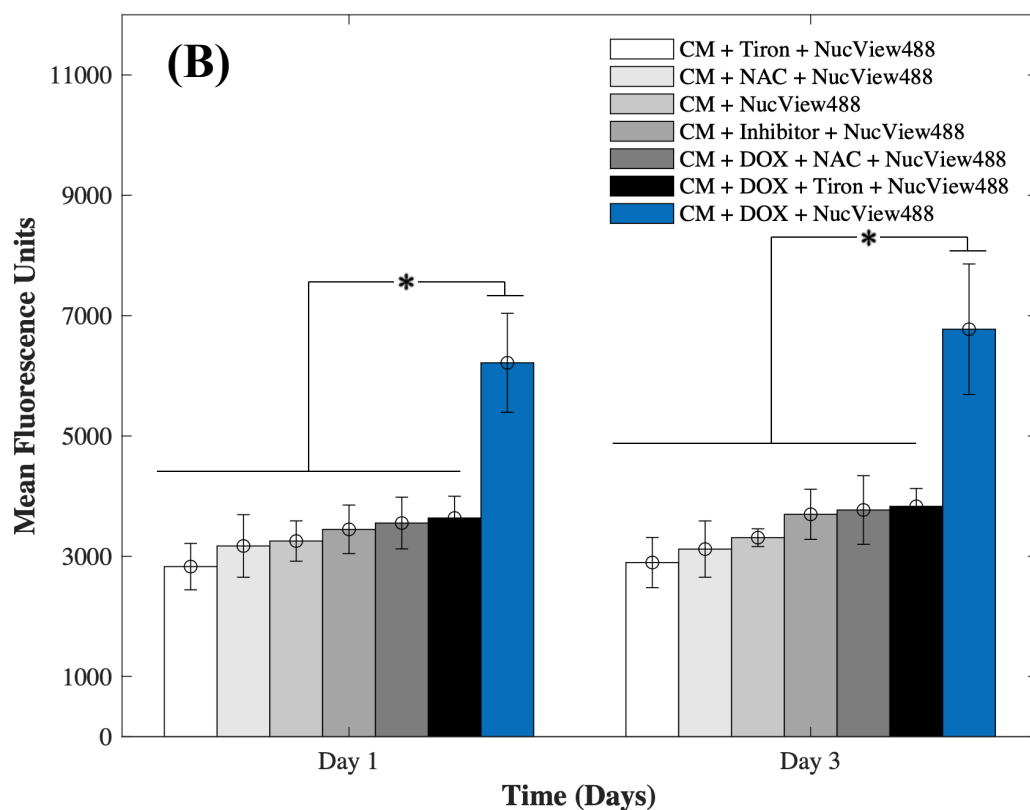
Figure 4.7: Evaluation of the caspase-3 activity of CMs in the 3D bioprinted spheroidal droplets. (A) Representative fluorescence images of experimental and control groups of caspase-3 activated cardiomyocytes after adding 1μM DOX and AOs compared to the control group captured on day 3 of culture. (B) Bar chart illustrating their relative mean fluorescence intensity. *p* values were found to be all statistically different. The scale bar corresponds to 100 μm.

For 2D samples, a significant difference ($p<0.05$) was observed in the MFU expressing cas-3 activity (Figure 4.8) between the group that contained DOX+SUB (6974 ± 841) and the groups that contained Tiron+SUB (3796 ± 363); NAC+SUB (3881 ± 531); CMs+SUB (3841 ± 321); Inhibitor+SUB (3901 ± 399); DOX+NAC+SUB (4242 ± 417); and DOX+Tiron+SUB (4334 ± 371). A similar trend in MFU was observed on day 3 but was not significant compared to day 1 ($p>0.05$). The NucView488 Cas-3 substrate, which was used to measure Cas-3 mediated apoptosis on CMs, was shown to have the highest emitted fluorescence in the group in which DOX was only added and the least fluorescence with Tiron/NAC or the Cas-3 inhibitor. This data implied the initiation of the apoptosis pathway in CMs triggered by the caspase cell

signaling pathway via DOX administration. But with the addition of Tiron & NAC, which are strong antioxidants, stimulated cell survival under such conditions and counteracted the effects of DOX [149]. The thickness of hydrogel scaffolds can interfere with the passage of emitted fluorescent light, which is reflected in a slight but consistent decrease in average intensity among the experimental and control groups [150].

(A)
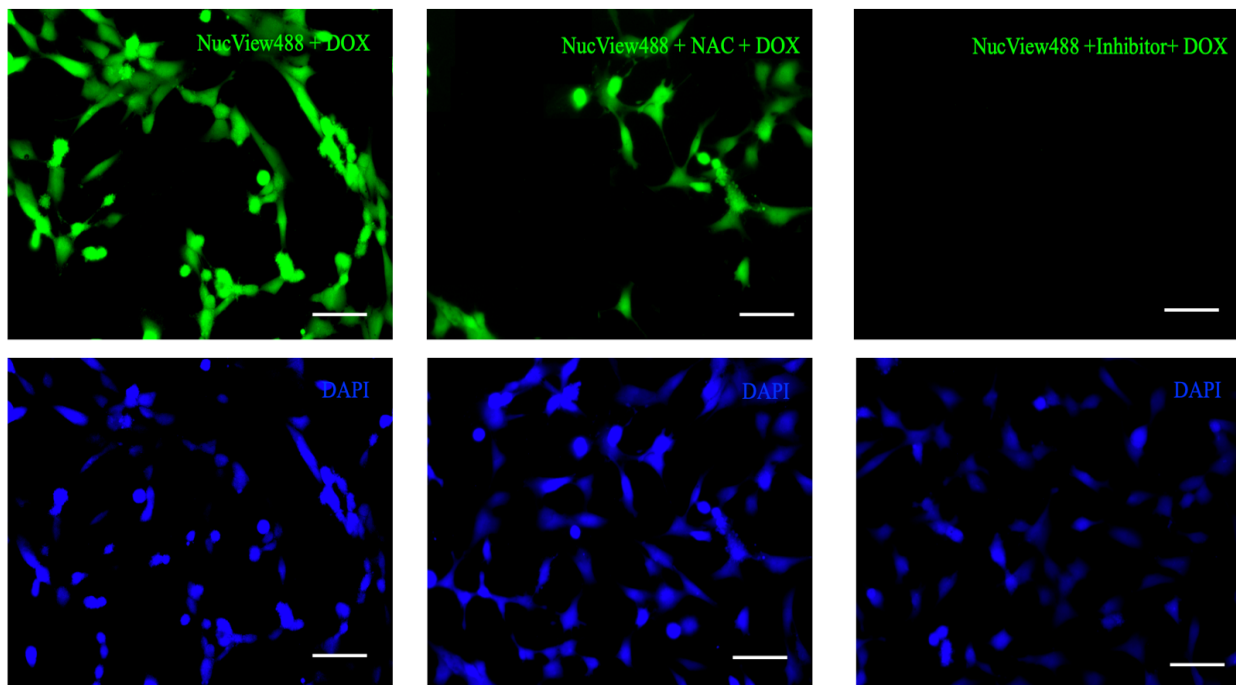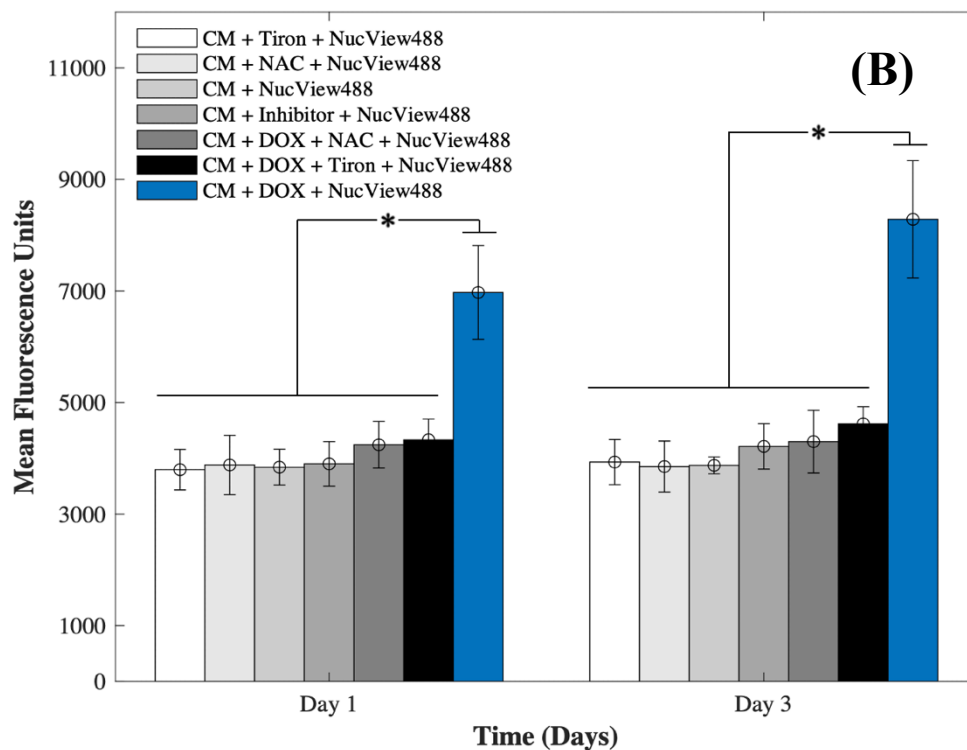
Figure 4.8: Evaluation of caspase-3 activity of CMs in 2D samples. (A) Representative fluorescence images of experimental and control groups of caspase-3 activated cardiomyocytes after adding 1µM DOX and Tiron/NAC compared to the control group captured on day 3 of culture. (B) Bar chart illustrating their relative mean fluorescence intensity. *p values were found to be all statistically different. The scale bar corresponds to 80 µm.

4.5.5   Confirmation of Oxidative Stress post-DOX Addition

Oxidative stress is a major player in DOX-induced cardiotoxicity. Moderate levels of ROS are vital for standard signal transduction processes, but elevated levels have been shown to be involved in various pathological conditions. Therefore, to study the effects of supplementing 1, 8, and 15mM of NAC on CMs in the presence of 1µM.

DOX, we examined DOX-induced oxidative stress using DHE. After oxidation, the superoxide indicator DHE binds with the cell's DNA, staining its nucleus a bright fluorescent red. Representative fluorescence images are shown in Figure 4.9A (3D samples) and Figure 4.10

72

A (2D samples). Results showed that CMs exposed to DOX alone demonstrated a significant increase in fluorescence when compared to groups where NAC was supplemented. The increase in MFU is due to an increase in ROS production in samples where NAC was not supplemented and therefore indicated higher levels of DOX-induced oxidative stress. When compared to control samples (no DOX), quantitative analysis showed a 34-fold, 17-fold, and 3-fold increase at day 1 and a 48-fold, 27-fold-fold and 4-fold in the MFU at day 3 of CMs in 3D bioprinted samples (Figure 4.9 B) with $p < 0.05$.

(A)
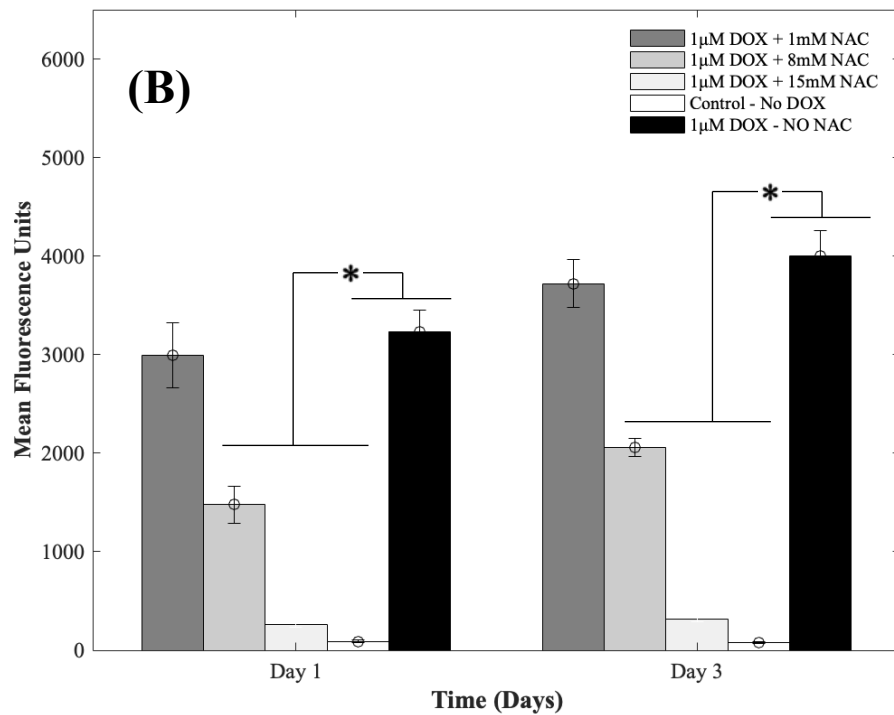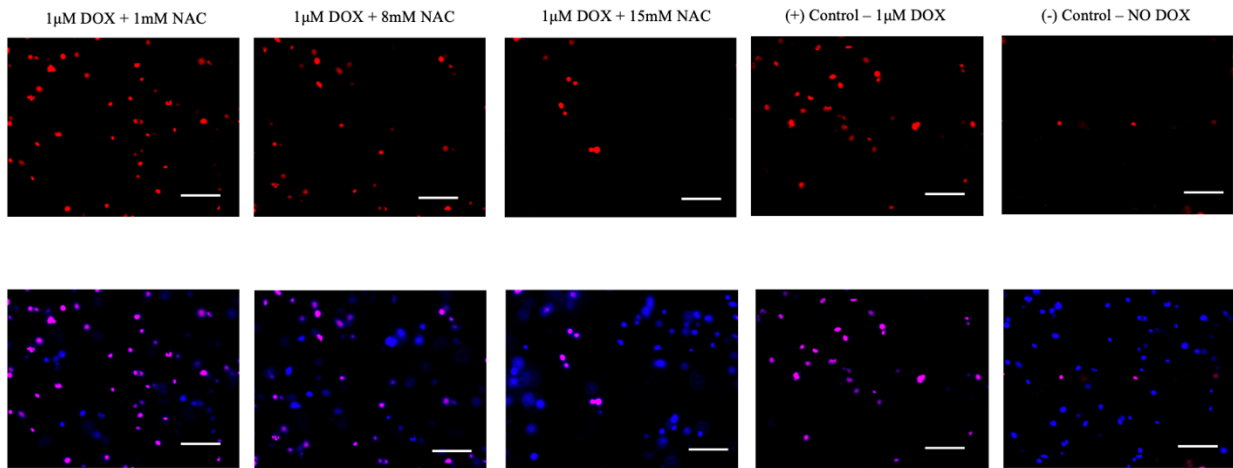
Figure 4.9: NAC antagonized doxorubicin-induced oxidative stress in 3D samples. (A) Representative fluorescence images of experimental and control groups of CMs treated with 1,8, and 15 mM of NAC and 1μM DOX on day 3 of culture. (B) Bar chart illustrating intracellular ROS production based on the relative mean fluorescence intensity. *p* values were found to be all statistically different (p<0.05). The scale bar corresponds to 100 μm.

In 2D samples, quantitative analysis showed a 39-fold, 24-fold, and 4-fold increase on day 1 and a 39-fold, 14-fold-fold and 2-fold in the mean fluorescent intensity on day 3 of CMs (Figure 4.10 B) when 1, 8, and 15mM of NAC was added respectively. Hence, a reduction in MFU intensity was due to a decrease in ROS generation. The administration of AOs such as NAC significantly mitigated the DOX-induced oxidative stress compared to untreated groups. Data for intracellular ROS production when 1, 8, and 15mM of Tiron were used can be found in Appendix A.2.11.

(A)

| 1μM DOX + 1mM NAC | 1μM DOX + 8mM NAC | 1μM DOX + 15mM NAC | (+) Control – 1μM DOX | (-) Control – NO DOX |
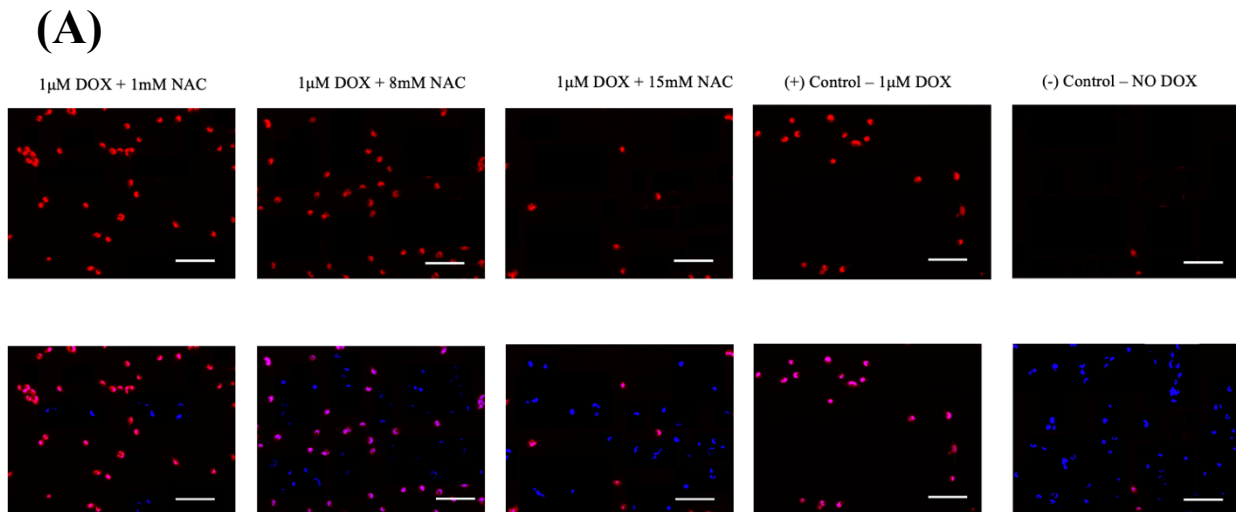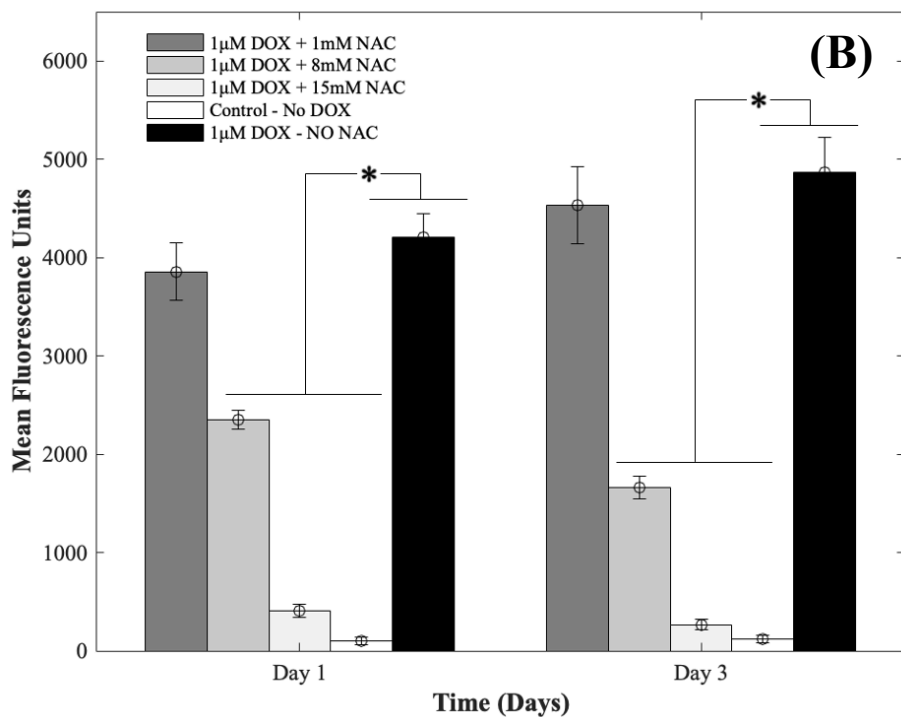
Figure 4.10: NAC antagonized doxorubicin-induced oxidative stress in 2D samples. (A) Representative fluorescence images of experimental and control groups of CMs treated with 1,8, and 15 mM of NAC and 1μM DOX on day 3 of culture. (B) Bar chart illustrating intracellular ROS production based on the relative mean fluorescence intensity. *p values were found to be all statistically different ($p<0.05$). The scale bar corresponds to 100μm.

4.5.6   Flow Cytometric-based Cell Proliferation analysis on CMs

To analyze the proliferation trends of cardiomyocytes with DOX, CMs were prestained with CTV dye (ex405nm/em450nm) and extracted at each time point, and analyzed based on the concept of dye dilution. This permitted us to study the trends of CMs proliferation seeded in the 3D bioprinted spheroidal droplets (Figure 4.11) and 2D samples (Figure 4.12). While Tiron is a vitamin E analog and NAC is a non-toxic glutathione precursor, both are considered antioxidants that help protect cells from the damage caused by free radicals [116, 151], therefore in this experiment only NAC was supplemented. Experimental samples included CMs exposed to varying doses of only NAC (1, 8, and 15mM; Figures 4.11A-F for 3D samples/Figures 4.12A-F

for 2D samples) and 1μM DOX, whereas the positive control group (Figures 4.11G-H for 3D samples/Figures 4.12G-H for 2D samples) included samples with DOX only (no NAC), and the negative control (Figures 4.11I-J for 3D samples/Figures 4.12I-J for 2D samples) consisted of neither (no DOX, no NAC).

As shown in Figure 4.11K, the average of %CTV+ of CMs at day 1 for 3D samples when 1mM (91.87±5.3%), 8mM (88.07±7.63%), 15mM (87.75±8.56%) of NAC was added respectively were not significant ($p > 0.05$) when compared to the positive (88.27±9.79%) and negative (87.02±4.82%) control group indicating a steady rate of proliferation of live CMs extracted from the 3D bioprinted spheroidal droplet at day 1.

On day 3, the average of %CTV+ of CMs at day 1 when 1mM (88.84±3.83%), 8mM (93.11±1.37%), 15mM (88.16±7.81%) of NAC and the positive control (87.29±2.99%) were all statistically significant ($p < 0.05$) to the negative control (78.77±0.4%) indicating that CMs did not significantly proliferate when 1μM of DOX was added with varying concentration of NAC when compared to normal conditions. Moreover, the average change in %CTV+ when 1mM of NAC (-3.29±0.02%), 8mM NAC (5.72±0.07%), 15mM NAC (0.47±0.008%), the positive control (-1.12±0.01%) were all statistically significant ($p < 0.05$) to the negative control sample (-9.48±0.05%).

Day 1
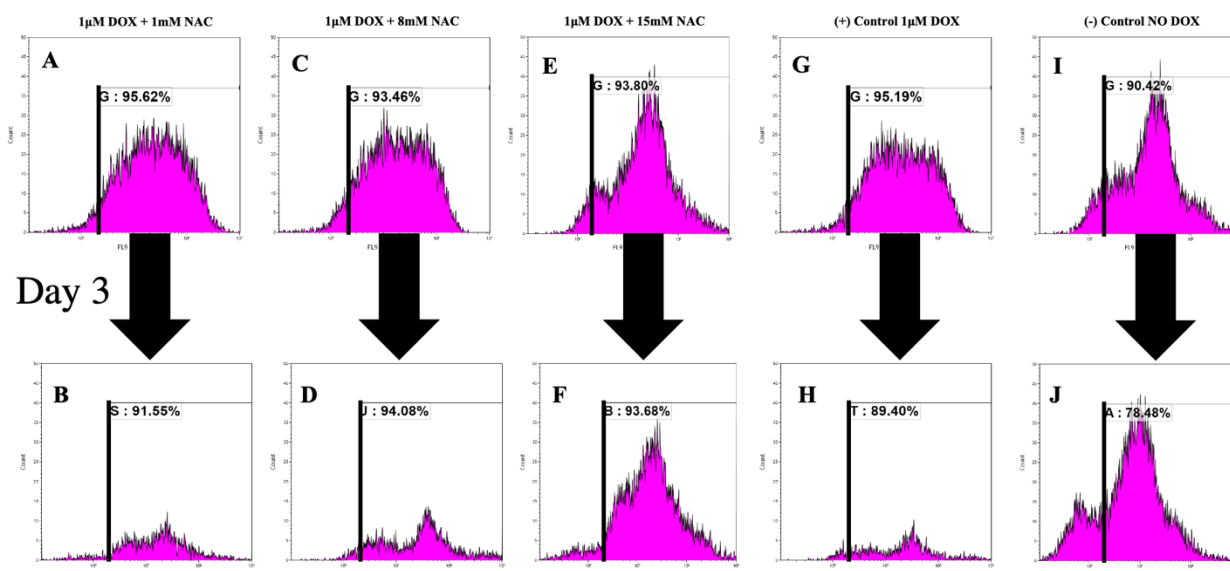
| | 1µM DOX + 1mM NAC | 1µM DOX + 8mM NAC | 1µM DOX + 15mM NAC | (+) Control 1µM DOX | (-) Control NO DOX |
| A | G : 95.62% | C G : 93.46% | E G : 93.80% | G G : 95.19% | I G : 90.42% |

Day 3

| B S : 91.55% | D J : 94.08% | F B : 93.68% | H T : 89.40% | J A : 78.48% |

K		1µM DOX + 1mM NAC	1µM DOX + 8mM NAC	1µM DOX + 15mM NAC	(+) Control 1µM DOX	(-) Control NO DOX
Day 1	Average %CTV+	91.87±5.3%	88.07±7.63%	87.75±8.56%	88.27±9.79%	87.02±4.82%
Day 3	Average %CTV+	88.84±3.83%	93.11±1.37%	88.16±7.81%	87.29±2.99%	78.77±0.40
% Change (DAY 1 – DAY 3)		*-3.29±0.02%*	*5.72±0.07%*	*0.47±0.008%*	*-1.12±0.01%*	*-9.48±0.05%*

Figure 4.11: Analysis of the effect of DOX and NAC using FACS analysis within the 3D bioprinted spheroidal droplets. Cardiomyocytes were prestained with CellTrace Violet (CTV) and mixed with the bioink prior to 3D bioprinting. Cells were extracted from the scaffolds from the experimental and control groups and analyzed using a flow cytometer. Representative graphs (A, C, E, G, and I) indicate the %CTV+ after 1 day of culture and (B, D, F, H, and J) after 3 days of culture. Shown in is K is the average of %CTV+ of prestained CMs on days 1 and 3.

For 2D samples, the average of %CTV+ (Figure 4.12K) of CMs at day 1 when 1mM (93.83±1.97%), 8mM (93.66±0.98%), 15mM (89.35±5.14%) of NAC was added respectively were not significant ($p > 0.05$) when compared to the positive (92.64±0.32%) and negative (89.22±4.71%) control group indicating a steady rate of proliferation of live CMs at day 1.

On day 3, the average of %CTV+ of CMs at day 1 when 1mM (94.19±0.17%), 8mM (94.04±1.64%), 15mM (93.72±1.96%) of NAC and the positive control (94.21±2.12%) were all

statistically significant (p<0.05) to the negative control (74.67±1.03%) indicating that CMs did not significantly proliferate when 1μM of DOX was added with varying concentration of NAC when compared to normal conditions. Moreover, the average change in %CTV+ when 1mM of NAC (0.38±0.02%), 8mM NAC (0.41±0.007%), 15mM NAC (4.89±0.03%), the positive control (1.69±0.02%) were all statistically significant (p<0.05) to the negative control sample (-16.17±0.04%).

Day 1
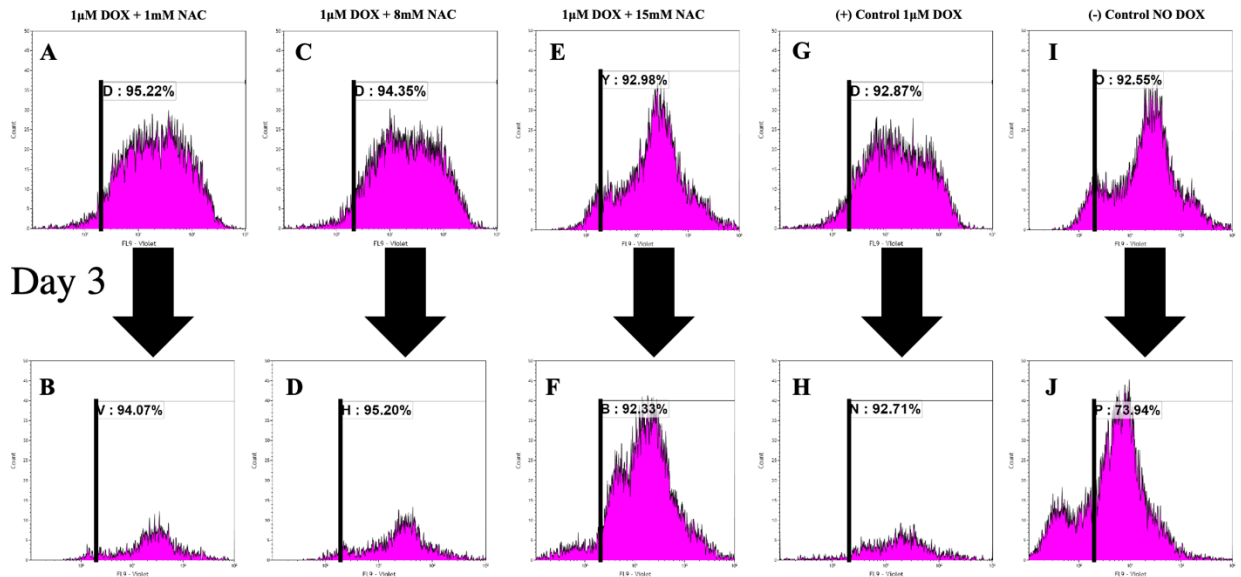
Day 3

K		1μM DOX + 1mM NAC	1μM DOX + 8mM NAC	1μM DOX + 15mM NAC	(+) Control 1μM DOX	(-) Control NO DOX
Day 1	Average %CTV+	93.83±1.97%	93.66±0.98%	89.35±5.14%	92.64±0.32%	89.22±4.71%
Day 3	Average %CTV+	94.19±0.17%	94.04±1.64%	93.72±1.96%	94.21±2.12%	74.67±1.03%
% Change (DAY 1 – DAY 3)		0.38±0.02%	0.41±0.007%	4.89±0.03%	1.69±0.02%	-16.17±0.04%

Figure 4.12: Analysis of the effect of DOX and NAC using FACS analysis in 2D samples. Cardiomyocytes were prestained with CellTrace Violet (CTV) and mixed with the bioink prior to 3D bioprinting. Cells were extracted from the scaffolds and analyzed using a flow cytometer. Representative graphs (A, C, E, G, and I) indicate the %CTV+ after 1 day of culture and (B, D, F, H, and J) after 3 days of culture. Shown in is K is the average of %CTV+ of prestained CMs on days 1 and 3.

Results indicate that with 1mM, 8mM and 15mM of NAC cells were not proliferating based on the concept of dye dilution between day 1 and day 3 compared to the negative control sample where DOX was not added. Positive controls included freshly isolated and prestained CMs with CTV while negative controls included freshly isolated and non-stained cells analyzed using FACS (Appendix A.2.12).

4.5.7   Gene Expression and Evaluation of CMs using qPCR

The GJA1 gene delivers instructions for the transcription of a protein called connexin 43, one component of a large family of connexin proteins. Moreover, connexins play a major role in cell-to-cell communication by forming channels, or gap junctions [152]. In an attempt to study the expression of GJA1, a gene from which CX-43 protein is translated, in the 3D bioprinted spheroidal droplets in comparison with 2D controls, CMs were extracted using both models on day 5 and analyzed using a thermocycler. As shown in Figure 13, results indicated statistical significance enhancement of the expression of the GJA1 gene between the 3D spheroidal droplet and the 2D control samples ($p > 0.05$).
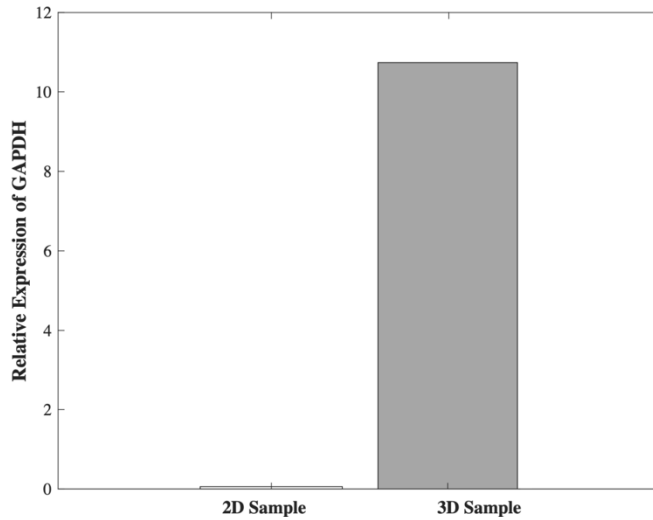
Figure 4.13: qPCR Analysis. Relative expression levels of GJA1 in the 2D control samples and the 3D spheroidal droplets normalized to GAPH.

Higher GJA1 expression in the 3D spheroidal droplets, when compared to 2D samples, is associated with increased levels of CX-43 protein essential for allowing diffusional movement of metabolites, ions, and potential intracellular communication between the adjacent cells [79, 107]. Moreover, CX-43 forms gap junction channels necessary for the spread of electrical signals, an essential aspect of the cardiac tissue [153].

4.6   Conclusion

In this pilot study, the key objective was to compare the traditional method for evaluating cytotoxicity using 2D tissue cultures with a developed 3D bioprinted spheroidal droplet model for high throughput testing. For this, we utilized a previously fabricated and optimized 3D bioprinted cardiac spheroidal model and evaluated the cardiotoxic effects of doxorubicin against AC16 cardiomyocytes. Unlike cell suspensions and tissue culture cellular monolayers, tissue-engineered constructs have a 3D structure to superiorly simulate the substantial impact that cell-to-cell and cell-to-matrix interactions influence cell behavior in in-vivo tissue and organ systems; a feature that 2D cell and tissue cultures cannot emulate well. In the future, the parameters of the

spheroidal droplet model can be additionally optimized to express a wider range of human-derived tissue-engineered equivalents allowing the examination of various cells and their interactions in a more biomimetic environment. While 3D cell culture systems offer a better way of representing human tissue in vitro, the 3D bioprinted cardiac model can be utilized for other drug screening and drug cytotoxicity assays to evaluate how cells are affected by drugs, disease, or injury.

4.7   Acknowledgments

Reference:

1. Diagnostics, C., *Cardiac Disease.* 2022.

2. Xie, Z., et al., *3D Bioprinting in Tissue Engineering for Medical Applications: The Classic and the Hybrid.* Polymers, 2020. **12**(8): p. 1717.

3. Sharma, S., et al., *Nanostructured Materials for Food Applications: Spectroscopy, Microscopy and Physical Properties.* Bioengineering, 2019. **6**(1): p. 26.

4. Association, A.H., *2021 Heart Disease and Stroke Statistics Update Fact Sheet.* 2021.

5. Machaalani, M., et al., *Knowledge, Attitude, and Practice Toward Cardiovascular Diseases in the Lebanese Population.* Global Heart, 2022. **17**(1).

6. Chen, X., et al., *Ferroptosis and cardiovascular disease: role of free radical-induced lipid peroxidation.* Free Radical Research, 2021. **55**(4): p. 405-415.

7. Korjian, S. and C.M. Gibson, *Chest Pain*, in *Handbook of Inpatient Cardiology*. 2020, Springer. p. 389-404.

8. Bonnet, F., et al., *Anxiety and depression are associated with unhealthy lifestyle in patients at risk of cardiovascular disease.* Atherosclerosis, 2005. **178**(2): p. 339-344.

9. Bezinover, D. and F. Saner, *Organ transplantation in the modern era*. 2019, Springer. p. 1-4.

10. Pham, M.T., et al., *Generation of human vascularized brain organoids.* Neuroreport, 2018. **29**(7): p. 588-593.

11. Jain, R., A. Poleshko, and J.A. Epstein, *Beating the odds: programming proliferation in the mammalian heart.* Genome medicine, 2018. **10**(1): p. 1-3.

12. Zuppinger, C., *3D Cardiac Cell Culture: A Critical Review of Current Technologies and Applications.* Frontiers in cardiovascular medicine, 2019. **6**: p. 87-87.

13. Chaicharoenaudomrung, N., P. Kunhorm, and P. Noisa, *Three-dimensional cell culture systems as an in vitro platform for cancer and stem cell modeling.* World journal of stem cells, 2019. **11**(12): p. 1065-1083.

14. Kim, J., et al., *3D Cell Printing of Tissue/Organ-Mimicking Constructs for Therapeutic and Drug Testing Applications.* International Journal of Molecular Sciences, 2020. **21**(20).

15. Qasim, M., et al., *3D printing approaches for cardiac tissue engineering and role of immune modulation in tissue regeneration.* International journal of nanomedicine, 2019. **14**: p. 1311-1333.

16. Kapałczyńska, M., et al., *2D and 3D cell cultures - a comparison of different types of cancer cell cultures.* Archives of medical science : AMS, 2018. **14**(4): p. 910-919.

17. Peng, W., et al., *3D bioprinting for drug discovery and development in pharmaceutics.* Acta Biomater, 2017. **57**: p. 26-46.

18. Mandrycky, C., et al., *3D bioprinting for engineering complex tissues.* Biotechnology Advances, 2016. **34**(4): p. 422-434.

19. Cui, H., et al., *3D Bioprinting for Organ Regeneration.* Adv Healthc Mater, 2017. **6**(1).

20. Pinto, B., et al., *Three-Dimensional Spheroids as In Vitro Preclinical Models for Cancer Research.* Pharmaceutics, 2020. **12**(12).

21.   Lazzari, G., P. Couvreur, and S. Mura, *Multicellular tumor spheroids: a relevant 3D model for the in vitro preclinical investigation of polymer nanomedicines.* Polymer Chemistry, 2017. **8**(34): p. 4947-4969.

22.   Benam, K.H., et al., *Engineered in vitro disease models.* Annu Rev Pathol, 2015. **10**: p. 195-262.

23.   Eschenhagen, T., C. Mummery, and B.C. Knollmann, *Modelling sarcomeric cardiomyopathies in the dish: from human heart samples to iPSC cardiomyocytes.* Cardiovascular Research, 2015. **105**(4): p. 424-438.

24.   Mitcheson, J.S., J.C. Hancox, and A.J. Levi, *Cultured adult cardiac myocytes: future applications, culture methods, morphological and electrophysiological properties.* Cardiovasc Res, 1998. **39**(2): p. 280-300.

25.   Joseph, J.S., S.T. Malindisa, and M. Ntwasa, *Two-dimensional (2D) and three-dimensional (3D) cell culturing in drug discovery.* Cell Culture, 2018. **2**: p. 1-22.

26.   Melissaridou, S., et al., *The effect of 2D and 3D cell cultures on treatment response, EMT profile and stem cell features in head and neck cancer.* Cancer Cell International, 2019. **19**(1): p. 16.

27.   Sacchetto, C., et al., *Modeling cardiovascular diseases with hiPSC-derived cardiomyocytes in 2D and 3D cultures.* International Journal of Molecular Sciences, 2020. **21**(9): p. 3404.

28.   Jensen, C. and Y. Teng, *Is it time to start transitioning from 2D to 3D cell culture?* Frontiers in molecular biosciences, 2020. **7**: p. 33.

29.   Murphy, S.V. and A. Atala, *3D bioprinting of tissues and organs.* Nat Biotechnol, 2014. **32**(8): p. 773-85.

30. Datta, P., et al., *3D bioprinting for reconstituting the cancer microenvironment.* npj Precision Oncology, 2020. **4**(1): p. 1-13.

31. Ma, X., et al., *3D bioprinting of functional tissue models for personalized drug screening and in vitro disease modeling.* Advanced drug delivery reviews, 2018. **132**: p. 235-251.

32. Gao, B., et al., *4D Bioprinting for Biomedical Applications.* Trends Biotechnol, 2016. **34**(9): p. 746-756.

33. Rowley, J.A., G. Madlambayan, and D.J. Mooney, *Alginate hydrogels as synthetic extracellular matrix materials.* Biomaterials, 1999. **20**(1): p. 45-53.

34. Zhu, J. and L.-H. Cai, *All-Aqueous Printing of Viscoelastic Droplets in Yield-Stress Fluids.* Acta Biomaterialia, 2022.

35. Alonzo, M., et al., *A comparative study in the printability of a bioink and 3D models across two bioprinting platforms.* Materials Letters, 2020. **264**: p. 127382.

36. Cho, D.-W., et al., *3D bioprinting techniques*, in *3D Bioprinting*. 2019, Springer. p. 25-29.

37. Xu, C., et al., *Scaffold-free inkjet printing of three-dimensional zigzag cellular tubes.* Biotechnology and Bioengineering, 2012. **109**(12): p. 3152-3160.

38. Abdolmaleki, H., P. Kidmose, and S. Agarwala, *Droplet-based techniques for printing of functional inks for flexible physical sensors.* Advanced Materials, 2021. **33**(20): p. 2006792.

39. Zhang, P. and A.R. Abate, *High-Definition Single-Cell Printing: Cell-by-Cell Fabrication of Biological Structures.* Advanced Materials, 2020. **32**(52): p. 2005346.

40. Kérourédan, O., et al., *In situ prevascularization designed by laser-assisted bioprinting: effect on bone regeneration.* Biofabrication, 2019. **11**(4): p. 045002.

41.   Ruiz-Alonso, S., et al., *Current Insights into 3D Bioprinting: An Advanced Approach for Eye Tissue Regeneration.* Pharmaceutics, 2021. **13**(3): p. 308.

42.   Cernencu, A.I., *3D Printing of Hydrogel Constructs Toward Targeted Development in Tissue Engineering*, in *3D printable Gel-inks for Tissue Engineering*. 2021, Springer. p. 79-127.

43.   Li, J., et al., *3D printing of hydrogels: Rational design strategies and emerging biomedical applications.* Materials Science and Engineering: R: Reports, 2020. **140**: p. 100543.

44.   Cleetus, C.M., et al., *Alginate Hydrogels with Embedded ZnO Nanoparticles for Wound Healing Therapy.* International journal of nanomedicine, 2020. **15**: p. 5097-5111.

45.   El Khoury, R., et al., *3D Bioprinted Spheroidal Droplets for Engineering the Heterocellular Coupling between Cardiomyocytes and Cardiac Fibroblasts.* Cyborg and Bionic Systems, 2021. **2021**: p. 9864212.

46.   Alonzo, M., et al., *3D Biofabrication of a Cardiac Tissue Construct for Sustained Longevity and Function.* ACS Applied Materials & Interfaces, 2022. **14**(19): p. 21800-21813.

47.   Mondal, A., et al., *Characterization and printability of Sodium alginate -Gelatin hydrogel for bioprinting NSCLC co-culture.* Scientific Reports, 2019. **9**(1): p. 19914.

48.   Nagiah, N., et al., *Development and Characterization of Furfuryl-Gelatin Electrospun Scaffolds for Cardiac Tissue Engineering.* ACS Omega, 2022.

49.   Afewerki, S., et al., *Gelatin-polysaccharide composite scaffolds for 3D cell culture and tissue engineering: Towards natural therapeutics.* Bioengineering & Translational Medicine, 2019. **4**(1): p. 96-115.

50.   Pan, T., et al., *3D Bioplotting of Gelatin/Alginate Scaffolds for Tissue Engineering: Influence of Crosslinking Degree and Pore Architecture on Physicochemical Properties.* Journal of Materials Science & Technology, 2016. **32**(9): p. 889-900.

51.   Zhang, J., et al., *Alginate dependent changes of physical properties in 3D bioprinted cell-laden porous scaffolds affect cell viability and cell morphology.* Biomedical Materials, 2019. **14**(6): p. 065009.

52.   Manzano, V.E., et al., *Alginates: hydrogels, their chemistry, and applications*, in *Alginates*. 2019, Apple Academic Press. p. 89-140.

53.   Sun, J. and H. Tan, *Alginate-Based Biomaterials for Regenerative Medicine Applications.* Materials (Basel), 2013. **6**(4): p. 1285-1309.

54.   Yao, B., et al., *Enzymatically degradable alginate/gelatin bioink promotes cellular behavior and degradation in vitro and in vivo.* Biofabrication, 2019. **11**(4): p. 045020.

55.   Theocharis, A.D., D. Manou, and N.K. Karamanos, *The extracellular matrix as a multitasking player in disease.* The FEBS journal, 2019. **286**(15): p. 2830-2869.

56.   Li, X., et al., *Functional Hydrogels With Tunable Structures and Properties for Tissue Engineering Applications.* Front Chem, 2018. **6**: p. 499.

57.   Lee, J.-H. and H.-W. Kim, *Emerging properties of hydrogels in tissue engineering.* Journal of Tissue Engineering, 2018. **9**: p. 2041731418768285.

58.   Akhtar, K., et al., *Scanning electron microscopy: Principle and applications in nanomaterials characterization*, in *Handbook of materials characterization*. 2018, Springer. p. 113-145.

59.   Ul-Hamid, A., *A beginners' guide to scanning electron microscopy*. Vol. 1. 2018: Springer.

60.   Allen, M.E., et al., *Hydrogels as functional components in artificial cell systems.* Nature Reviews Chemistry, 2022. **6**(8): p. 562-578.

61.   Zhao, Z., et al., *Injectable microfluidic hydrogel microspheres for cell and drug delivery.* Advanced Functional Materials, 2021. **31**(31): p. 2103339.

62.   Yu, C., et al., *Aliphatic Chain Modification of Collagen Type I: Development of Elastomeric, Compliant, and Suturable Scaffolds.* ACS Applied Bio Materials, 2020. **3**(3): p. 1331-1343.

63.   Mokhtari, H., et al., *An injectable mechanically robust hydrogel of Kappa-carrageenan-dopamine functionalized graphene oxide for promoting cell growth.* Carbohydrate polymers, 2019. **214**: p. 234-249.

64.   Zhang, K., et al., *Structurally dynamic hydrogels for biomedical applications: pursuing a fine balance between macroscopic stability and microscopic dynamics.* Chemical Reviews, 2021. **121**(18): p. 11149-11193.

65.   Chansoria, P., et al., *Characterizing the Effects of Synergistic Thermal and Photo-Cross-Linking during Biofabrication on the Structural and Functional Properties of Gelatin Methacryloyl (GelMA) Hydrogels.* ACS Biomaterials Science & Engineering, 2021. **7**(11): p. 5175-5188.

66.   Yazdi, M.K., et al., *Agarose-based biomaterials for advanced drug delivery.* Journal of Controlled Release, 2020. **326**: p. 523-543.

67.   Alonzo, M., et al., *Hydrogel scaffolds with elasticity-mimicking embryonic substrates promote cardiac cellular network formation.* Progress in biomaterials, 2020. **9**(3): p. 125-137.

68.   Dunst, S. and P. Tomancak, *Imaging flies by fluorescence microscopy: principles, technologies, and applications.* Genetics, 2019. **211**(1): p. 15-34.

69.   Shen, Y., et al., *Recent progress of surface-enhanced Raman spectroscopy for subcellular compartment analysis.* Theranostics, 2021. **11**(10): p. 4872.

70.   Song, Y., *Development of aggregation induced emission-boosted adaptive optical (AIE-AO) confocal microscopy for enhanced bioimaging.* 2022.

71.   Bayguinov, P.O., et al., *Modern laser scanning confocal microscopy.* Current protocols in cytometry, 2018. **85**(1): p. e39.

72.   Bowen, R.E., et al., *Statistics of heart failure and mechanical circulatory support in 2020.* Annals of translational medicine, 2020. **8**(13).

73.   Neidenbach, R., et al., *Improving medical care and prevention in adults with congenital heart disease—reflections on a global problem—part I: development of congenital cardiology, epidemiology, clinical aspects, heart failure, cardiac arrhythmia.* Cardiovascular Diagnosis and Therapy, 2018. **8**(6): p. 705.

74.   Savoji, H., et al., *Cardiovascular disease models: a game changing paradigm in drug discovery and screening.* Biomaterials, 2019. **198**: p. 3-26.

75.   Jacob, S., et al., *Strategies for Expanding Donors Pool in Heart Transplantation.* Reviews in Cardiovascular Medicine, 2022. **23**(8): p. 285.

76.   Bajaj, P., et al., *3D biofabrication strategies for tissue engineering and regenerative medicine.* Annual review of biomedical engineering, 2014. **16**: p. 247-276.

77.   Anil Kumar, S., et al., *A Comparative Study of a 3D Bioprinted Gelatin-Based Lattice and Rectangular-Sheet Structures.* Gels, 2018. **4**(3): p. 73.

78.   Alonzo, M., et al., *3D Bioprinting of cardiac tissue and cardiac stem cell therapy.* Transl Res, 2019. **211**: p. 64-83.

79.   Anil Kumar, S., et al., *A Visible Light-Cross-Linkable, Fibrin–Gelatin-Based Bioprinted Construct with Human Cardiomyocytes and Fibroblasts.* ACS Biomaterials Science & Engineering, 2019. **5**(9): p. 4551-4563.

80.   AnilKumar, S., et al., *The applicability of furfuryl-gelatin as a novel bioink for tissue engineering applications.* Journal of biomedical materials research. Part B, Applied biomaterials, 2019. **107**(2): p. 314-323.

81.   Gopinathan, J. and I. Noh, *Recent trends in bioinks for 3D printing.* Biomaterials research, 2018. **22**(1): p. 1-15.

82.   Veldhuizen, J., R.Q. Migrino, and M. Nikkhah, *Three-dimensional microengineered models of human cardiac diseases.* J. Biol. Eng., 2019. **13**: p. 29.

83.   Sharma, P. and C. Gentile, *Cardiac Spheroids as in vitro Bioengineered Heart Tissues to Study Human Heart Pathophysiology.* J Vis Exp, 2021(167).

84.   Polonchuk, L., et al., *Cardiac spheroids as promising in vitro models to study the human heart microenvironment.* Scientific reports, 2017. **7**(1): p. 1-12.

85.   Zanoni, M., et al., *3D tumor spheroid models for in vitro therapeutic screening: a systematic approach to enhance the biological relevance of data obtained.* Scientific reports, 2016. **6**(1): p. 1-11.

86.   Wust, S., et al., *Tunable hydrogel composite with two-step processing in combination with innovative hardware upgrade for cell-based three-dimensional bioprinting.* Acta Biomater, 2014. **10**(2): p. 630-40.

87.   Jeoh, T., et al., *How alginate properties influence in situ internal gelation in crosslinked alginate microcapsules (CLAMs) formed by spray drying.* PloS one, 2021. **16**(2): p. e0247171.

88.   Du, Y., et al., *Directed assembly of cell-laden microgels for fabrication of 3D tissue constructs.* Proceedings of the National Academy of Sciences of the United States of America, 2008. **105**(28): p. 9522-9527.

89.   Bakopoulou, A., et al., *Dental pulp stem cells in chitosan/gelatin scaffolds for enhanced orofacial bone regeneration.* Dent Mater, 2019. **35**(2): p. 310-327.

90.   Stowers, R.S., S.C. Allen, and L.J. Suggs, *Dynamic phototuning of 3D hydrogel stiffness.* Proc Natl Acad Sci U S A, 2015. **112**(7): p. 1953-8.

91.   Pinto, A.R., et al., *Revisiting Cardiac Cellular Composition.* Circulation research, 2016. **118**(3): p. 400-409.

92.   Adeniran, B., et al., *Improved preservation of ovarian tissue morphology that is compatible with antigen detection using a fixative mixture of formalin and acetic acid.* Human Reproduction, 2021. **36**(7): p. 1871-1890.

93.   Chimene, D., et al., *Advanced bioinks for 3D printing: a materials science perspective.* Annals of biomedical engineering, 2016. **44**(6): p. 2090-2102.

94.   Hollister, S.J., *Porous scaffold design for tissue engineering.* Nat Mater, 2005. **4**(7): p. 518-24.

95.   Annabi, N., et al., *Controlling the porosity and microarchitecture of hydrogels for tissue engineering.* Tissue engineering. Part B, Reviews, 2010. **16**(4): p. 371-383.

96.   Loh, Q.L. and C. Choong, *Three-dimensional scaffolds for tissue engineering applications: role of porosity and pore size.* Tissue engineering. Part B, Reviews, 2013. **19**(6): p. 485-502.

97.   Wang, X., et al., *Electro-spinning/netting: A strategy for the fabrication of three-dimensional polymer nano-fiber/nets.* Progress in materials science, 2013. **58**(8): p. 1173-1243.

98.   Patra, S., P.M. Ajayan, and T.N. Narayanan, *Dynamic mechanical analysis in materials science: The Novice's Tale.* Oxford Open Materials Science, 2020. **1**(1).

99.   Herrero-Herrero, M., J.A. Gómez-Tejedor, and A. Vallés-Lluch, *Role of Electrospinning Parameters on Poly(Lactic-co-Glycolic Acid) and Poly(Caprolactone-co-Glycolic acid) Membranes.* Polymers, 2021. **13**(5): p. 695.

100.   Giri, S.K., M.K. Tripathi, and N. Kotwaliwale, *Effect of composition and storage time on some physico-chemical and rheological properties of probiotic soy-cheese spread.* Journal of food science and technology, 2018. **55**(5): p. 1667-1674.

101.   Kumar, S.A., et al., *Applications of stem cells and bioprinting for potential treatment of diabetes.* World J Stem Cells, 2019. **11**(1): p. 13-32.

102.   Begum, J., et al., *A method for evaluating the use of fluorescent dyes to track proliferation in cell lines by dye dilution.* Cytometry A, 2013. **83**(12): p. 1085-95.

103.   Filby, A., et al., *An imaging flow cytometric method for measuring cell division history and molecular symmetry during mitosis.* Cytometry A, 2011. **79**(7): p. 496-506.

104.   Christidi, E. and L.R. Brunham, *Regulated cell death pathways in doxorubicin-induced cardiotoxicity.* Cell Death & Disease, 2021. **12**(4): p. 339.

105. Franco, Y.L., T.R. Vaidya, and S. Ait-Oudhia, *Anticancer and cardio-protective effects of liposomal doxorubicin in the treatment of breast cancer.* Breast cancer (Dove Medical Press), 2018. **10**: p. 131-141.

106. Hanf, A., et al., *The anti-cancer drug doxorubicin induces substantial epigenetic changes in cultured cardiomyocytes.* Chemico-Biological Interactions, 2019. **313**: p. 108834.

107. Joddar, B., et al., *Abstract 465: A 3D Bioprinted Human Cardiac Cell Platform to Model the Pathophysiology of Diabetes.* Circulation Research, 2020. **127**(Suppl_1): p. A465-A465.

108. Andrysiak, K., J. Stępniewski, and J. Dulak, *Human-induced pluripotent stem cell-derived cardiomyocytes, 3D cardiac structures, and heart-on-a-chip as tools for drug research.* Pflügers Archiv - European Journal of Physiology, 2021. **473**(7): p. 1061-1085.

109. Ingber, D.E., *Human organs-on-chips for disease modelling, drug development and personalized medicine.* Nature Reviews Genetics, 2022. **23**(8): p. 467-491.

110. Lefrak, E.A., et al., *A clinicopathologic analysis of adriamycin cardiotoxicity.* Cancer, 1973. **32**(2): p. 302-14.

111. Von Hoff, D.D., et al., *Risk factors for doxorubicin-induced congestive heart failure.* Ann Intern Med, 1979. **91**(5): p. 710-7.

112. Tadokoro, T., et al., *Mitochondria-dependent ferroptosis plays a pivotal role in doxorubicin cardiotoxicity.* JCI insight, 2020. **5**(9).

113. Yu, X., et al., *Dexrazoxane ameliorates doxorubicin-induced cardiotoxicity by inhibiting both apoptosis and necroptosis in cardiomyocytes.* Biochemical and Biophysical Research Communications, 2020. **523**(1): p. 140-146.

114. Singla, D.K., T.A. Johnson, and Z. Tavakoli Dargani, *Exosome treatment enhances anti-inflammatory M2 macrophages and reduces inflammation-induced pyroptosis in doxorubicin-induced cardiomyopathy.* Cells, 2019. **8**(10): p. 1224.

115. Hu, C., et al., *Osteocrin attenuates inflammation, oxidative stress, apoptosis, and cardiac dysfunction in doxorubicin-induced cardiotoxicity.* Clinical and Translational Medicine, 2020. **10**(3): p. e124.

116. Cui, G., et al., *Oxidative stress-mediated mitochondrial pathway-dependent apoptosis is induced by silica nanoparticles in H9c2 cardiomyocytes.* Toxicology mechanisms and methods, 2020. **30**(9): p. 646-655.

117. Antonucci, S., et al., *The determining role of mitochondrial reactive oxygen species generation and monoamine oxidase activity in doxorubicin-induced cardiotoxicity.* Antioxidants & redox signaling, 2021. **34**(7): p. 531-550.

118. Songbo, M., et al., *Oxidative stress injury in doxorubicin-induced cardiotoxicity.* Toxicology letters, 2019. **307**: p. 41-48.

119. Tripathi, R., et al., *Free radical biology in neurological manifestations: Mechanisms to therapeutics interventions.* Environmental Science and Pollution Research, 2021: p. 1-48.

120. Mortezaee, K., et al., *Redox interactions and genotoxicity of metal-based nanoparticles: A comprehensive review.* Chemico-biological interactions, 2019. **312**: p. 108814.

121. Khuanjing, T., et al., *Acetylcholinesterase inhibitor ameliorates doxorubicin-induced cardiotoxicity through reducing RIP1-mediated necroptosis.* Pharmacological Research, 2021. **173**: p. 105882.

122. Guo, X., et al., *NFκB promotes oxidative stress-induced necrosis and ischemia/reperfusion injury by inhibiting Nrf2-ARE pathway.* Free Radical Biology and Medicine, 2020. **159**: p. 125-135.

123. Dhalla, N.S., et al., *Involvement of Oxidative Stress in the Development of Subcellular Defects and Heart Disease.* Biomedicines, 2022. **10**(2): p. 393.

124. Martins-Marques, T., A. Rodriguez-Sinovas, and H. Girao, *Cellular crosstalk in cardioprotection: Where and when do reactive oxygen species play a role?* Free Radical Biology and Medicine, 2021. **169**: p. 397-409.

125. Monticone, M., et al., *NAC, Tiron and Trolox Impair Survival of Cell Cultures Containing Glioblastoma Tumorigenic Initiating Cells by Inhibition of Cell Cycle Progression.* PLOS ONE, 2014. **9**(2): p. e90085.

126. Yang, J., Y. Su, and A. Richmond, *Antioxidants tiron and N-acetyl-L-cysteine differentially mediate apoptosis in melanoma cells via a reactive oxygen species-independent NF-κB pathway.* Free Radical Biology and Medicine, 2007. **42**(9): p. 1369-1380.

127. Abdelghffar, E.A., et al., *Pea (Pisum sativum) peel extract attenuates DOX-induced oxidative myocardial injury.* Biomedicine & Pharmacotherapy, 2021. **143**: p. 112120.

128. Kumfu, S., S.C. Chattipakorn, and N. Chattipakorn, *Iron overload cardiomyopathy: Using the latest evidence to inform future applications.* Experimental Biology and Medicine, 2022. **247**(7): p. 574-583.

129. Technology, C.S., *Doxorubicin #5927.* 2022.

130. Sigma, M. *Doxorubicin hydrochloride*. 2022; Available from: https://www.sigmaaldrich.com/US/en/product/sigma/44583.
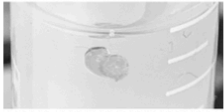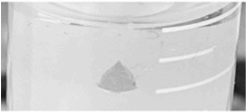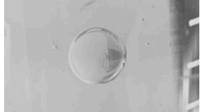
131. Dludla, P.V., et al., *N-Acetyl cysteine ameliorates hyperglycemia-induced cardiomyocyte toxicity by improving mitochondrial energetics and enhancing endogenous Coenzyme Q9/10 levels.* Toxicology Reports, 2019. **6**: p. 1240-1245.

132. Shi, R., et al., *N-acetylcysteine amide decreases oxidative stress but not cell death induced by doxorubicin in H9c2 cardiomyocytes.* BMC Pharmacol, 2009. **9**: p. 7.

133. Cailleret, M., et al., *<i>N</i>-Acetylcysteine Prevents the Deleterious Effect of Tumor Necrosis Factor-α on Calcium Transients and Contraction in Adult Rat Cardiomyocytes.* Circulation, 2004. **109**(3): p. 406-411.

134. Tu, V.C., J.J. Bahl, and Q.M. Chen, *Signals of Oxidant-Induced Cardiomyocyte Hypertrophy: Key Activation of p70 S6 Kinase-1 and Phosphoinositide 3-Kinase.* Journal of Pharmacology and Experimental Therapeutics, 2002. **300**(3): p. 1101.

135. Dludla, P.V., et al., *N-Acetyl cysteine ameliorates hyperglycemia-induced cardiomyocyte toxicity by improving mitochondrial energetics and enhancing endogenous Coenzyme Q9/10 levels.* Toxicology Reports, 2019. **6**: p. 1240-1245.

136. Zhou, Y.-F., et al., *Construction of A375· S2 Melanoma Cell Line with High Sensibility to IL-1 by Overexpressing IL-1 Receptor.* Indian Journal of Microbiology, 2022: p. 1-8.

137. Parchehbaf-Kashani, M., et al., *Design and characterization of an electroconductive scaffold for cardiomyocytes based biomedical assays.* Materials Science and Engineering: C, 2020. **109**: p. 110603.

138. Zhou, X., et al., *Fabrication of polylactic acid (PLA)-based porous scaffold through the combination of traditional bio-fabrication and 3D printing technology for bone regeneration.* Colloids and Surfaces B: Biointerfaces, 2021. **197**: p. 111420.

139.   Biotium. *NucView® 488 Caspase-3 Assay Kit for Live Cells*. Glowing products for Science 2022; Available from: https://biotium.com/product/nucviewtm-488-caspase-3-assay-kit-for-live-cells/.

140.   Cen, H., et al., *DEVD-NucView488: a novel class of enzyme substrates for real-time detection of caspase-3 activity in live cells.* The FASEB Journal, 2008. **22**(7): p. 2243-2252.

141.   Nagiah, N., et al., *Development and Characterization of Furfuryl-Gelatin Electrospun Scaffolds for Cardiac Tissue Engineering.* ACS Omega, 2022. **7**(16): p. 13894-13905.

142.   Schmittgen, T.D. and K.J. Livak, *Analyzing real-time PCR data by the comparative CT method.* Nature protocols, 2008. **3**(6): p. 1101-1108.

143.   Li, J. and D.J. Mooney, *Designing hydrogels for controlled drug delivery.* Nat Rev Mater, 2016. **1**(12).

144.   Edmondson, R., et al., *Three-dimensional cell culture systems and their applications in drug discovery and cell-based biosensors.* Assay Drug Dev Technol, 2014. **12**(4): p. 207-18.

145.   Zhao, L. and B. Zhang, *Doxorubicin induces cardiotoxicity through upregulation of death receptors mediated apoptosis in cardiomyocytes.* Scientific Reports, 2017. **7**(1): p. 44735.

146.   Nikolova, M.P. and M.S. Chavali, *Recent advances in biomaterials for 3D scaffolds: A review.* Bioact Mater, 2019. **4**: p. 271-292.

147.   Unnikrishnan, K., L.V. Thomas, and R.M. Ram Kumar, *Advancement of Scaffold-Based 3D Cellular Models in Cancer Tissue Engineering: An Update.* Front Oncol, 2021. **11**: p. 733652.

148. Xu, T., et al., *Oxidative stress in cell death and cardiovascular diseases.* Oxidative medicine and cellular longevity, 2019. **2019**.

149. Maheshwari, A., et al., *N-acetyl-L-cysteine counteracts oxidative stress and prevents H2O2 induced germ cell apoptosis through down-regulation of caspase-9 and JNK/c-Jun.* Molecular Reproduction and Development, 2011. **78**(2): p. 69-79.

150. Zhao, L., et al., *The integration of 3-D cell printing and mesoscopic fluorescence molecular tomography of vascular constructs within thick hydrogel scaffolds.* Biomaterials, 2012. **33**(21): p. 5325-5332.

151. Matsuzaki, S., et al., *Insulin signaling alters antioxidant capacity in the diabetic heart.* Redox biology, 2021. **47**: p. 102140.

152. Dong, X., et al., *p54nrb is a transcriptional corepressor of the progesterone receptor that modulates transcription of the labor-associated gene, connexin 43 (Gja1).* Molecular endocrinology, 2009. **23**(8): p. 1147-1160.

153. Joddar, B., et al., *Engineering approaches for cardiac organoid formation and their characterization.* Translational Research, 2022.

A.1.1: The evolutionary process in engineering a 3D bioprinted spheroid

Generations / Parameters	Generation I	Generation II	Generation III	Generation IV
Hydrogel Composition	2% Gelatin 3% MVG alginate			
Printer Head Temperature (°C)	28°C			
Bed Temperature (°C)	Room Temperature (25-28°C)			
Printer Speed (mm/s)	0.7 mm/s			
Extrusion Pressure (kPa)	15 kPa			
Nozzle size/Inner diameter (mm)	16 G (~1.19 mm)			
Bioink pre-heating (min)	15 min at 37°C		40 min at 37°C	N/A
Pre-addition of CaCl₂ (µL)	230 µL	N/A		5 µL
Post-addition of CaCl₂ (µL)	N/A	230 µL	80 µL	75 µL
Aspect ratio	0.9773 ± 0.4632 mm	1.2378 ± 0.1068 mm	0.7710 ± 0.2782 mm	1.0124 ± 0.0437 mm

A.1.2: Average aspect ratio (mean ± SD) calculations for GEN1-III spheroidal droplets as enlisted in **A.1.1**.
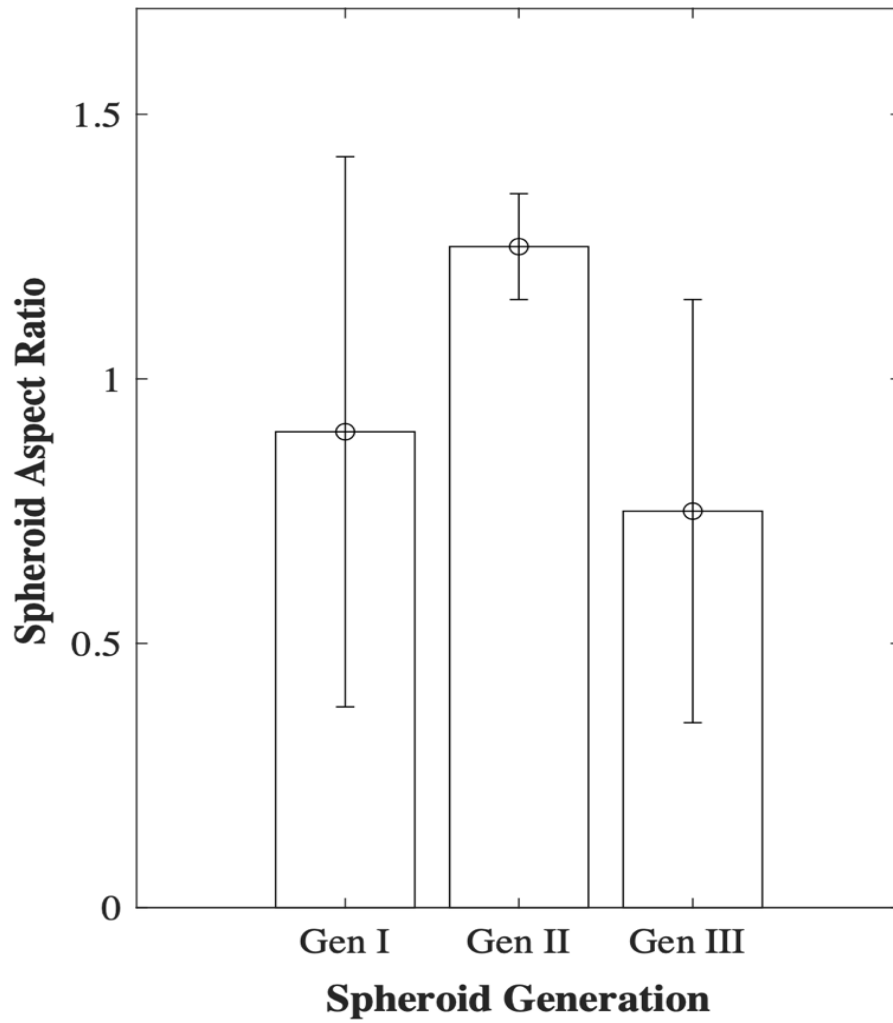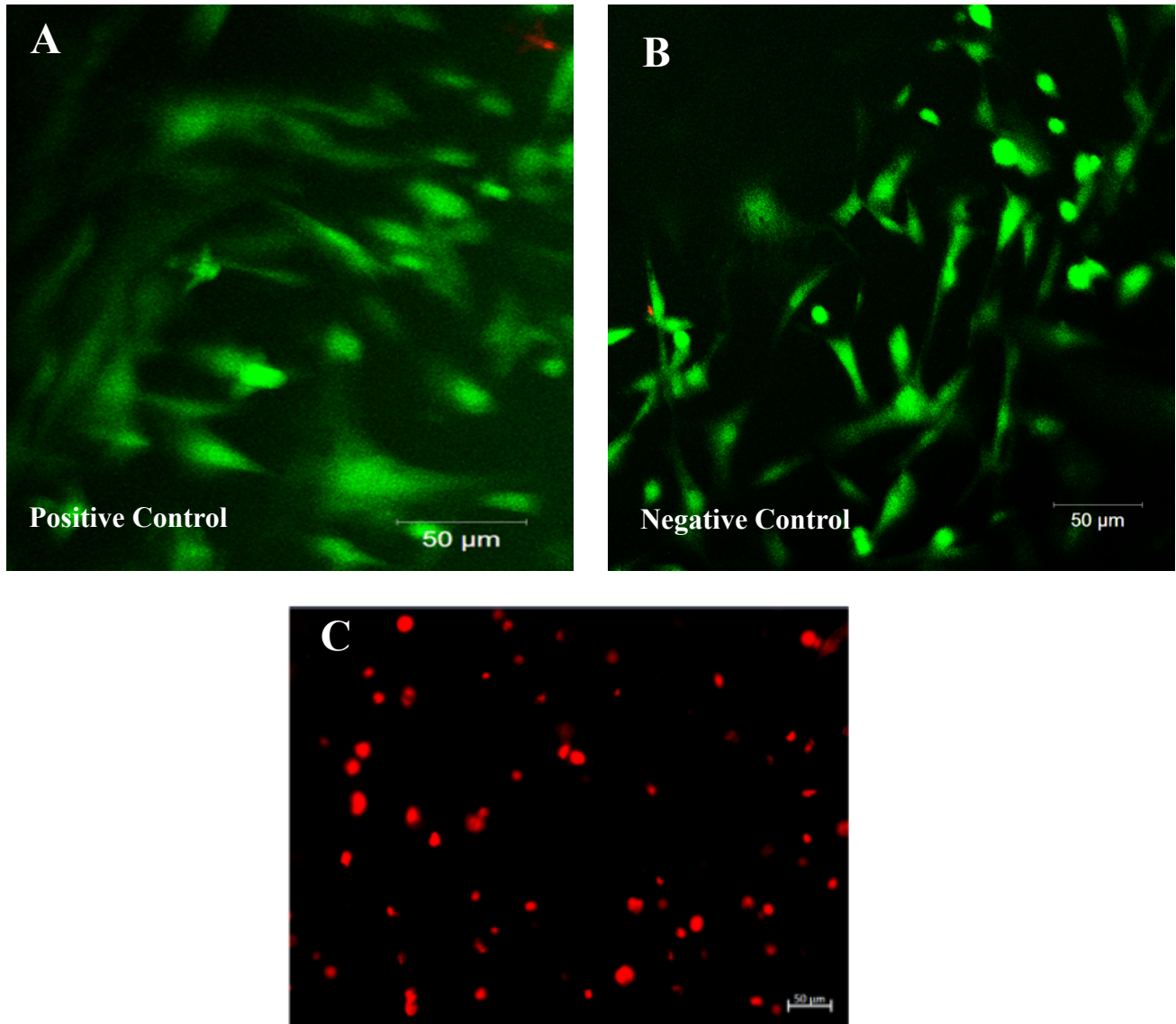
A.1.3: Cell viability was assessed by performing the live/dead assay on 2D structures after 4 days of culture. (A) Shows live cells cultured atop the spheroids (positive control) and stained in green by calcein AM whereas dead cells are stained in red by ethidium homodimer. (B) Depicts cells cultured in plastic wells (negative control). (C) Represents cells printed in a 3D spheroid stained in red by ethidium homodimer after intended apoptosis with ethanol treatment.
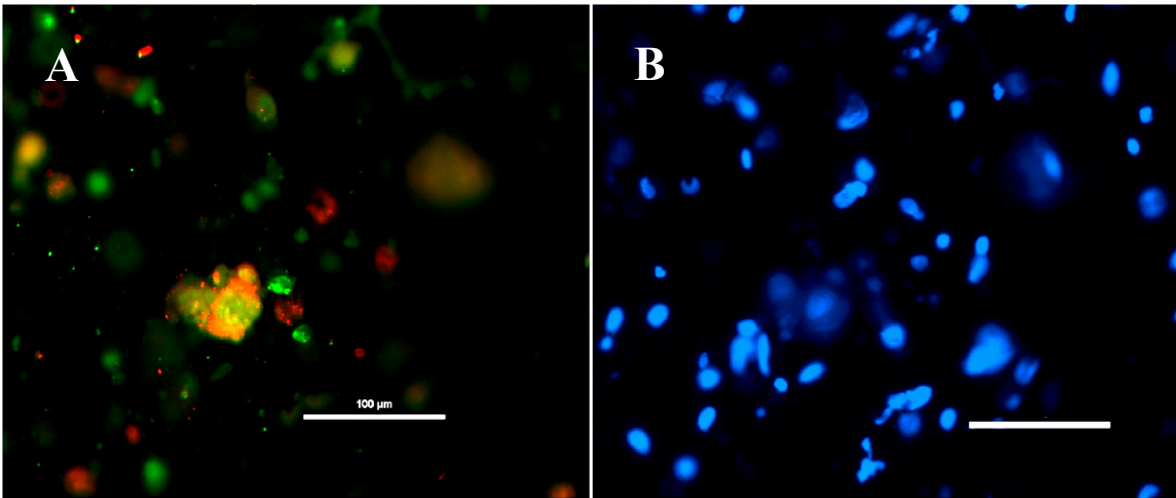
A.1.4: Shown in (A) is an image depicting heterocellular coupling between CM (green) and CF (red) after 21 days of culture and (B) both cell types (CM & CF) with DAPI (blue) staining (Right).
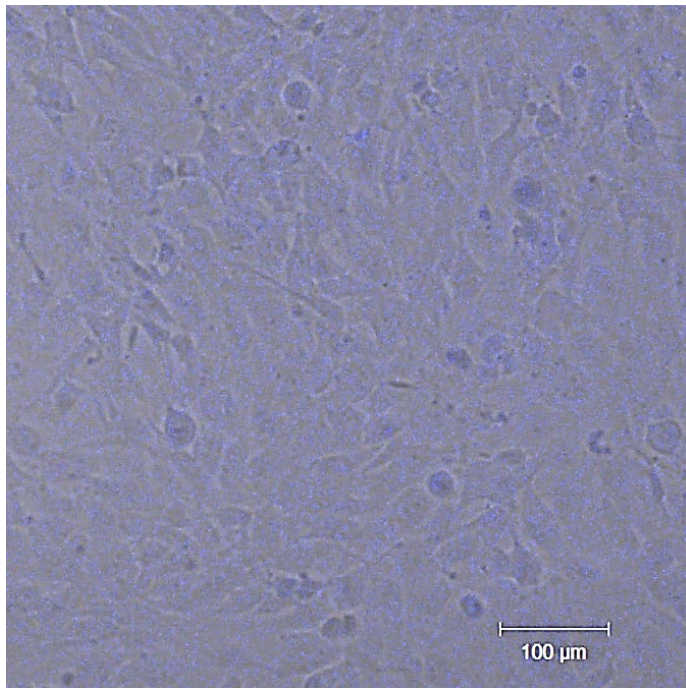
A.1.5: Shown is a bright field image of CTV dye-stained CM cells.

(B)	Day 1	Day 3	Day 5
	Number of LIVE cells	Number of LIVE cells	Number of LIVE cells
0.4µM DOX	27903 ± 620 cells	24677 ± 1234 cells	15645 ± 1203 cells
0.6µM DOX	26290 ± 1546 cells	20483 ± 1223 cells	12741 ± 889 cells
0.8µM DOX	23709 ± 1847 cells	9516 ± 1730 cells	2742 ± 457 cells
1µM DOX	21774 ± 920 cells	5322 ± 798 cells	62 ± 31 cells
Control (NO DOX)	28870 ± 931 cells	28548 ± 1241 cells	27903 ± 1240 cells
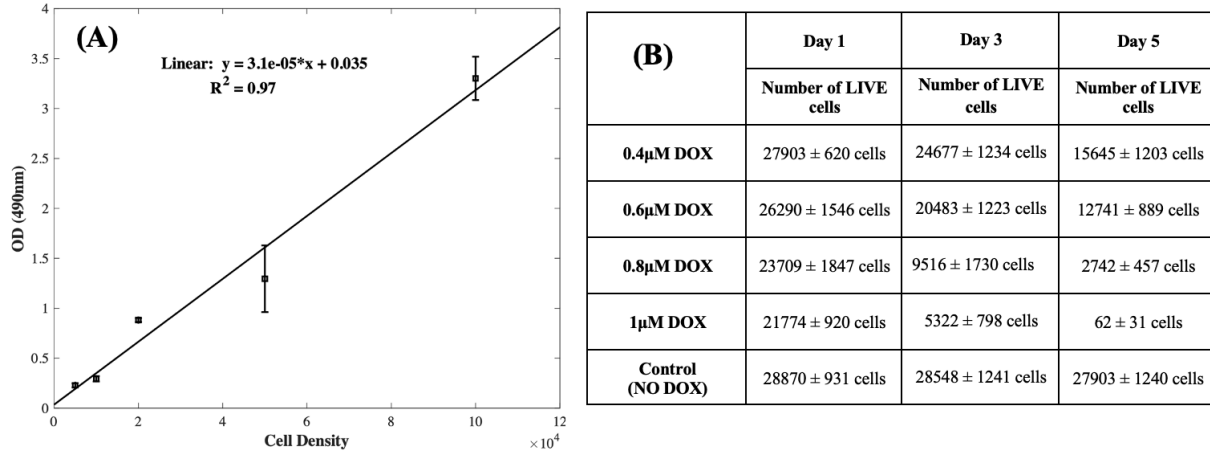
A.2.1: (A) Graph showing the linear best fit curve of the MTS assay data on CMs with various cell population densities in the 3D bioprinted spheroidal droplets. All values are expressed as Mean ± SEM of three replicates (n=3). (B) Table showing the amount of live CMs post-treatment with increasing concentrations of doxorubicin extrapolated from the linear best fit curve of MTS data during 5 days of culture.

(A) Linear: $y = 3.6\text{e-}05*x + 0.074$
$R^2 = 0.97$
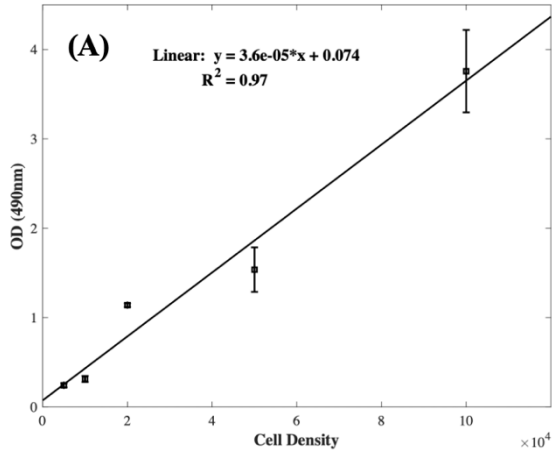
(B)	Day 1	Day 3	Day 5
	Number of LIVE cells	Number of LIVE cells	Number of LIVE cells
0.4µM DOX	26277 ± 1030 cells	21000 ± 1012 cells	17944 ± 997 cells
0.6µM DOX	25722 ± 1286 cells	16556 ± 988 cells	13500 ± 964 cells
0.8µM DOX	22944 ± 1529 cells	6278 ± 1256 cells	4056 ± 369 cells
1µM DOX	20444 ± 1262 cells	1833 ± 523 cells	284 ± 77 cells
Control (NO DOX)	27944 ± 1294 cells	27944 ± 776 cells	27944 ± 1294 cells

A.2.2: (A) Graph showing the linear best fit curve of the MTS assay data on CMs with various cell population densities in 2D samples. All values are expressed as Mean ± SEM of three replicates (n=3). (B) Table showing the amount of live CMs post-treatment with increasing concentrations of doxorubicin extrapolated from the linear best fit curve of MTS data during 5 days of culture.

(A)		Day 1	Day 3	Day 5
		Number of LIVE cells	Number of LIVE cells	Number of LIVE cells
Tiron	1mM	23709 ± 1847 cells	11452 ± 881 cells	6613 ± 827 cells
	8mM	24032 ± 1849 cells	15000 ± 1200 cells	14032 ± 597 cells
	15mM	28225 ± 1551 cells	28226 ± 1241 cells	25645 ± 1545 cells
	Control (NO DOX)	28871 ± 1242 cells	28548 ± 1241 cells	27903 ± 1240 cells
	Control + Tiron (NO DOX)	28548 ± 1552 cells	28226 ± 931 cells	28225 ± 1241 cells

(B)		Day 1	Day 3	Day 5
		Number of LIVE cells	Number of LIVE cells	Number of LIVE cells
NAC	1mM	22741 ± 922 cells	12419 ± 1183 cells	6935 ± 1110 cells
	8mM	23710 ± 1232 cells	15645 ± 1203 cells	15000 ± 900 cells
	15mM	27903 ± 620 cells	26612 ± 1547 cells	26612 ± 619 cells
	Control (NO DOX)	28870 ± 1242 cells	28548 ± 1241 cells	27903 ± 1240 cells
	Control + Tiron (NO DOX)	28548 ± 931 cells	28548 ± 1552 cells	27903 ± 1240 cells

A.2.3: Tables showing the amount of live CMs in the 3D spheroidal droplets post-treatment with increasing concentrations of (A) Tiron and (B) NAC extrapolated from the linear best fit curve of MTS data during 5 days of culture.

(A)		**Day 1**	**Day 3**	**Day 5**
		Number of LIVE cells	**Number of LIVE cells**	**Number of LIVE cells**
Tiron	**1mM**	21278 ± 1013 cells	7944 ± 441 cells	3778 ± 900 cells
	8mM	21833 ± 1269 cells	13222 ± 1202 cells	12667 ± 717 cells
	15mM	26277 ± 773 cells	26833 ± 774 cells	26833 ± 774 cells
	Control (NO DOX)	27944 ± 1294 cells	27944 ± 776 cells	27944 ± 1294 cells
	Control + Tiron (NO DOX)	27944 ± 1035 cells	28222 ± 518 cells	28500 ± 78 cells

(B)		**Day 1**	**Day 3**	**Day 5**
		Number of LIVE cells	**Number of LIVE cells**	**Number of LIVE cells**
NAC	**1mM**	21556 ± 761 cells	9333 ± 911 cells	4611 ± 769 cells
	8mM	22388 ± 2035 cells	13222 ± 1202 cells	12667 ± 956 cells
	15mM	26833 ± 774 cells	26278 ± 1030 cells	26833 ± 774 cells
	Control (NO DOX)	27944 ± 1294 cells	27944 ± 776 cells	27944 ± 1294 cells
	Control + Tiron (NO DOX)	27944 ± 776 cells	27944 ± 1035 cells	28222 ± 1295 cells

A.2.4: Tables showing the amount of live CMs in 2D samples post-treatment with increasing concentrations of (A) Tiron and (B) NAC extrapolated from the linear best fit curve of MTS data during 5 days of culture.
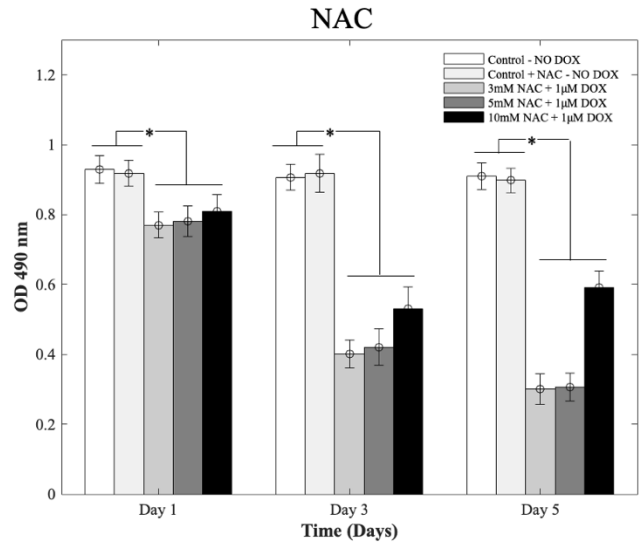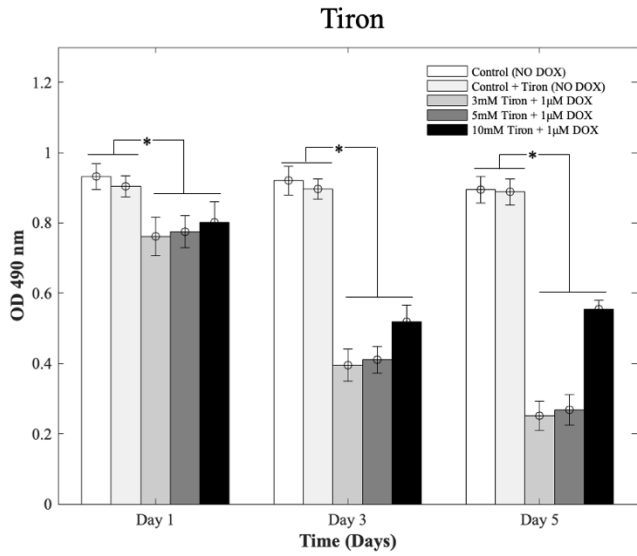
A.2.5: Optical density measurements for MTS assay of CMs in the 3D spheroidal droplets treated with increasing concentrations (3mM, 5mM, and 10mM) of (A) Tiron and (B) NAC respectively with 1μM DOX during 5 days of culture. *p values were found to be all statistically different.

(A)

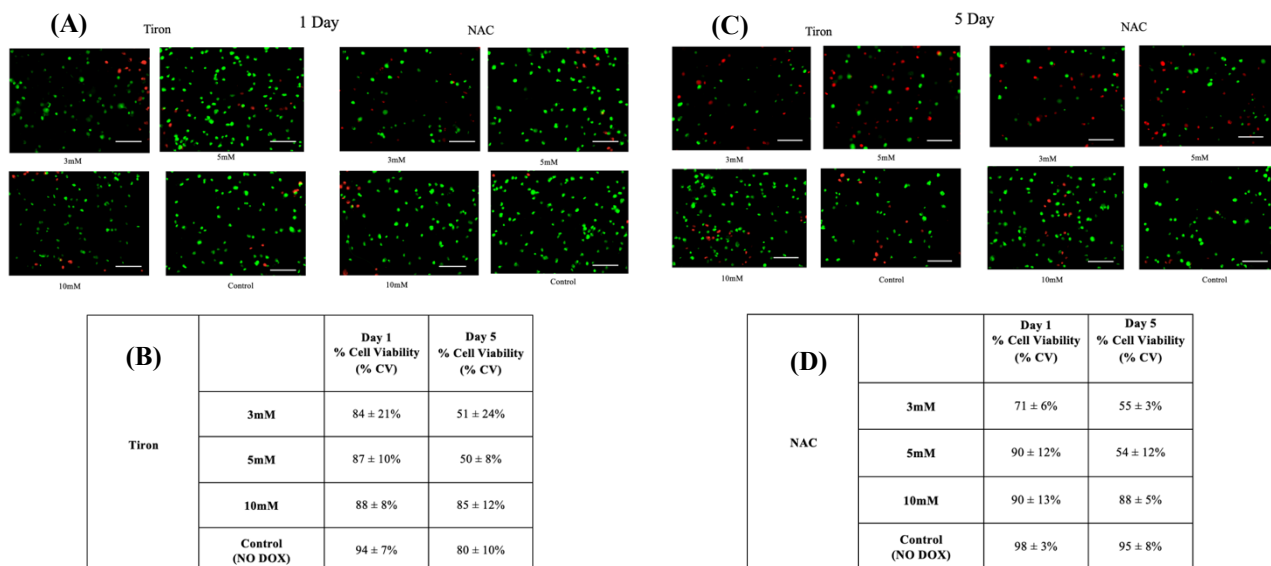| Tiron	Day 1			Day 3			Day 5		
	OD Value	% Cell Viability (% CV)	Number of LIVE cells	OD Value	% Cell Viability (% CV)	Number of LIVE cells	OD Value	% Cell Viability (% CV)	Number of LIVE cells
3mM	0.76 ± 0.06	81 ± 6%	23387 ± 1846 cells	0.40 ± 0.05	41 ± 5%	11774 ± 1472 cells	0.25 ± 0.04	25 ± 4%	6935 ± 1110 cells
5mM	0.78 ± 0.05	83 ± 5%	24032 ± 1541 cells	0.41 ± 0.04	42 ± 4%	12096 ± 1180 cells	0.27 ± 0.04	27 ± 4%	7581 ± 1123 cells
10mM	0.80 ± 0.06	85 ± 6%	24677 ± 1851 cells	0.52 ± 0.05	55 ± 5%	15645 ± 1504 cells	0.56 ± 0.03	61 ± 3%	16935 ± 907 cells
Control (NO DOX)	0.93 ± 0.04	100%	28871 ± 1242 cells	0.92 ± 0.04	100%	28548 ± 1241 cells	0.90 ± 0.04	100%	27903 ± 1240 cells
Control + Tiron (NO DOX)	0.90 ± 0.03	100%	27903 ± 930 cells	0.90 ± 0.03	100%	27903 ± 930 cells	0.89 ± 0.04	100%	27581 ± 1239 cells

(B)

NAC	Day 1			Day 3			Day 5		
	OD Value	% Cell Viability (% CV)	Number of LIVE cells	OD Value	% Cell Viability (% CV)	Number of LIVE cells	OD Value	% Cell Viability (% CV)	Number of LIVE cells
3mM	0.77 ± 0.04	82 ± 4%	23710 ± 1232 cells	0.40 ± 0.04	42 ± 4%	11774 ± 1177 cells	0.30 ± 0.04	30 ± 4%	8548 ± 1140 cells
5mM	0.78 ± 0.04	84 ± 4%	24302 ± 1232 cells	0.42 ± 0.05	44 ± 5%	12419 ± 1478 cells	0.31 ± 0.04	31 ± 4%	8871 ± 1145 cells
10mM	0.81 ± 0.05	87 ± 5%	25000 ± 1543 cells	0.53 ± 0.06	57 ± 6%	15968 ± 1808 cells	0.59 ± 0.05	63 ± 5%	17903 ± 1517 cells
Control (NO DOX)	0.93 ± 0.04	100%	28870 ± 1242 cells	0.91 ± 0.04	100%	28226 ± 1241 cells	0.91 ± 0.04	100%	28226 ± 1241 cells
Control + Tiron (NO DOX)	0.92 ± 0.04	100%	28548 ± 1241 cells	0.92 ± 0.05	100%	28548 ± 1552 cells	0.90 ± 0.04	100%	27903 ± 1240 cells

A.2.6: Tables showing the percent cell viability of CMs in the 3D spheroidal droplets treated with the same concentrations of (A) Tiron and (B) NAC with 1μM DOX extrapolated from the linear best fit curve of MTS data.

(A) Tiron — 1 Day — NAC

3mM, 5mM, 10mM, Control (Tiron)
3mM, 5mM, 10mM, Control (NAC)

(C) Tiron — 5 Day — NAC

3mM, 5mM, 10mM, Control (Tiron)
3mM, 5mM, 10mM, Control (NAC)

(B)		Day 1 % Cell Viability (% CV)	Day 5 % Cell Viability (% CV)
Tiron	3mM	84 ± 21%	51 ± 24%
	5mM	87 ± 10%	50 ± 8%
	10mM	88 ± 8%	85 ± 12%
	Control (NO DOX)	94 ± 7%	80 ± 10%

(D)		Day 1 % Cell Viability (% CV)	Day 5 % Cell Viability (% CV)
NAC	3mM	71 ± 6%	55 ± 3%
	5mM	90 ± 12%	54 ± 12%
	10mM	90 ± 13%	88 ± 5%
	Control (NO DOX)	98 ± 3%	95 ± 8%

A.2.7. Representative fluorescence images of live/dead staining of 3D bioprinted spheroidal scaffolds treated with increasing concentrations (3mM, 5mM, and 10mM) of Tiron and NAC and 1μM DOX. Live cells are stained in green by calcein AM and dead cells stained in red by ethidium homodimer after (A) 1 day and (C) 5 days of culture. (B, D) Tables representing the percent live/dead of cells. The scale bar corresponds to 100μm.
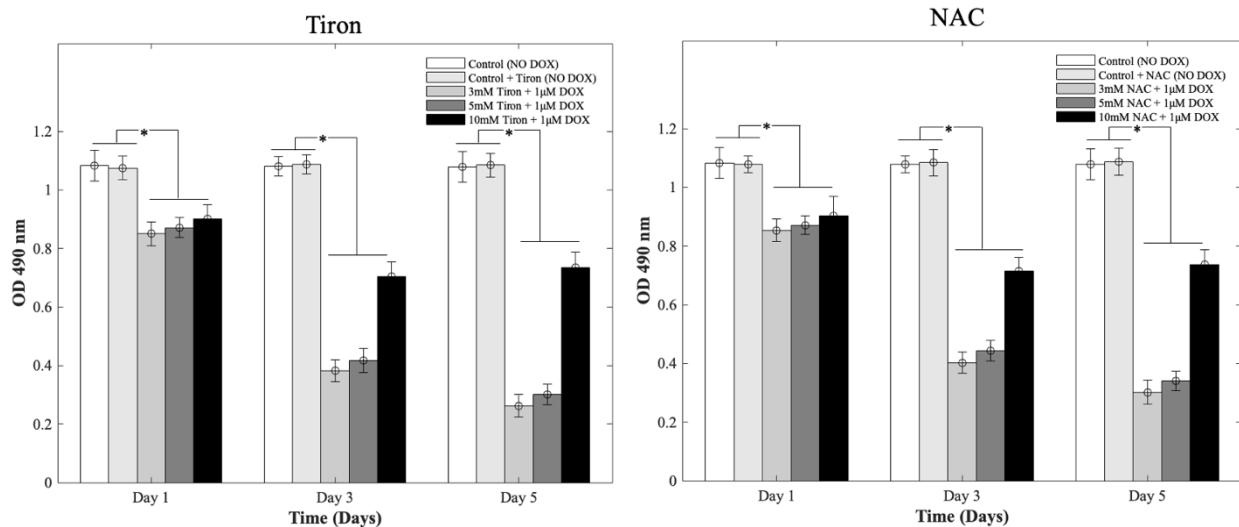
A.2.8: Optical density measurements for MTS assay of CMs grown on 2D samples with increasing concentrations (3mM,5mM, and 10mM) of (A) Tiron and (B) NAC with 1μM DOX after 5 days of culture. *p values were found to be all statistically different. (B, D) Tables showing the percent cell viability of CMs extrapolated from the linear best fit curve of MTS data.

Tiron	**(A)**	Day 1			Day 3			Day 5		
		OD Value	% Cell Viability (% CV)	Number of LIVE cells	OD Value	% Cell Viability (% CV)	Number of LIVE cells	OD Value	% Cell Viability (% CV)	Number of LIVE cells
3mM		0.85 ± 0.04	77 ± 4%	21556 ± 1014 cells	0.38 ± 0.04	30 ± 3%	8500 ± 895 cells	0.26 ± 0.04	18 ± 3%	5167 ± 795 cells
5mM		0.87 ± 0.03	79 ± 3%	22111 ± 762 cells	0.42 ± 0.04	34 ± 3%	9611 ± 915 cells	0.30 ± 0.04	22 ± 3%	6278 ± 837 cells
10mM		0.90 ± 0.05	82 ± 5%	22944 ± 1275 cells	0.71 ± 0.05	63 ± 4%	17667 ± 1244 cells	0.73 ± 0.05	65 ± 4%	18222 ± 1248 cells
Control (NO DOX)		1.08 ± 0.05	100%	27944 ± 1294 cells	1.08 ± 0.03	100%	27944 ± 776 cells	1.08 ± 0.05	100%	27944 ± 1294 cells
Control + Tiron (NO DOX)		1.08 ± 0.04	100%	27944 ± 1035 cells	1.09 ± 0.03	100%	28222 ± 777 cells	1.08 ± 0.04	100%	27944 ± 1035 cells

| NAC	**(B)**	Day 1			Day 3			Day 5		
		OD Value	% Cell Viability (% CV)	Number of LIVE cells	OD Value	% Cell Viability (% CV)	Number of LIVE cells	OD Value	% Cell Viability (% CV)	Number of LIVE cells
3mM		0.85 ± 0.04	77 ± 4%	21556 ± 1014 cells	0.40 ± 0.04	32 ± 3%	9056 ± 906 cells	0.30 ± 0.04	22 ± 3%	6278 ± 837 cells
5mM		0.87 ± 0.03	79 ± 3%	22111 ± 762 cells	0.44 ± 0.04	36 ± 3%	10166 ± 924 cells	0.34 ± 0.03	26 ± 2%	7389 ± 652 cells
10mM		0.90 ± 0.07	82 ± 6%	22944 ± 1785 cells	0.72 ± 0.05	64 ± 4%	17944 ± 1246 cells	0.74 ± 0.05	66 ± 4%	18500 ± 1250 cells
Control (NO DOX)		1.08 ± 0.05	100%	27944 ± 1294 cells	1.08 ± 0.03	100%	27944 ± 776 cells	1.08 ± 0.05	100%	27944 ± 1294 cells
Control + NAC (NO DOX)		1.08 ± 0.03	100%	27944 ± 776 cells	1.08 ± 0.05	100%	27944 ± 1294 cells	1.09 ± 0.05	100%	28222 ± 1295 cells

A.2.9: (A, B) Tables showing the percent % CV and number of live CMs grown on 2D samples extrapolated from the linear best fit curve of MTS data after 5 days of culture.
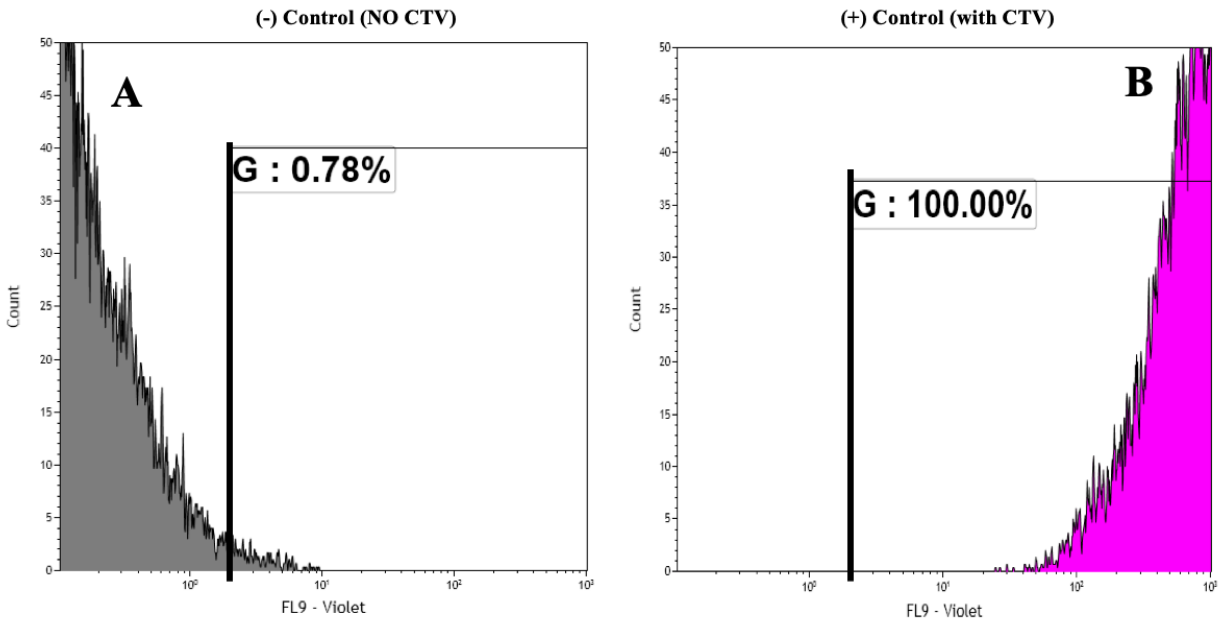
(A) Tiron — 1 Day — NAC

3mM · 5mM · 10mM · Control

(C) Tiron — 5 Day — NAC

3mM · 5mM · 10mM · Control

(B)
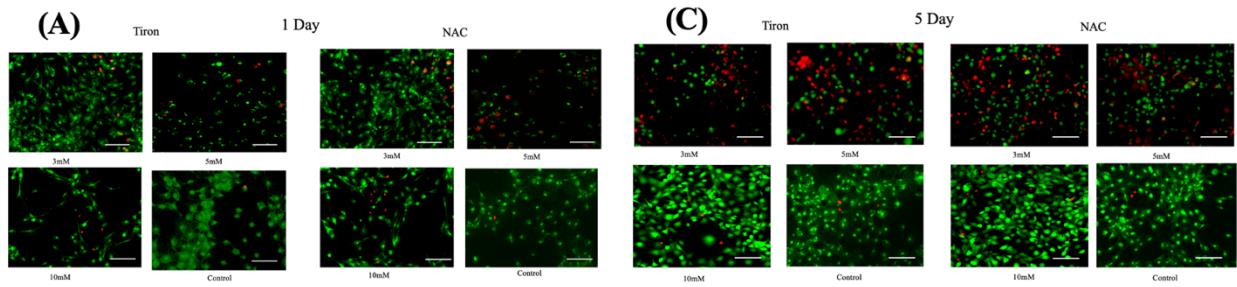
Tiron		Day 1 % Cell Viability (% CV)	Day 5 % Cell Viability (% CV)
	3mM	94 ± 7%	45 ± 11%
	5mM	93 ± 6%	49 ± 9%
	10mM	92 ± 10%	93 ± 8%
	Control (NO DOX)	99 ± 3%	97 ± 3%

(D)

| NAC		Day 1 % Cell Viability (% CV)	Day 5 % Cell Viability (% CV)
	3mM	94 ± 10%	57 ± 7%
	5mM	90 ± 8%	70 ± 14%
	10mM	92 ± 13%	90 ± 10%
	Control (NO DOX)	99 ± 2%	99 ± 2%

A.2.10: Representative fluorescence images of live/dead staining of cardiomyocytes grown in 2D samples treated with increasing concentrations (3mM, 5mM, and 10mM) of Tiron and NAC and 1μM DOX. Live cells are stained in green by calcein AM and dead cells stained in red by ethidium homodimer treated with Tiron and NAC after (A) 1 day and (C) 5 days of culture. (B, D) Tables representing the percent live/dead cells of CMs. The scale bar corresponds to 100μm.
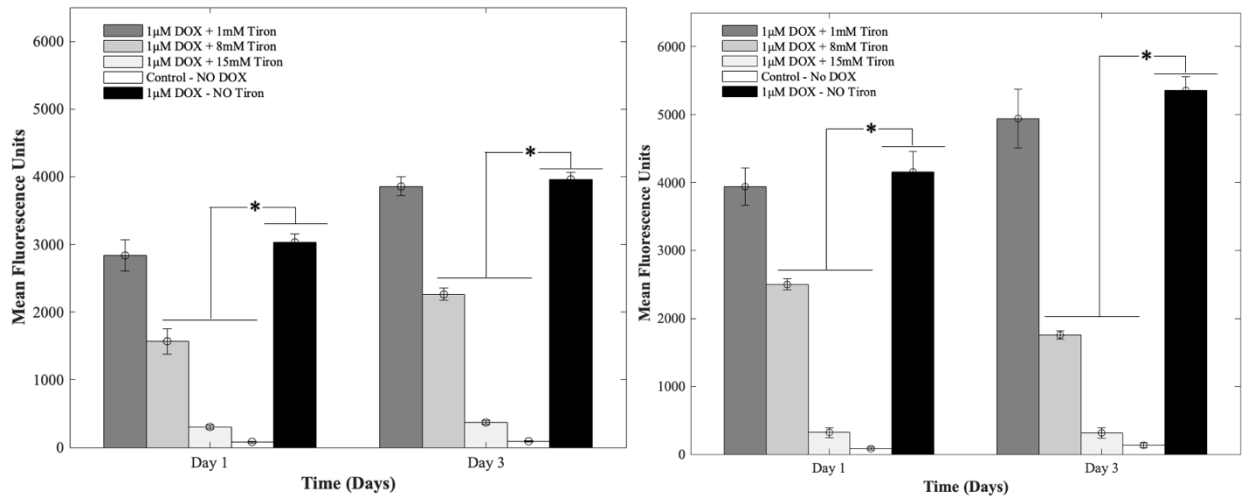
A.2.11: Bar charts illustrating intracellular ROS production using DHE staining of CMs treated with 1,8, and 15 mM of Tiron and 1μM DOX in (A) 3D spheroidal droplets and (B) 2D samples. *p values were found to be all statistically different (p<0.05).

(-) Control (NO CTV)

A

G : 0.78%

Count

FL9 - Violet

(+) Control (with CTV)

B

G : 100.00%

Count

FL9 - Violet

A.2.12: (A) Representative figure demonstrating a characteristic peak of a negative control samples (to the left). On the other hand, shown to the right is a characteristic peak of a positive control sample (B) whereby cells were prestained with CTV dye.

0.4μM DOX

(A)

0.6μM DOX

(C)

Control (NO DOX)

(E)

0.8μM DOX

(B)

1μM DOX

(D)
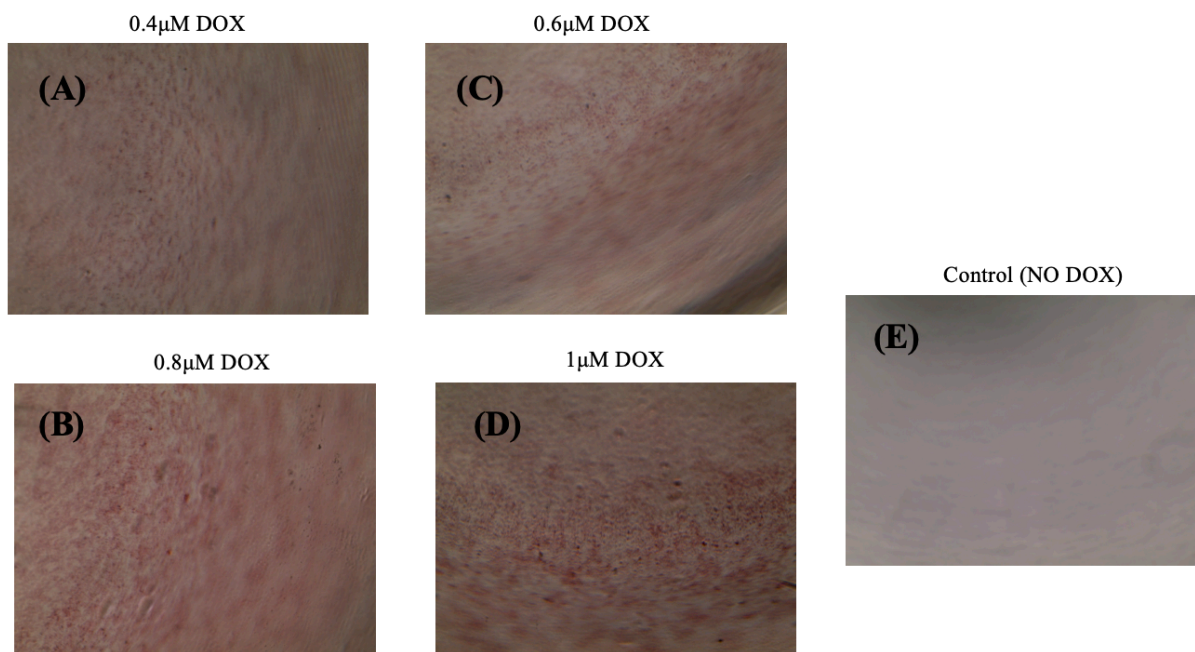
A.2.13: (A-D) Representative figures demonstrating the diffusion of DOX (0.4μM, 0.6μM, 0.8μM and 1μM) into the hydrogel scaffolds in comparison to the control sample scaffold (E) where DOX was not administered.

0.4μM DOX

(A)

0.6μM DOX

(C)

Control NO DOX

(E)

0.8μM DOX

(B)

1μM DOX

(D)
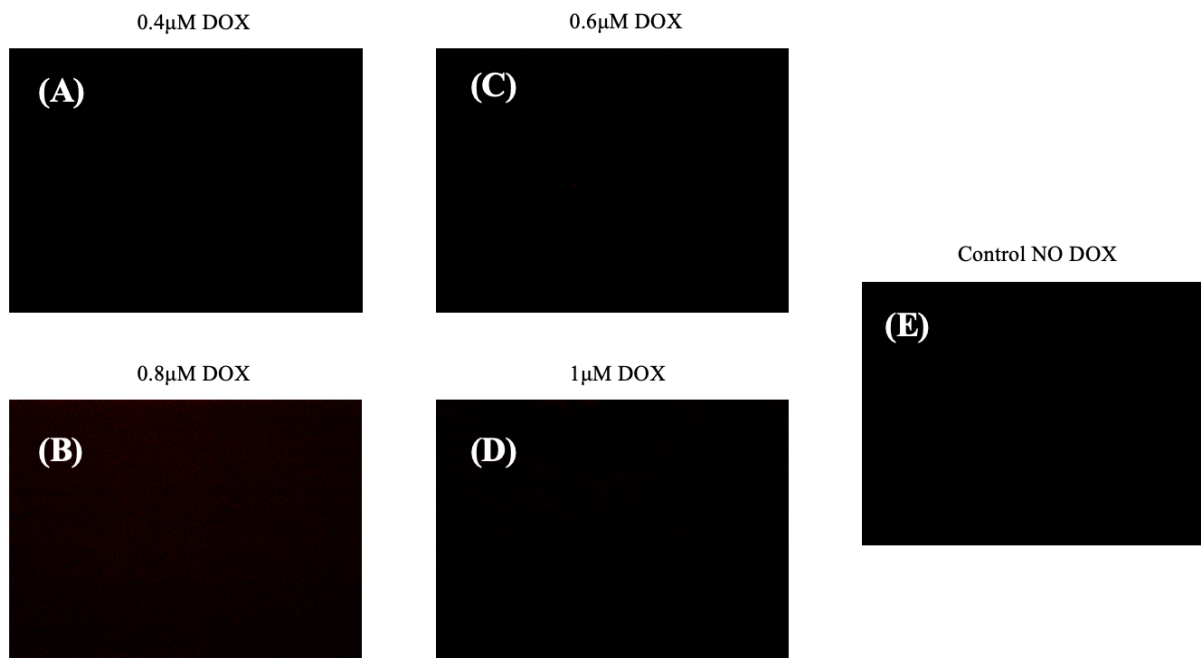
A.2.14: (A-D) Representative figures acquired using the 43 DsRed filter showing no fluorescence with different concentrations of DOX (0.4μM, 0.6μM, 0.8μM and 1μM) in comparison to the control sample scaffold (E) where DOX was not administered.

Vita

Raven El Khoury was born in Byblos-Lebanon, to Dr. Abdo El Khoury and Mrs. Marie-Therese Mouwarrek. He attended his high school education at Antonine Sisters School (Ghazir, Mount Lebanon) where he received his diploma, following which he joined the Lebanese American University of Beirut (LAU) for his bachelor's degree in Biology. After he graduated from LAU, Raven was accepted to the Biomedical Engineering Program at the New Jersey Institute of Technology (NJIT, Newark, NJ), where he worked on several projects, including writing a research proposal that leveraged natural and synthetic polymer biomaterials to create a unique S.M.A.R.T. technology platform of conjugated chitosan-PLGA nanofibers to support various tissue engineering applications with a standard product which demonstrates tunable stiffness properties over time and spatial requirements of three-dimensional scaffolds. Raven then pursued his Ph.D. in Biomedical Engineering at the University of Texas at El Paso. During this time, he served as a research assistant and mentored undergraduate and graduate students. He is also a member of various organizations, such as the Society for Biomaterials (SFB) and the Biomedical Engineering Society (BMES). A record of his awards and publications can be found at:

https://orcid.org/0000-0002-3776-0842